UCLouvain

Université catholique de Louvain
Secteur des Sciences et Technologies
Institut de Recherche en Mathématique et Physique
Centre for Cosmology, Particle Physics and Phenomenology

Development of single gap resistive plate chamber detectors for muography

Doctoral dissertation presented by

R.M. Ishan Darshana Gamage

in fulfilment of the requirements for the degree of Doctor in Sciences

Thesis support committee

Prof. Eduardo Cortina Gil (Supervisor)	UCLouvain, Belgium
Dr. Andrea Giammanco (Supervisor)	UCLouvain, Belgium
Prof. Fabio Maltoni (Chair)	UCLouvain, Belgium
Prof. Vincent Lemaitre	UCLouvain, Belgium
Prof. Michael Tytgat	VUB, Belgium
Prof. Giulio Saracino	University of Naples Federico II, Italy

July, 2023

Remerciements

I would like to take this opportunity to express my sincere gratitude and appreciation to all those who have played an important part in the successful completion of my Ph.D. journey. Their unwavering support, guidance, and expertise have been invaluable throughout this challenging yet rewarding academic journey.

First and foremost, I extend my heartfelt thanks to my esteemed supervisors, Dr. Andrea Giammanco and Prof. Eduardo Cortina Gil, for giving me the opportunity to work with them and for their exceptional mentorship and dedication. Despite their busy schedules, they were always available to me, not only for academic matters but also for personal ones. Their profound knowledge of the subject matter, continuous encouragement, and constructive feedback were instrumental in shaping the direction of my research and refining my scholarly abilities. I consider myself truly fortunate to have had the privilege of working under their guidance. I also extend my gratitude to Prof. W.D.G Dharmaratna and Prof. Giacomo Bruno for being on my supervisory panel. I would also like to express my sincere thank to the members of my Ph.D. jury, Prof. Fabio Maltoni, Prof. Vincent Lemaitre, Prof. Michael Tytgrat, and Prof. Guilio Sarancino, for their expertise and insightful contributions during the evaluation of my dissertation. Their rigorous examination of my work, thoughtful comments, and valuable suggestions have immensely enriched the quality and rigor of my research.

I would like to convey my profound gratitude to all the members of CP3 for their support since day one of my journey. In particular, I want to extend special thanks to our beloved secretary, Carinne Mertens, who has been there for me at every moment I needed assistance, making us feel like we are at home. I am also immensely thankful to Stéphanie Landrain and Carine Baras for their invaluable support in all administrative matters. I am deeply grateful to Laurent Bruniaux, Arnaud Romain, Nicolas Szilasi, Guilhem Vanlancker, and Pavel Damin for their outstanding contributions to the technical and electronic solutions that played a pivotal role in the success of my research. Without their guidance and assistance, completing my Ph.D. would not have been possible.

I would like to extend my most sincere appreciation to the friends whose support and encouragement have played a significant role in my Ph.D. journey. Maxime Lagrange, Marwa Al Moussawi, Sandamali Lokuhitige, Marmar Sabetizade, Matteo Maltoni, Celine Chamieh, Elvis Ferreira your friendship has been a

constant source of inspiration and motivation. Thank you for always believing in me and providing a listening ear during both the highs and lows of this academic pursuit. Samip Basnet and Amrutha Samalan, thank you for being the best colleagues that I could ask for. The good times we had during the last four years are unforgettable.

I would like to extend my sincere appreciation to a group of exceptional friends—Suat Donertas, Khawla Jaffel, Sandya Jain, Julien Touchèque, Jan Jerhot, Vishal Kumar, Ricardo Cabrita, Oguz Güzel, Joshma de Souza, Silvana Romero, Ankit Beniwal and Misha Goodman. Throughout my Ph.D. journey, these friends were not just colleagues but also a source of joy and camaraderie. Our shared lunches, coffee breaks, and small gatherings provided moments of respite during the academic challenges. These casual interactions were not only the highlights of my day but also instrumental in helping me navigate the tougher times. I also extend my appreciation to all the friends from the PhD group who were there for me, including Allexandro Ratto, Jose Baena, Sonia Voinea, Maryam Jafari, David Forsman, Johanna, and all the others. Additionally, my thanks go to the BBT group including Joshma, Silvana, Ankit, and Misha. Your friendship has been a vital source of inspiration, and your presence has made this challenging journey more enjoyable. I am grateful for the laughter, the encouragement, and the shared experiences that have enriched my life during these years.

I sincerely thank to the all friends from my homecountry, Sri Lanka who have been an integral part of my life for the past years. To Malinda Prabath, Malith Ishantha, Chinthaka Kasun, Waruna Weragala, Osanda Kalpitha, Samith Buddhika, Kusal Perera, Krishmila Abeywickrama, Samadhi Hewawasam, Pavani Nadeesha, and Kanishka Samararathna, your friendship has been a constant source of inspiration and laughter throughout my Ph.D. journey. Your ability to both inspire and tease me has made these four years truly memorable. Your unwavering support and encouragement have been the best I could ever hope for. Your presence has made every day brighter and every hurdle easier to overcome.

Last but not least, I would like to thank the most important people in my life, my family. My beloved father, Mr. Nimalsiri Gamage, my mother, Mrs. Piyaseeli Gamage, my granny, Mrs. Rankiri, and my late grandfather, Mr. Manikkuwa. They are the best parents and grandparents. They supported me in every decision I made throughout my life, no matter what. I am grateful to my three sisters, Mrs. Nadeesha Darshani, Mrs. Nimasha Darshani, and Miss. Nilusha Darshani, for being with me throughout the whole journey of my Ph.D. and my life, and for believing in me. I would also like to thank all of my family, including all aunts, uncles, and my cousins.

As an expat, I am deeply appreciative of the unwavering support I received

from my colleagues, friends, and family members throughout this academic journey. Their encouragement, understanding, and belief in my abilities have been a constant source of motivation.

Finally, I would like to acknowledge the institutions and funding bodies that supported my Ph.D. research. Their financial assistance made it possible for me to dedicate myself fully to my studies and pursue my research goals. This Ph.D. journey has been a transformative experience, and I am grateful to everyone who has been a part of it. Their guidance and support have not only contributed to the successful completion of my doctoral studies but have also enriched my personal and intellectual growth Thank you once again for your invaluable contributions to my academic and professional development.

Preface

Muography (or muon radiography) is an imaging technique that relies on the use of cosmogenic muons as a free and safe radiation source. It can be applied in various fields such as archaeology, civil engineering, geology, nuclear reactor monitoring, nuclear waste characterization, underground surveys, etc.

This thesis reports on the development of portable muon detectors (or "muoscopes") which are based on Resistive Plate Chambers (RPC), planar detectors that use ionization in a thin gas gap to detect cosmic muons. Portable muon telescopes can be used for applications where confined space is available to deploy the detectors, e.g. speleology, archaeometry, mineral searches, as well as the imaging of cultural heritage, such as monumental statues and building decorations. For the latter type of applications, imaging methods based on other forms of radiation (X rays, neutrons) have been used with success in some cases, but become infeasible when the objects of interest are too large to be transported to a properly equipped laboratory.

In this context, our goals include portability, robustness, safety and autonomy. Portability imposes strong limitations in both weight and size; robustness means the ability to operate in a wide range of ambient conditions; safety is particularly important in confined environments, and it is not trivial for gaseous detectors; and autonomy means that the detectors should run for extended periods without human intervention, for example by using a battery-based, very low-power readout and control electronics able to adapt to changing environmental conditions.

In the aim of providing full understanding for both experts and non-experts, the chronology of the dissertation is organized as follows:

Chapter one, gives an extended description of cosmic rays, cosmic muons, the production of cosmic muons, and muography. And also explains various applications of muography as well as current detector technologies we use in muography. The second chapter provides a genaral comprehension of RPC detectors. In Chapter three, we discuss the design and production of the first muoscope prototype at UCLouvain. In Chapter four, the design and manufacturing processes of the trigger system of the muoscope are discussed in detail. In addition, the calibration procedure for the trigger is covered in this section. The semi-conductive coating on the resistive plates is one of the RPC's primary components. The manufacturing method for resistive

plates is described in Chapter five, including discussion of the production and calibration of a few detector parameters, as well as long-term investigations of the resistivity measurements. Chapter six, offers understanding of the muoscope's various readout boards; it elucidates the rationale behind each new version of the readout boards.

While the most significant advancements in hardware are covered in chapters four, five and six, Chapter seven discusses the background noise that was present in the RPC lab as well as the steps that were taken to eliminate it. Chapter eight, interprets the performance experiments that were carried out with the RPC and DAQ systems. This chapter, also, covers in details the modifications that were made to the FPGA programming of the DAQ system so that it could function with the trigger system. The last chapter contains a discussion of the results that we have previously obtained from various performance studies, as well as a brief description of our future plans about the scope of the project.

Contents

1. Chapter
Cosmic muons and Muography

1.1. Cosmic rays

Cosmic rays play the most significant part of the muography, by supplying cosmic muons, the radiation source of the muography. This radiation was first observed in 1912 [1], when Victor Hess ascended to 5300 meters, on board of a balloon, and measured the rate of ionization in the atmosphere finding that it increased to about three times that at sea level. Since then cosmic rays were largely measured and studied.

These high-energy particles from space are mostly (89%) protons, i.e. the nuclei of hydrogen, the lightest and most common element in the universe. They also contain (10%) nuclei of helium and (1%), nuclei of heavier elements upto uranium. Typically, these particles are referred to as *primary cosmic rays*. Scientists have also found a small flow of energetic electrons and positrons, equal to about 1% of the flow of hadrons. Part of this flux is probably caused by the pion-muon-electron (or positron) decay chain, which is caused by energetic collisions of the primary hadronic component with the interstellar medium and interactions with the background radiation field.

The energy spectrum of these primary particles has been measured to be between about 1 GeV and over 10^{12} GeV. Figure 1.1 shows the overview of the measurements over 25 years [2]. The main four parts of the global spectrum can be described by an inverse power law, $I(E) \propto E^{-\alpha}$, with a varying value of α. The spectral index is $\alpha \approx 2.7$ from 10 to 10^6 GeV, $\alpha \approx 3$ from 10^6 GeV to 10^9 GeV, and above 10^9 GeV, the spectrum goes back $\alpha \approx$ to 2.6, and then around 10^{12} GeV, after this region, cosmic flux is moving from galactic cosmic to extra galactic cosmic. The knee and the ankle that connect the first and second regions and the second and third regions.The mentioned power laws do a good job of describing the four regions, but there are important signs of a finer structure within them.

When primary cosmic radiation passes through the Earth's atmosphere, it interacts with the atoms and molecules that make up the air. All particles are affected by hadronic and/or electromagnetic processes, which create a large shower of particles with a hadronic core and a photon-electron part that grows mostly in electromagnetic cascades that start when neutral pions decay into two photons.

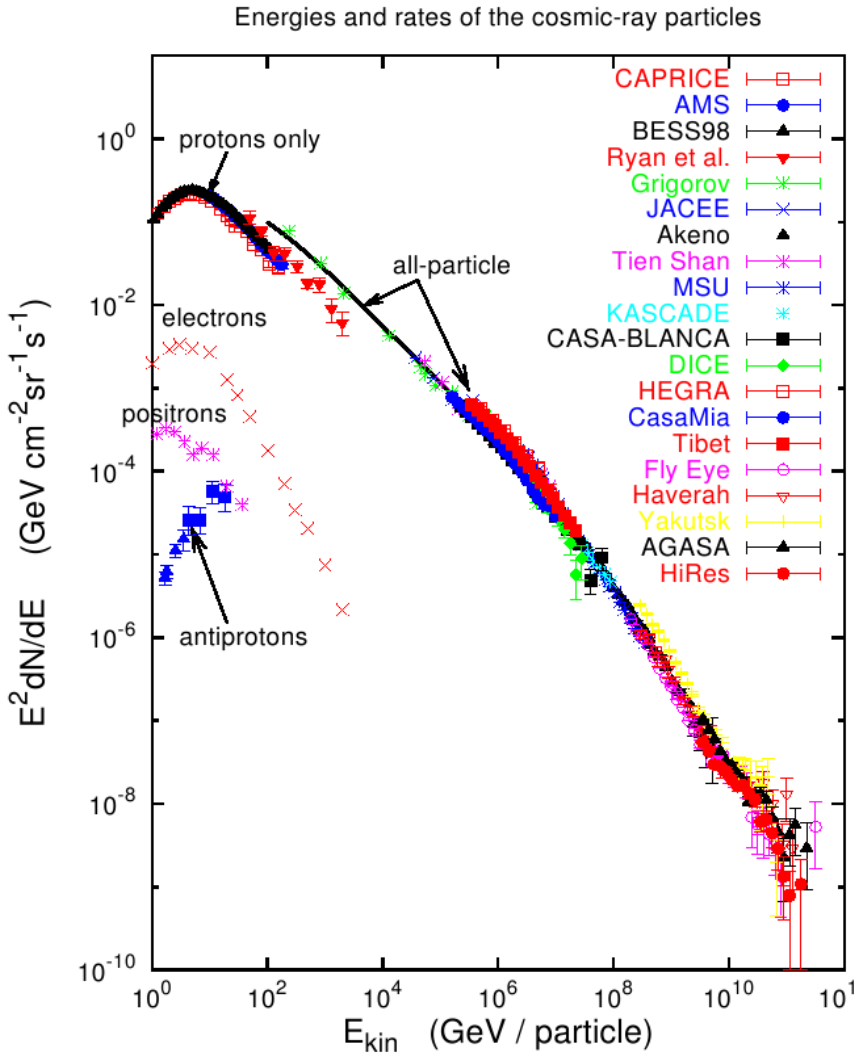

Figure 1.1. | Overview of energy spectra of cosmic rays of all types. Figure from [2]

1.2. Cosmic-ray muons

The muon (μ) is a type of elementary particle that shares most of its quantum numbers with the electron but has a mass that is approximately 200 times greater than that of the electron. It is abundantly and freely produced in the interaction of primary cosmic rays with the upper atmosphere.

The discovery of the muon in 1937 [3] was the result of years of research into cosmic sea-level radiation [4]. The muon was first associated with the particle

proposed by Yukawa [5] to explain the restricted range of the nuclear binding force. However, investigations conducted between 1943 and 1947 revealed that the muon had low or no nuclear interactions with matter [6], contradicting its characterization as a nuclear force mediator. In 1947, Lattes, Muirhead, Occhialini, and Powell established that cosmic muons are produced by the decay of hadrons [7], the most abundant of which is the charged pion with a mass slightly bigger than the muon.

1.2.1. Production of cosmic muons

The muons we use for imaging are called "atmospheric" because they originate in our planet's atmosphere (typically 15 km above sea level), or "cosmic" because of their origin. The primary cosmic rays entering the atmosphere collide with atmospheric nuclei (mostly Nitrogen and Oxygen), producing hadrons that can interact with the atmosphere further unless they decay.In these collisions, pions (π^0,π^+,π^-) and kaons (K^0,K^+,K^-) are formed in large quantities, and when they are charged, their predominant decay modes create muons. See Figure: 1.3.

$$\pi^{\pm} \rightarrow \mu^{\pm} + \nu_{\mu}(\overline{\nu}_{\mu}) \tag{1.1.}$$

$$K^{\pm} \rightarrow \mu^{\pm} + \nu_{\mu}(\overline{\nu}_{\mu}) \tag{1.2.}$$

The branching ratios of these two are 99.99% and 63.5% respectively.

At rest, muons have a lifetime of $\tau \approx 2.2\ \mu$s before they decay into electrons and neutrinos, however a well-known relativistic phenomenon causes this lifetime to be extended by the Lorentz factor (γ):

$$\gamma \equiv 1/\sqrt{1-\beta^2}$$

where $\beta = v/c$ is the relativistic speed.

Most muons reach sea level due to the relative hardness of the atmospheric muon spectrum;the majority of atmospheric muons are created at a height of around 15 km, while the Earth's atmosphere is mostly confined inside 16 km. The great majority of charged particles at sea level are muons, which arrive at a rate of about 100 Hz/m^2 [8]. Protons, electrons, and positrons make up the majority of the other charged particles produced in the cosmic shower that can reach Earth's surface; even though they do not decay, these background particles vanish or lose energy much more quickly than muons due to their stronger interactions with matter: The energy loss through bremsstrahlung depends on $1/m^2$, where m is the mass of the particle, making bremsstrahlung for muons 40,000 times smaller than for electrons and positrons. Moreover, positrons quickly annihilate with the electrons of the atmospheric atoms.

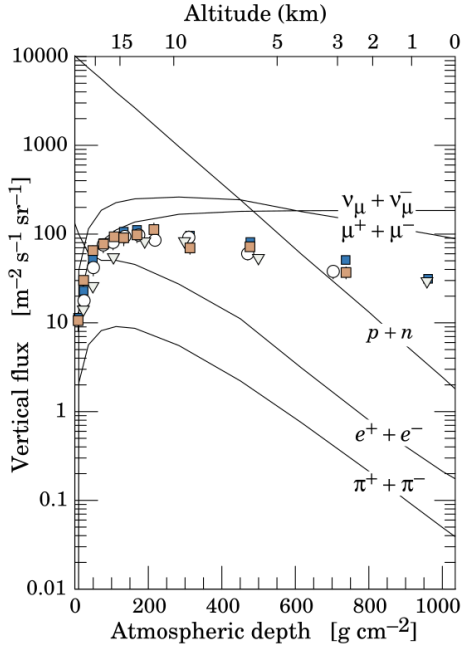

Figure 1.2. | Vertical fluxes of various particles, for momenta larger than 1 GeV. Continuous lines are derived from a model and demonstrate that above this energy threshold, at the sea level (maximum atmospheric depth shown in the figure), the sum of positive and negative muon fluxes constitutes the vast majority of the charged particle flux and is only second to the neutrino flux (that is not a background to muography due to the low interaction rate). Points correspond to measurements of the vertical flux of negative muons only, with different. Symbols corresponding to different experiments [8].

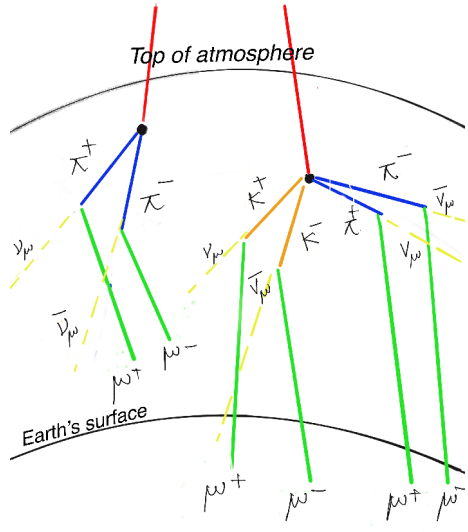

Figure 1.3. | Interactions of primary cosmic ray particles(red line) when they interact with atoms in the upper atmosphere (•).

Nuclear interactions influence protons but are absent for muons. The overall background flux is considerably less than the muon flux due to these factors [8].

For the angular and energy distributions of cosmic muons at sea level or moderate altitudes, several parameterizations exist [9].

Figure 1.4 shows the muon flux (both μ^+ and μ^-) flux in the sea level. The vertical intensity peaks at the kinetic energy of, $k_E \approx 4$ GeV. And the muon charge ratio reflects the excess of π^+ over π^- and K^+ over K^-.

The mean energy of muons arriving at sea level is around 4 GeV, and the mean number of particles traversing a horizontal detector is of the order of 1 cm^{-2} min^{-1} [8]. For detailed calculations, one has to take into account the variations in these quantities, which are due to the altitude and geographical location (especially latitude). On a large time scale, solar effects may also modify the numerical values of the measured flux [10].

1.2.2. Interaction with matter

Muons lose a fraction of their energy when passing through matter, but unlike other particles, they are able to penetrate through hundreds of metres of rock without being totally absorbed. This characteristic makes muons appropriate for examining the interiors of large bodies, such as volcanoes, pyramids, etc. Following the passage of muons through matter, the most significant impacts are:

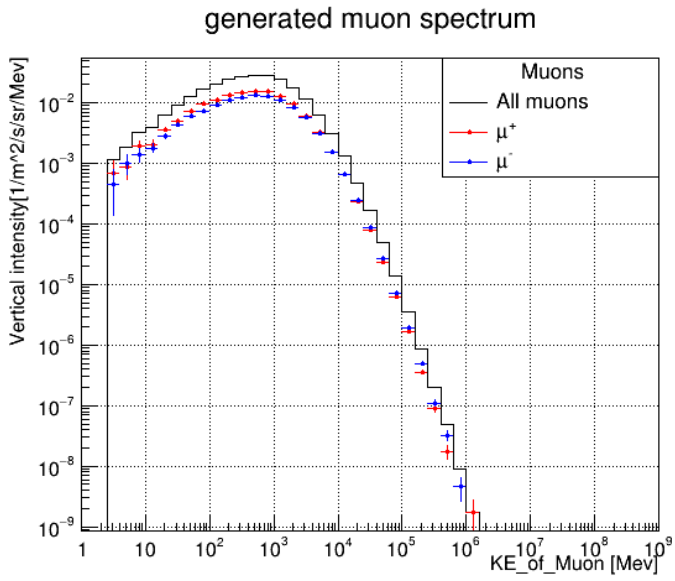

Figure 1.4. | Muon Flux at sea level (Generated with CRY Generator by Marwa Al Moussawi (CP3,UCLouvain)).

- Energy loss
- Trajectory variation (multiple scattering)

Both of these impacts can provide information regarding the composition of the material being traversed.

Energy loss

The mean energy loss per unit length (also called the stopping power) for any charged particle traversing a block of matter is governed by the Bethe-Bloch equation:

$$\left\langle -\frac{dE}{dX} \right\rangle = Kz^2 \frac{Z}{A} \frac{1}{\beta^2} \left[\frac{1}{2} \ln \frac{2m_e c^2 \beta^2 \gamma^2 T_{max}^2}{I^2} - \beta^2 - \frac{\delta(\beta\gamma)}{2} \right] \tag{1.3.}$$

The stopping power of the Equation 1.3 and 1.4 are expressed in $MeV\,g\,cm^{-1}$, K is a proportionality coefficient, and z is the charge number (in multiples of the electron charge) of the incident particle (z = 1 for muons). Z and A are the atomic number and mass of the absorber, and I is the mean excitation energy, where m_e is the mass of the electron, and T_{max} is the maximum kinetic energy transfer in a single collision, and $\delta(\beta\gamma)$ is a correction related to the density effect.

Muons are relativistically significant, heavy, and charged particles. They mostly

lose energy by ionising and exciting the atoms of the medium with which they interact. The following describes the average stopping power of a muon in a given reference [11].

$$-\frac{dE}{dX} = a(E) + b(E)E \tag{1.4.}$$

where $a(E)$ accounts for ionization and atomic excitation, $b(E)$ accounts for radioactive processes, i.e., bremsstrahlung, pair production, and photo-nuclear interactions. The first term, dominating at low energies, below 100 GeV.

Muons lose energy due to inelastic collisions with the electrons of matter, as seen by the first term in Equation 1.4. The radioactive processes that contribute to the muon energy loss are formalized in the term b(E)E, where b(E) is a slowly varying function of energy that is asymptotically constant and can be expanded as the sum of three terms: $b_{brems} + b_{pair} + b_{nucl}$ from bremsstrahlung, pair production, and photo-nuclear interactions respectively. The reflection of these processes on the muon stopping power law is widely discussed and formally derived in [11].

Multiple scattering

When travelling through a medium, muons can experience multiple Coulomb scattering (mcs) [12] from atomic nuclei. The muon's interaction with the nuclei releases almost no energy. For the simple reason that nuclei are so much heavier than muons, even slight scatterings can throw off the muon's path. The msc can be understood as the cumulative result of numerous independent scatterings.

The Rutherford formula accurately describes the single scattering cross section, as seen in the equation 1.5 below.

$$\frac{d\sigma(\theta)}{d\Omega} = \left(\frac{1}{4\pi\epsilon_0}\right)^2 \frac{Z^2 \cdot e^4}{2 \cdot m_\mu^2 \cdot c^4 \cdot \beta^4} \cdot \frac{1}{\sin^4(\theta/2)} \tag{1.5.}$$

Here, Z is the atomic number of the medium's constituent atoms, e is the electron charge, m_μ is the mass of the muon, ϵ_0 is the permittivity of free space and θ is the scattering angle.

Multiple Coulomb scattering, entails repeated random deviations from the muon's trajectory and results in a net exit angle of θ. A schematic of this effect is shown in Figure 1.5.

If the average number of scatterings is larger than 20 and the energy loss is negligible, which is usually the case for muographic applications, the distribution of the net diffusion as a function of the thickness can be derived by statistically treating the process, as in Molière's theory [13]. For numerous

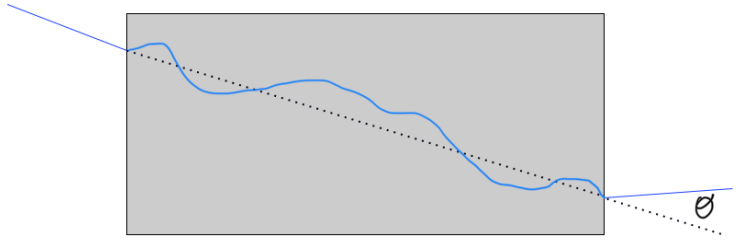

Figure 1.5. A schematic view of multiple coulomb scattering process.

applications, the net scattering distribution can be represented using the central limit theorem, which asserts that the sum of a large number of distributions, in this case the single Coulomb scatterings, can be approximately Gaussian. Following is an expression for the root mean square (rms) of the computed Gaussian distribution of the projected angle, θ:

$$\sigma_\theta = \frac{13.6MeV}{\beta cp} z \sqrt{\frac{x}{X_0}} \left[1 + 0.038 \ln \left(\frac{xz^2}{X_0 \beta^2} \right) \right] \tag{1.6.}$$

where p, βc, and z are the particle momentum, velocity, and charge (for the muons z = 1), x is the path length from entry to exit, $\sigma_\theta = \theta^{rms}_{plaane} = 1/\sqrt{2}\theta^{rms}_{space}$ and X_0 is the material radiation length, defined as;

$$X_0 = 716.4 g/cm^2 \frac{A}{Z(Z+1)\ln\left(287/\sqrt{Z}\right)} \tag{1.7.}$$

where Z represents the atomic number and A represents the atomic mass. Several applications of muon radiography rely on the measurement of muon deflections to evaluate the properties of the deflectant material; more information is provided in the following sections.

1.3. Muography

The absorption and multiple scattering of cosmic muons can be used to image objects. This is called muography. The fundamental idea of muography is to utilise the attenuation or deviation of cosmic muons to visualise large and/or dense objects that conventional methods are unable to handle. Muography by absorption is called **muon radiography** and muography by multiple scattering is known as **muon tomography**. The brief introduction to both methods are described below.

1.3.1. Muon radiography

Muon radiography by absorption is a technique that measures the extent to which muons are absorbed when passing through a specific volume of material. By doing so, it indirectly determines the average density of the materials that

the muons have passed through or identifies any density irregularities such as empty spaces or high-density deposits. These irregularities are visible as an excess or deficit of muons, respectively.

The mechanism is quite similar to that of standard X-ray radiography, which is used to scan the human body or small objects, with the difference that the source in muography is natural (cosmic muons), hence the flow is fixed and multi-directional. Another significant distinction is that muons can penetrate hundreds of metres of rock [14], whereas X-rays cannot survive more than around 10 metres. This feature makes muons more suitable for scanning larger objects than X-rays.

Muon radiography involves measuring the transmission of muons through a target object. This is done by comparing the muon flux upstream and downstream of the object, as a ratio that varies with the zenithal and azimuthal angles (θ and Φ). For large targets, it is not practical to place a detector directly above the object to measure the upstream flux, so a "free sky measurement" is used instead. This involves measuring the flux in angular regions away from the target, either within the same field of view or in a different direction. To reduce systematic errors, these measurements are usually made using the same detector as used for the downstream measurements. However, corrections may be required to account for differences in data taking duration (if free sky measurements are made in a different run) or detection efficiency (if different detectors or angular regions are used). The effective muon transmission (t) is determined by comparing the corrected angular distributions $N_T(\theta,\Phi)$ and $N_{FS}(\theta,\Phi)$ measured downstream from the target and looking at the free sky, respectively [15] [16] [17].

$$t(\theta,\Phi) = \frac{N_T(\theta,\Phi)}{N_{FS}(\theta,\Phi)} \tag{1.8.}$$

A comparison with a simulation is necessary to obtain information on the density distribution inside the target volume. A realistic muon flux characterising the angular and energy spectra at ground level, complete exterior geometry of the volume under inspection as viewed from the detector's point of sight, and an approximated average value of the volume density must all be included in simulations. When the measured transmission is compared to several simulations, each of which is run under different assumptions about the average density, the result is a full 2D average density map distribution as viewed from the detector's perspective.

This kind of analysis relies on the accurate reconstruction of muon tracks. Hence, the spatial resolution of the picked tracking technology has a significant component, as the corresponding angular resolution is one of the parameters that determines the precision of a density map. Most muon radiography

trackers have angular resolutions ranging from a few milliradians to a few tens of milliradians.

1.3.2. Muon tomography

Muon tomography is a distinct muographic technique that takes advantage of the multiple Coulomb scattering mechanism. It is based on the measurement of the deviation of muons through the investigated object. The technique is appropriate for investigating volumes with thicknesses less than tens of metres and involves the installation of detectors to monitor muons before and after they penetrate the object.

Simplifying equation 1.6, the standard deviation of the scattering for a cosmic muon passed through a object of momentum p can be approximated by:

$$\sigma_\theta \approx \frac{13.6MeV}{cp}\sqrt{\frac{x}{X_0}} \tag{1.9.}$$

where x is the path length from entry to exit, and X_0 is the radiation length. Very accurate estimations for $\frac{1}{X_0}$ exist in equation 1.7 [18]. From equations 1.9 and equation1.7, the standard deviation of the deflected angle is directly related to the Z of the object. Therefore scattering muography could be used to identify high Z material with respect to low Z material.

1.4. Applications of muography

The initial practical utilisation of muography can be traced back to the 1950's [19]. E.P George conducted a study to assess the viability of utilising a Geiger counter telescope to deduce the thickness of ice located above a tunnel situated in an Australian mine. The detector did not provide any directional information; however, it was capable of being relocated within the tunnel. The focus of interest pertained to the correlation between the position and the muon flux. During the 1960s, a group of researchers, headed by Alvarez, introduced the initial application of archaeology [20]. Their muon telescope utilised a configuration of spark chambers to effectively reconstruct particle trajectories.

Subsequent to that point in time, significant advancements have been made in the field of muography. The following section provides a concise overview of the various applications.

Volcanology

Since absorption muon tomography utilises cosmic muons that traverse a portion of a solid structure and are partially absorbed relative to those coming from the open sky, it is of great interest in the exploration of hidden parts of mountains, active or potentially active volcanoes. In the years since Nagamine

et al. in [21] and Tanaka et al. [22] used this concept, many different projects, prototype detectors, and operational activities have been done. The Japanese team led by Tanaka [16, 22–25] used a muon telescope composed of multiple detection planes with scintillators and PMTs separated by lead plates; the Diaphane Collaboration conducted measurement campaigns in multiple countries [26–29](France, Italy, and the Philippines) using muon telescopes based on scintillators; and the TOMUVOL Collaboration used resistive plate chambers [30]. Also, a muon telescope built from scintillator strips and SiPM photosensors was used in the MU-RAY Project [31, 32] to investigate Mt. Vesuvius in Italy.

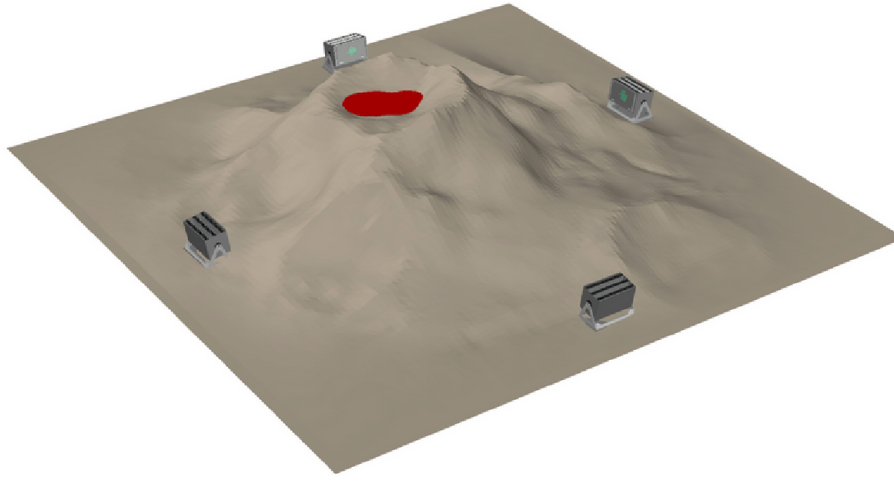

Figure 1.6. Sketch of muographic measurements aimed at a 3D reconstruction of a volcano (image from [15]).

There are two main reasons why this topic is intriguing: first, muon tomography-based techniques have the potential to shed light on previously unknown interior features of mountains, such as cavities or variations in density. Moreover, there is also the hope of improving resolution and gaining the ability to monitor the subsurface structures' temporal evolution in real time, thereby predicting explosions and lava eruptions.

Underground measurements

Although absorption muon tomography excels at examining geological sites, underground cavities, caverns, mines, and tunnels. Several publications [33–35] illustrate this method's effectivity in these scenarios.

The range of rock thickness for many of these uses is typically on the order of tens of metres, which is significantly less than the values of interest in large

volcanic structures. Because it is possible to set up the detector in locations other than those required for volcanic investigations, this method will likely be used more frequently in the near future to probe subterranean environments.

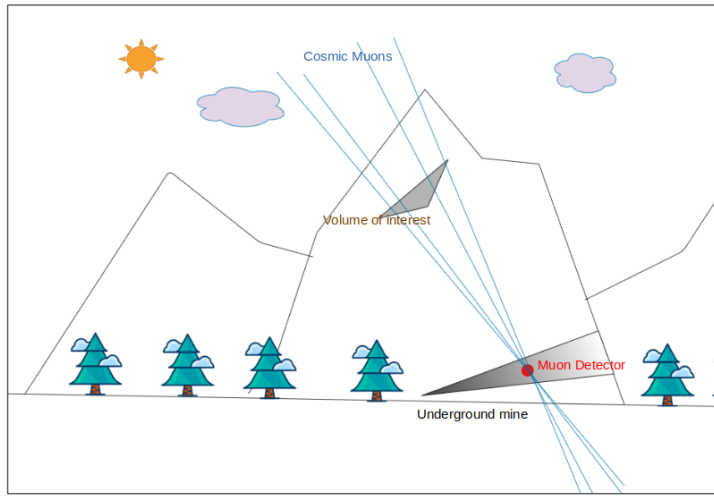

Figure 1.7. | Muon Detector in a underground tunnel.

Archaeology

Alvarez and his colleagues used a muon detector inside an Egyptian pyramid to look for possible hidden chambers [20]. This is one of the first examples of absorption muography. Still, there is a lot of interest in studying these very old structures, and in 2017 [36], the ScanPyramid Project [37], reported that they had found a very large (~30 m), unknown chamber in the Great Pyramid of Khufu. Such a void was first looked into with nuclear emulsions. Then, measurements with scintillation hodoscopes and gas detectors confirmed what the nuclear emulsions had found. This is a good example of how different ways of observing point to the same body of evidence. In the last few years, more examples of how the muon absorption method has been used for archaeological studies [38, 39] . One of these is a study of the density anomalies in the Teotihuacan Pyramid of the Sun [39].

Homeland Security

This method was proposed as an effective replacement for more conventional approaches to inspecting and scanning a large volume, in light of the chance that unauthorized fissile substances (uranium or plutonium) could be shipped inside containers. Two good muon tracking detectors, one above and one below the volume to be examined, are needed for a muon tomograph that

uses the scattering process. The amount of scattering experienced by a muon can be estimated by reconstructing its path above and below the volume, and in the simplest method (where a single scattering centre is assumed), the so-called POCA (Point of Closest Approach) algorithm is used to find the 3D coordinates of the scattering point [40]. It is possible to construct 2D and 3D tomographic images by collecting a big enough number of individual tracks that traverse the volume in any direction 1.8. Based on the tracking detectors, a muontomograph's performance can be measured in terms of its spatial and angular resolution, its overall detection efficiency, which in turn affects the scan time, its ability to identify high-Z elements and discriminate them from lighter elements, and its responsiveness to false-positive events, all of which require a longer scan time.

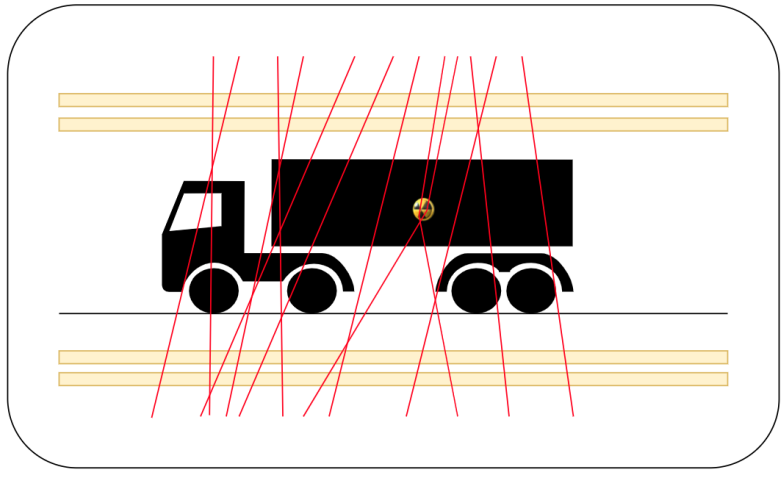

Figure 1.8. | Illustration depicting the experimental rig used for cargo container muon tomography. Reconstructing muon tracks before and after they traverse the container's contents requires the use of two muon tracking detectors, one above and one below the container.

The problem of scanning the contents of a cargo container for concealed high-Z materials is an important one in the context of homeland security, and it was the focus of a number of applications. The sheer number of containers moving around the globe makes it difficult to monitor the contents of all of them. Currently, only a fraction of them are scrutinised. Small-scale prototypes using different detection methods such as gas chambers, segmented strip scintillators, resistive plate chambers, and GEM have been developed using this method over the past few years. Several research groups have reported significant advancements in this area by creating both portable and large - scale detectors for muon tomography [41–46].

Nuclear reactors and nuclear waste imaging

Over the course of several decades, a tremendous quantity of spent fuel has been generated; the vast majority of it is currently being kept in spent fuel pools or dry storage casks. After being filled with used fuel, these canisters are sealed, making it impossible to inspect the contents. So, keeping a close watch on radioactive waste is crucial for ensuring the site's security. Several studies have shown that muon radiography may be used to successfully explore nuclear waste storage silos, whether in muon absorption or muon scattering mode [47–52].

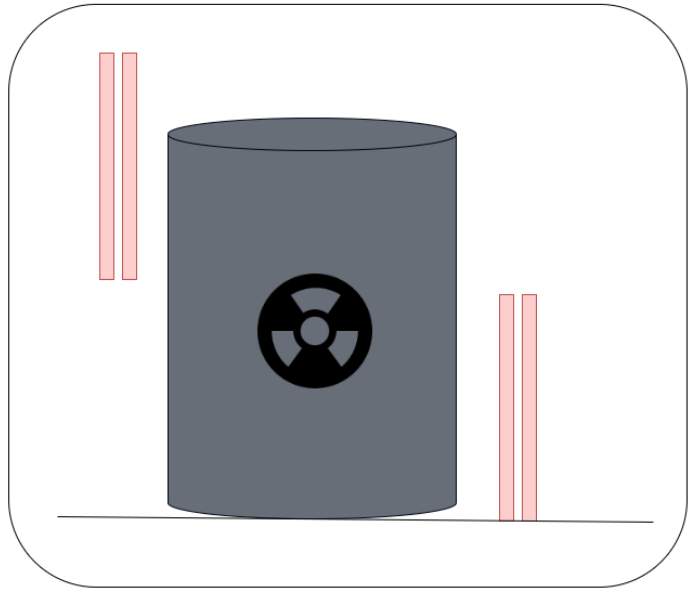

Figure 1.9. | Sketch of Muon scattering tomography is used for the interrogation of nuclear waste casks.

Other applications

Muon tomography can theoretically be used to examine dense structures using either the muon absorption or scattering processes. Muon telescopes were used to image water towers [53], calibrating the detector's response as a function of the water content within the tower. Cosmic muons can be used as a useful probe for the monitoring of civil buildings and structures by the study of the angular distribution of muons detected in coincidence between a tracking detector on the ground and a set of additional detectors mechanically linked to

the structure being monitored. Any movement of the structure relative to the ground will result in a small change in the orientation distribution of cosmic muons detected in coincidence [54].

Some muography teams are attempting to use muography for the purpose of monitoring cultural heritage; In fact, the objects being monitored are fragile, and the researchers are unable to move them or use other monitoring methods such as X-rays because the majority of the artefacts are housed in museums or other crowded locations. Therefore, muography would be an excellent candidate for scanning these kind of objects.

In this section, only a few muography applications are described for the reader's comprehension. More information about applications can be found at the cited source [55].

1.5. Detector technologies in muography

As muography has so many potential uses, detectors must often meet a wide range of conditions that aren't always necessary or even of interest in traditional particle physics. A muography particle detector, in general, needs to be robust and easy to use from a distance. Depending on the setting of deployment, power consumption may be a crucial factor to consider. Due to the low rate of events, the data rate and speed of the data acquisition (DAQ) and front-end electronics (FEE) are not crucial. Generally speaking, various muographic uses call for various detector geometries and detection methods. Hence, many different types of muon detectors have been suggested and constructed during the last few decades, with just a small number of traits in common. One of these is that, despite being highly wanted and potentially a game-changer for muography, it is currently not possible to detect the muon momentum on a per-particle basis.

If the detector system is designed for scattering muography, the muon trajectory must be reconstructed with high precision (typically 1 $mrad$ or higher resolution) before and after the passage through the investigated target. A typical detector geometry is depicted in Figure 1.8, with one of the two tracking systems positioned above (upstream) the target and the other below (downstream). This configuration takes advantage of the greater muon flux from the zenith, thereby reducing the data acquisition time. This is the case, for instance, with muon portals designed for homeland security (Section 1.4), in which data must be acquired as quickly as feasible. Nevertheless, the optimal geometry for particular use cases can vary, as illustrated in Reference [47], where the upstream and downstream tracking systems are positioned on the sides of a large cylindrical cask of expended nuclear fuel (Figure 1.9). In order to maximise muon acceptance, detectors tend to be comparatively large ($1-10m^2$)due to the ensemble's limited geometric factor.

Where absorption muography is applied, such as for imaging of large man-made structures ($\approx$ 10–100 m) or extremely large targets such as volcanoes, a relatively small detector can be positioned laterally to the target, as depicted in Figure 1.6. Installed at a predetermined distance from the target, the typical detector configuration resembles a muon telescope composed of position-sensitive layers. Due to the effect of multiple scattering, the angular resolution is restricted to 10 $mrad$ or greater. For a given X–Y spatial resolution of a single detection plane, a telescope's angular resolution largely depends on the distance between the first and last planes. A greater distance increases the angular resolution but diminishes the telescope's acceptance. When a muography is required of a subterranean target, this telescope geometry can only be utilised if tunnels exist below the target. Given the high cost of drilling or excavating underground, absorption muography detectors that can be inserted into boreholes have been proposed and developed for use in the absence of a suitable tunnel. The first proposal for a borehole detector for muography was published in reference [35], where simulations for a mining application demonstrated promising results in comparison to the telescope option. For a more recent example, see [56].

1.5.1. Scintilator detectors

Plastic scintillators are commonly used for muon tracking due to their quick signal response, large area production, adaptability in severe environments, etc. As atoms in scintillating materials relax after being stimulated by the passage of a charged particle, light is released by fluorescence. The amount of energy released by the impinging muon via ionisation in the scintillating material is determined by the electronic signal produced by the photomultiplier's collection of this light. Crystal, plastic, and liquid scintillators are just a few of the materials used in physics labs and radiation detection applications. Plastic scintillators are widely used in muon imaging (and particularly muography) because they are regarded as being sturdy, dependable, and easy to use. They are best suited for applications where spatial resolution and hence angular resolution is not essential. Systems based on fast responding plastic scintillators can be produced at appropriate cost-to-performance ratios and are suited for application in demanding situations. Moreover, plastic scintillators are simple to form into a variety of geometries (such as square, rectangular, or triangular bars), making it simple to alter the geometry of the detector.

1.5.2. Nuclear emulsion detectors

Nuclear emulsions are analogous to photographic emulsions in that they are used to detect ionising particles passing through a medium by documenting a three-dimensional track. Typically, nuclear emulsions consist of AgBr crystals

interspersed with a polymer (of animal origin). A traversing ionising particle would sensitise the crystals, leaving a latent image. The process of development causes metallic Ag to coalesce on the sensitised site, resulting in the growth of folded filaments on the order of 100 nm to 1μm in length. Granules are aligned along the path of the particle in the medium, making nuclear emulsions a natively 3D particle tracking detector with typically sub-micrometric precision. Nuclear emulsions are sensitive from the time they are produced until they are developed, and the latent image is even more susceptible to chemical reactions than it is to thermal effects and humidity. They can attain angular resolutions of a few mrad, are inexpensive, and do not require an external power source [57]. However, there are significant concerns regarding their use. Initially, the emulsion film begins to document particle tracks upon its inception. As a result, an emulsion sandwich must be created precisely at the start of the observation campaign in order to terminate the information on previously recorded tracks.The OPERA experiment [58] which was designed to identify the extremely rare interactions between neutrinos and matter, had invested significant resources in the development of automated motorised optical systems that scan the plates and use pattern recognition to reconstruct candidate tracks in a reasonable amount of time (typically hours per cm^2). Few laboratories in the world possess these microscopes, making their use more difficult.

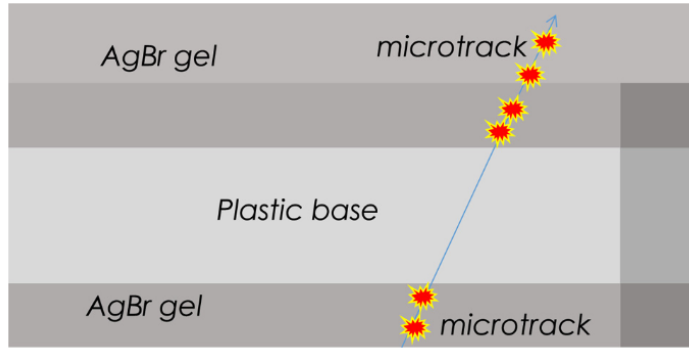

Figure 1.10. | Typical emulsion film structure with double coating on a plastic substrate. Ionising tracks in the sensitive gel produces microtracks. Over the base, two microtracks can be connected to form base-tracks. Picture from [57].

In spite of this, emulsion films have been utilised successfully in a variety of muography experiments and have demonstrated excellent performance in environments ranging from alpine tunnels [59,60] to pyramids in deserts [36] and Mediterranean volcanoes [61], during measurement periods lasting several months.

1.5.3. Gaseous detectors

There are different types of gaseous detectors used in Muography. In this section few of them are briefly explained.

Multi-wire proportional chamber

In 1968, George Charpak developed the Multi-Wire Proportional Chamber (MWPC) [62], which revolutionised the field of particle detectors due to its position sensitivity and ability to measure rates higher than any other device before. The MWPC consists of a gas-filled enclosure with an anode wire plane and two cathode planes that can be realised with wire, strips, or pads. To determine the avalanche position in two dimensions, at least one cathode wire or strip should be perpendicular to the anode wire plane. A typical MWPC is shown in Figure 1.11. When a charged particle passes through the detector volume, it creates primary electrons in its path, and the primary electrons drift towards the anode plane. The field strength is inversely proportional to the distance to the wire, which is why multiplication takes place within a few tens of microns of regions around the wire. A signal is obtained from the wire(s) as well as from the nearby cathode strip(s) due to capacitive coupling. The rate capability of the MWPC is limited by space charge effects, which are addressed by a new generation of detectors known as Micro-Pattern Gaseous Detectors (MPGDs). These detectors are manufactured using microelectronics techniques, ensuring precision gaps and strips up to a few microns. MPGDs are renowned for their spatial resolution, timing response, energy resolution, rate handling capability, and radiation hardness. An example for MWPC in muography can be found here [63].

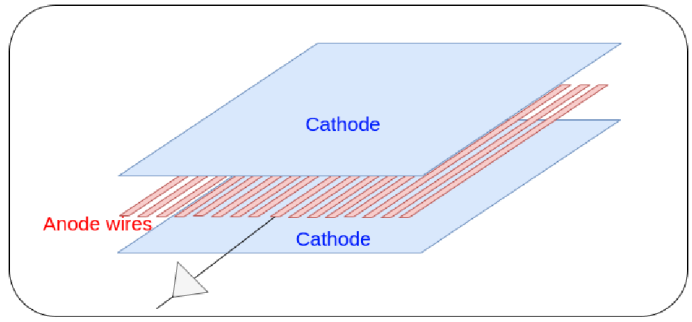

Figure 1.11. | A schematic representation of a MWPC.

Drift chambers

A drift chamber is a particle tracking device that measures the spatial position of an ionising particle based on the drift time of ionisation electrons in a

gas [64]. The primary purpose of these detectors is to measure the time it takes for electrons released by the interaction of an incident muon with an active gas mixture to reach a high-voltage anode wire. This is done by using a sequence of cathode strips driven by high voltage, resulting in a drift field between two PCBs. The anode generates a signal in response to the electrons, which is picked up by the system's electronics and directed by the electromagnetic field. One three-dimensional track point requires two perpendicular detectors, as the interaction location is measured in one dimension by the drift chambers.

As may be seen from the references that follow [65–67], numerous different research groups take advantage of drift chambers for muon scattering tomography.

Micromesh gaseous structure (Micromegas)

The Micromegas [68] are parallel plate detectors with micromesh a few hundred microns above the anode result. The micromesh splits the detector into two parts: the drift gap and the amplification gap. The field strength in the amplification gap is high enough that when the primary waves made in the drift region enter the gap, they cause an avalanche. Due to the small size of the amplification gap, the effects of the space charge are also not very important. The micromesh bends towards the anode plane because there is a strong electric field in the amplification gap. Adding gaps that make more dead areas solves the problem. Also, discharges can damage the anode reading directly and can spread through the electronics.

Resistive plate chambers (RPC)

This thesis work is based on RPC detectors. A detailed description about RPC is included in the chapter 2.

1.5.4. Summary of the Detectors

Summary of various detector as included in the table 1.1.

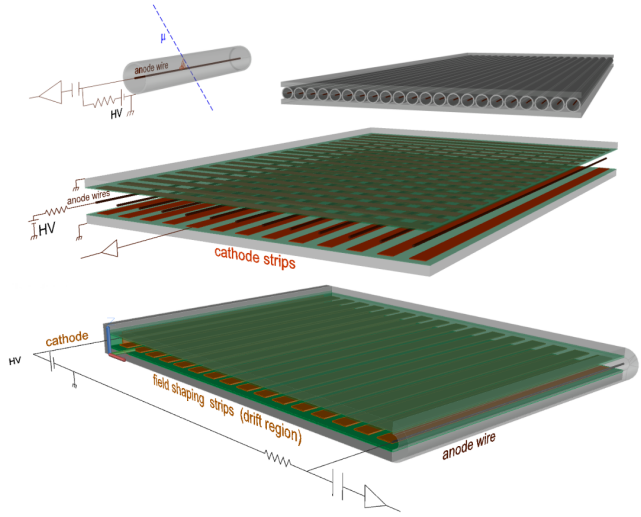

Figure 1.12. | Principle of operation of a gaseous detector. (Top) A position sensitive layer is constructed using cylindrical close-walled tubes. (Middle) Multi-wire chamber approach uses segmented cathode strips for dual coordinate readout. (Bottom) Principle of operation of a drift chamber.The figure is reproduced from [15].

Type	Surface	Resolution	Construction	Readout	Cost
Plastic Scintillators					
square bars	1-4m^2	> 10 mrad	Simple	Simple	Low
Triangular bars	1-2m^2	<10 mrad	Simple	Medium	Medium
Scintillating Fibres	1-2m^2	0.1 mrad	Medium	Complex	High
Gaseous detectors					
Proportional tubes	1-4m^2	10 mrad	Simple	Simple	Low
Multi-wire chambers	>4m^2	< 1 mrad	Medium	Simple	Medium
Drift Chambers	>4m^2	0.1 mrad	complex	Complex	High
Res. Plate Chambers	>10m^2	0.1 mrad	Simple	Medium	Low
Nuclear Emulsion	>4m^2	0.1 mrad	Simple	Complex	Low

Table 1.1. | Summary of comparison of various detectors in muography [15]. Note that in this table, it discusses the standard use case of RPCs, which is for very large areas. In our project, we are developing small-scale RPCs, which entails different challenges.

Chapter 2. RPC detectors

2.1. Brief history

Gaseous detectors are one of first devices used to detect radiation. The first gaseous detectors were built on a cylindrical geometry: the primary electrons formed by the crossing ionising particle were gathered at a central wire, and the avalanche processes happened in the region immediately around it.

Santonico and Cardarelli created the first prototypes of modern RPCs at the beginning of the 1980s using phenolic laminate, commonly known as bakelite, compressed under high pressure. They functioned at atmospheric pressure and did not require as long and complicated a process to manufacture the electrodes [69]. They named this newly created particle detector Resistive Plate Counter (RPC), however we now call them Resistive Plate Chambers.

The following features of Modern RPCs were included in Santonico and Cardarelli design.

- Geometry of planar surfaces (with the consequent advantages of time resolution).
- The electrodes are made of resistive materials, which allows for detector self-quenching and eliminates the necessity for a pulsed operation mode, as well as high-voltage (HV) removal following the passage of an ionizing particle and subsequent discharge.
- HV is applied to the electrodes through a signal-transparent resistive layer.
- The concept of producing detectors that are simple to assemble in order to cover broad areas.

In the original design, two electrodes are kept separate and parallel to one another by inserting a rectangular frame. The surfaces of the bakelite plates facing the gas have been polished and painted with a Linseed oil-based paint. The electric field is applied to the counter by connecting the conducting paper foil to the high voltage and the copper foil to the ground. The output pulses are read out by copper strips applied outside the counter [69]. From this design, they were able to achieve an efficiency of over 90 percent.

Throughout RPC's development history, various working mode [70–72], gas combinations [73,74], and new detector designs have been developed [75,76], resulting in additional detector improvement. RPCs were a natural choice for

muon chambers and/or trigger detectors in multipurpose experiments such as CMS [77] or ATLAS [78], time-of-flight detectors in ALICE [79], calorimeters with CALICE [80], and muography detectors [30] as well due to their low construction costs and easily attainable large detection areas.

2.2. Working Principle

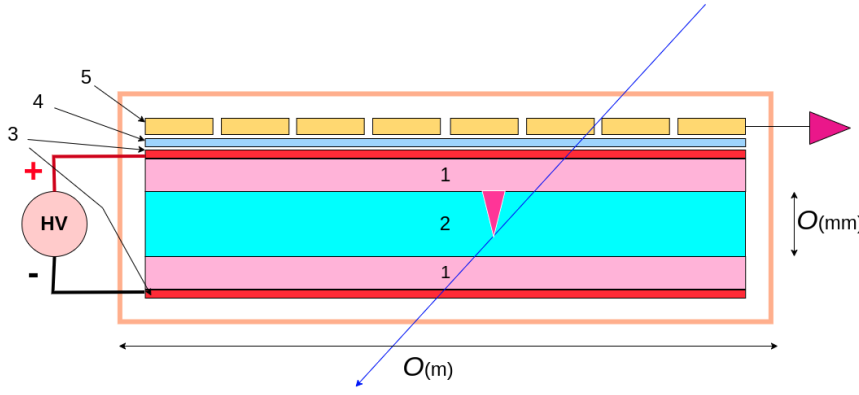

Figure 2.1. | Simple schematics of a single gap RPC. (1) Bakelite/glass electrodes with (Semi-)resistive coating ((3) in the diagram), (2) gas gap, (4) Mylar insulator, (5) readout strips.

Resistive plate chamber detector is a gaseous particle detector that uses a continuous and uniform electric field created by two parallel electrode plates, made with resistive coating (carbon based) applied on a high bulk resistivity material (Typically glass or bakelite). The gap between the electrodes is filled with a gas mixture (More details are in section 2.5) used to produce primary ionisation in the gas volume. The schematics of a RPC detector is shown in a Figure 2.1. The gas molecules are ionised by a charged particle, such as a muon, as they pass through the detector, resulting in the creation of an ionising track in accordance with the Bethe-Bloch formula [81] for the gas being used. This leads to the release of free electrons and ions.

When an unbound electron within a gas is subjected to acceleration due to the electric field, it will undergo diffusion upon encountering gas molecules in its vicinity. This recurrent deflection, occurring across numerous collisions and trajectories, eventually leads the electrons to attain a steady speed known as the drift velocity, v_D. This velocity is a function of electric field strength and gas density (or pressure).

When electric fields reach a certain intensity, the rate of ionization will surpass the rate of attachment. As a result, an unbound electron will initiate a cascade of

additional electrons. This phenomenon is known as *Townsend avalanche*, named after Johh Sealy Townsend, the scientist who first identified this mechanism in the 1890s. The fractional increase in the number of electrons per unit length is given by Townsend equation:

$$\frac{dn}{n} = \alpha \cdot dx \tag{2.1.}$$

Here α is called the first Townsend coefficient for the gas. Its value is zero for electric field values below a threshold value. Likewise, the attachment coefficient, denoted as β, is characterized as the quantity of attachments occurring per unit of distance. For parallel detector structure α and β are constant and so the solution for the equation will be exponential as follows:

$$n(x) = n_0 \cdot e^{(\alpha-\beta)\cdot x} \tag{2.2.}$$

where,

- n_0 : number of primary electrons in the initial position
- α : First Townsend coefficient.
- β : Attachment coefficient.
- x : Distance from the initial position.

Figure 2.2 illustrates the exponential expansion of single-electron avalanches when α surpasses β. As the count of electrons reaches approximately 100, the avalanche experiences rapid exponential growth.

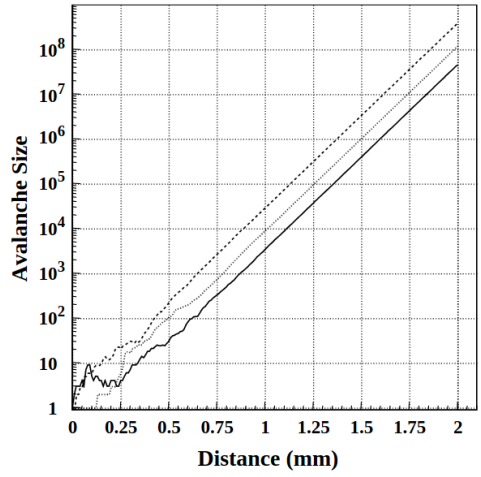

Figure 2.2. Avalanches started by a single electron at x = 0 for α =13 mm^{-1} and β = 3.5 mm^{-1}. The exponential growth $e^{(\alpha-\beta)\cdot x}$ is clearly visible when the number of electrons is sufficiently large. Figure from [82].

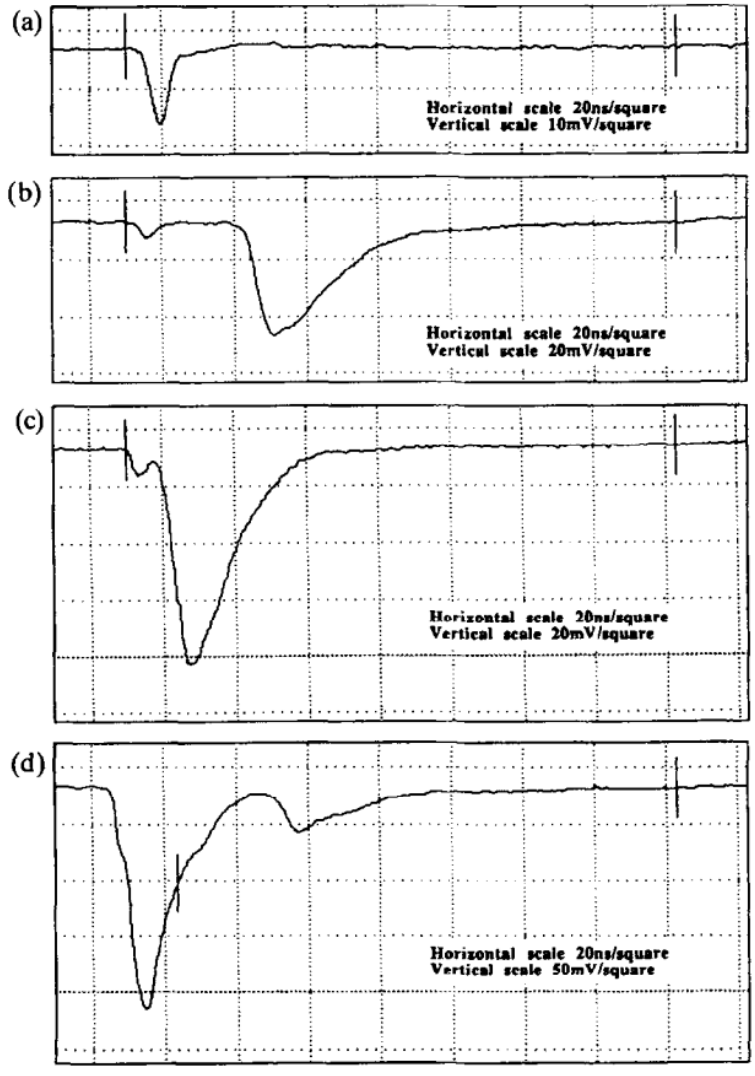

Figure 2.3. | Waveforms of signals at various operating voltages The typical duration of the avalanche signal (a, 9.4 kV) is 4-5 ns FWHM. A streamer signal appears 38 ns (b, 9.6 kV) after the avalanche. The avalanche-streamer delay gradually decreases at increasing voltages (c, 10.2 kV), and eventually (d, 11.4 kV), the avalanche-streamer signals combine into a single pulse. Additionally, multi-streamer signals are seen [70].

Let Q be the total charge produced by avalanche process:

$$Q = n_0 \cdot e \cdot M \tag{2.3.}$$

Where:

- n_0 : number of primary electrons.
- M : multiplication factor.
- e : charge of the electron.

An essential component of particle detection with an RPC is the avalanche process although RPCs can only operate in the avalanche mode ($M < 10^6$) when the electric field is strong enough. If not, it won't be able to detect anything because the signal is too weak (drift-only regime).

Streamer mode (also known as spark mode) is another method to use an RPC. If the electric field is increased past avalanche mode, this regime can be attained [70]. Sparks appear when the total charge in the avalanche is close to or exceeds 10^8 electrons ($M > 10^8$)(the so-called Raether limit [83]). Although the electrode generates a larger (almost 100 times greater) charge, the recharging process takes more time. As a result, this regime has greater dead time, which results in a rate constraint.

2.3. Signal formation

The process of signal generation in RPCs is straightforward and is applied in many gas-filled ion chambers, proportional counters, and even semiconductor detectors. The signals produced by these detectors result from the movement of electrically charged particles (electrons) once they are created by the incoming radiation.

The signal induced by the movement of charged particles on a conductor was described by the *Shockley-Ramo theorem*. This theorem originated from the works of William Shockley in 1938 [84], where he presented a method for calculating the current induced in a conductor by a nearby moving charge. Simon Ramo further contributed to this theorem a year later by providing a more comprehensive and mathematically detailed explanation [85].

This theorem is founded on the principle that instantaneous electric currents in a conductor, induced by external moving charges, result from the change in electrostatic flux lines across that electrode. Using Green's Theorem, Shockley and Ramo derive the following formula:

$$i(t) = \frac{\vec{E_w}(\vec{x}(t)) \cdot \vec{v}(\vec{x}(t), t)}{V_w} \cdot q \tag{2.4.}$$

Where, $v(t)$ is the instantaneous velocity vector of a point charge q, and $\vec{E_w}$ is a *weighting field* with the weighting potential V_w. The weighting field is calculated for each electrode by setting it to the potential V_w (Usually 1 V) while all other conductors are grounded (Figure 2.4). The weighting vector field explains how much of the charge particle's motion contributes to the formation of an electric current in the electrode. It effectively quantifies the electrode's sensitivity to

particle motion, offering insight into the overall current generated based on the movement characteristics of the charge. Note that quantity $\vec{E_w}/V_w$ has dimensions m^{-1} although equation 2.4 is often cited in a way that drops V_w, suggesting the wrong $V\ m^{-1}$ dimensions.

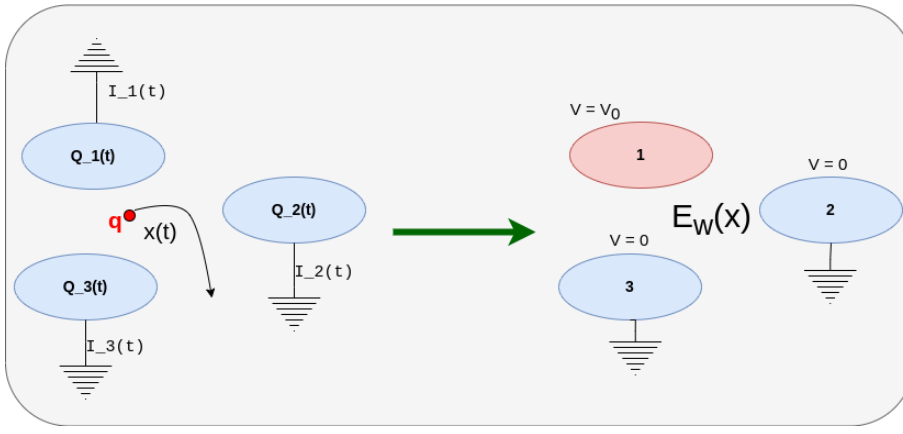

Figure 2.4. | Visualization illustrating Ramo's theorem and the concept of weighting field. It computes the current induced on a grounded electrode by a charge q travelling along a trajectory.

In a simple case where $\vec{E_w}(\vec{x}) = E_{w,z} = E_w$, uniform with x and y components are equal to zero, and drift velocity of the charge particles are assumed as v_D in the medium, the current induced $i(t)$ can be written as:

$$i(t) = \frac{E_w \cdot \vec{v_D}}{V_w} \cdot e \cdot N(t) \tag{2.5.}$$

where, e is the charge of the electron and $N(t)$ is the electrons at time t.

The Shockely-Ramo theorom mentioned above is only valid if the electrodes are ideal conductors surrounded by insulators that produce instantaneous currents. Since RPC detectors have resistive elements, W. Riegler extended the Ramo theorem to deal with this. More thorough discussion on signal genaration was discussed in the refernce [86] including the effects from detector geometry.

2.4. Electrodes of the RPC

The electrodes of the RPC have two components. The high-resistivity material and the semi-resistive (in some references, it is mentioned as semi-conductive) coat applied to one side of the electrode material. This section gives an overview of the importance of selecting the electrode material and the semi-resistive coating.

2.4.1. Electrode material

There are several factors involved while selecting the electrode material. The spatial resolution is diminished if the bulk resistivity is too low, as the signal will extend across the plate. If the resistivity is quite high, it will take longer for the electrodes to recharge, which is inconvenient for high-rate events. The resistivity of a material used in RPC should remain stable; otherwise, the rate capability would be compromised. This issue is caused by the ageing of a detector, and it affects a large number of RPCs made from bakelite. It is important to maintain the smoothness of the surface of the electrode since it improves the noise characteristics of the detector [87]. Usually, bakelite is coated with linseed oil to obtain a smooth surface. The resistivity of the materials used at making RPCs are ranging from 10^9 to $10^{!2}$ Ω.cm. Table 1 shows the most common RPC electrode materials, Where ϵ_r is the relative relative permeability of the material.

Material	Bulk resistivity(Ω.cm)	ϵ_r
Glass	10^{12} - 10^{14}	~ 7
Bakelite	10^{10} - 10^{11}	~4.7
Doped ceramics (SiN/SiC)	10^9	~8.5

Table 2.1. Properties of the most used electrode materials for RPCs.

Each of these materials has it's own pros and cons. But due to the low cost and no ageing effect and low rate capabilities doesn't affect when dealing with cosmic muons, we use floating glass for develop RPCs for muography applications.

2.4.2. Resistive coating

Resistive layers serve a crucial role as indispensable components of RPC detectors. These layers receive the working voltage and have to distribute it uniformly across the electrode surface in order to ensure a homogeneous electric field across the gas gap, and the charge of an avalanche also dissipates through them. The surface resistivity of these layers is a crucial parameter that must be precisely adjusted. it should be low enough to ensure uniform HV distribution and sufficiently high to be "transparent" for the avalanche-induced signal. If the surface resistivity is less than a few hundred $k\Omega/\square$, the induced signals will propagate through the resistive layers over a large area, resulting in a large cluster size [88] and if the surface resistivity is excessively high, however, a large electric potential difference will form along the detector's surface. This will decrease the effective working voltage in regions far from the injection site of working voltage, particularly for RPCs with very large sizes

and in high irradiation conditions. In this instance, the surface resistivity must be regulated between several hundred $k\Omega/\square$ and several $M\Omega/\square$ [89].Resistive layer is usually made with graphite, carbon based inks [90] or conductive sheets.

2.5. Gas Mixture

As with RPCs, the gas is, in a sense, the "heart" of a gaseous detector. Particularly, RPCs necessitate the use of gas compositions with few characteristics for efficient operation [91] :

- High primary ion-electron cluster density to ensure high detection efficiency.
- It should have relevant quenching features in order to reduce the ionization from UV protons and to avoid the sparks.
- Being electronegative, to reduce the transversal side of the discharges and improve its localization.
- Possibly, it should not be hazardous to human health or the planet.

The first RPC [69] was operated in streamer mode with a mixture of Argon and butane (50%/50%), a standard mixture use in multi-wire proportional chambers. This mixture maximized the number of primary charge carriers freed in the gas by ionising particles and used the Townsend coefficient of Argon to determine the multiplication and attachment of primary ionisation electrons. Prior to the discovery of the avalanche mode, the rate capability of RPCs in streamer mode was a concern due it long propagation time (See Figure 2.3). To improve performance, the fast charge ratio in signal development could be increased, reducing the charge induced per avalanche. Studies using Freon-based quenchers, such as CF_3Br, showed that a lower induced charge could improve rate capability [70]. This led to the discovery of the avalanche mode, which confirmed that smaller induced charges improved RPCs' rate capability.

The typical gas mixture used in RPCs operated in avalanche mode is consist of following three gases:

1. **Tetrafluoroethane ($C_2F_4H_2$)**, also known as Freon or R134a, is the predominant component of RPC gas mixtures, accounting for a typical proportion of over 90%. It is used due to its high effective Townsend coefficient and large average fast charge, which permit the detector to operate with a higher threshold than, for instance, Argon, which has a comparable effective Townsend coefficient but a lower fast charge. To operate under comparable conditions, Argon would require a stronger electric field, resulting in a greater proportion of streamers and thereby limiting the detector's rate capability.

2. **Isobutane (i-C_4H_{10})**, which is only present in a small percentage of gas mixtures, is utilised for its UV-suppressing properties, thereby preventing avalanche streamers caused by UV photon emission.

3. **Sulphur hexafluoride (SF_6)** is utilised in extremely small amounts due to its strong electro-negativity. The compound absorbs excess electrons, preventing the formation of streamers. However, a percentage of SF_6 greater than 1% will not provide any additional benefits in terms of streamer cancellation power, but will increase the operating voltage [74].

In our muoscope prototype, we are currently using a gas mixture of $C_2F_4H_2$ (95.4%), i-C_4H_{10} (4.5%) and SF_6 (0.3%).

Moreover, $C_2F_4H_2$ and SF_6 are greenhouse gases. Finding a gas mixture that is less harmful to the environment is the subject of current research [92–94].

2.6. Performances of RPC

2.6.1. Detection efficiency

A RPC's detector efficiency is primarily determined by gas multiplication. Variations in the gap's width can affect the gas's multiplication. The charge distribution differs between narrow and broad gaps. For narrow gaps, the number of events with minor induced charges is always greater than for wide gaps, where the number remains constant and decreases $q_{ind} \rightarrow 0$ [95], where q_{ind} is the charge induced on the pick up electrode. Figure 2.5 demonstrates this conduct. Small induced charges necessitate high-quality amplifiers, low thresholds, and low noise. Therefore, wider distances are more effective, although higher HVs are needed.

For a signal to be detectable, the gas gain or multiplication must be set high enough to generate a sufficient avalanche. Electrons initiating an avalanche across the entire gap width will generate the strongest signals. Avalanches that began further away from the cathode may not grow large enough to generate a detectable signal. There is a minuscule chance that the first millimetre closest to the cathode has no primary ionisation. In this case, the probability of generating a detectable signal depends on the remaining distance from which a cluster may form and grow. With a large separation, there is more space for an avalanche to reach the detection threshold. Wider gaps tend to have a lower probability of streamers for the same detection efficiency as narrow gaps [95] because the gain can be set to a lower value in a wider gap. However, wide gaps have a lower time resolution because the electrons must travel further. Variations in gap width are significantly worse in narrow gaps than in wide

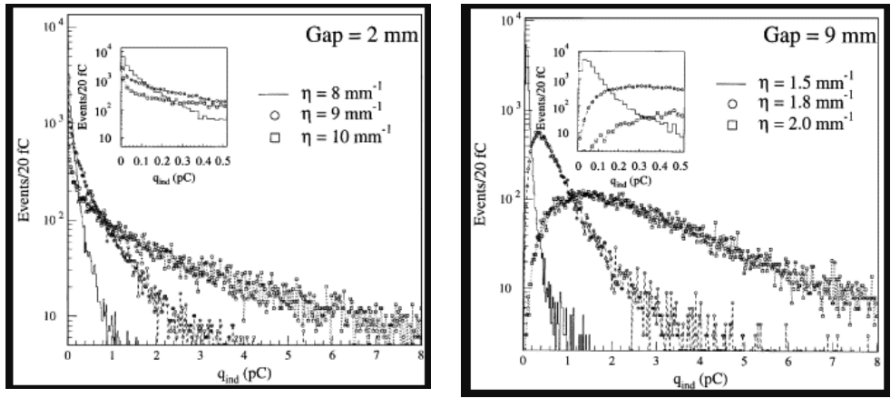

Figure 2.5. | Charge spectra for a narrow and wide gap [95].

gaps. Variations in the gap width by 100 micrometres can already result in a variation in gain by a factor of 2500 for a 2 mm narrow gap [96].

2.6.2. Timing resolution

RPC detectors are well known for their excellent timing resolutions. A simplified way to compute the timing resolution is given in [82]. Let's consider a signal - in terms of induced current - of a primary electron inside the gas gap:

$$i_{ind}(t) = I_s \cdot e^{(\alpha-\beta)\cdot v_D} \tag{2.6.}$$

Where I_s is the signal current amplitude, exponentially distributed around an average amplitude and different from event to event. So the time t where signal crosses a threshold I_{th} can be written as,

$$t = \frac{1}{(\alpha-\beta)\cdot v_D} \cdot \ln \frac{I_{th}}{I_s} \tag{2.7.}$$

After the corresponding calculation (See reference [82] for detailed calculation) the simplified formula for the timing resolution of the RPC can be written as:

$$\sigma_t = \frac{1.28}{(\alpha-\beta)\cdot v_D} \tag{2.8.}$$

where,
α : First Townsend coefficient
β : Attachment coefficient
v_D : Drift velocity of electrons.

The units of v_D is cms^{-1} while the units of α and β are mm^{-1}. However the

units of σ_t will be in seconds (or nanoseconds after calculations).

2.6.3. Spatial resolution

Spatial resolution in RPCs is typically pretty good ($O(1mm)$), but it is dependent on various parameters, most notably the strip width and the mean cluster size, i.e., the number of strips hit concurrently, both of which are directly connected to plate resistivity. Indeed, the resistive coating will disperse the signal, reducing spatial resolution. And if the layer's resistance is too high, we will have issues with recharging time and voltage drop. It is then critical to find a balanced compromised value.

This chapter provides an in-depth look into single gap resistive plate chambers. However, within the context of our current configuration, our current main goal is good spatial resolution rather than time resolution. And to understand the behaviors of gas-tight RPCs detectors.

Chapter 3. Muoscope at CP3/UCLouvain

This chapter describes the construction of mini glass-resistive plate chamber. This provides information about the first muoscope prototype, including hardware and software development.

The muoscope consists primarily of two distinct parts: the RPC detector and the data acquisition system (DAQ). There are 4 identical RPC layers, each hosted in a gas-tight aluminium box and the DAQ system is integrated with high voltage power supply. Each RPC consists of two glass plates with a thickness of 1.1 mm and a gas layer of 1 mm. A uniform gap between the glass plates was obtained by placing nine-round edge spacers made of polyether ether ketone (PEEK).The readout board of the RPC is made with sixteen copper strips. Each strip is 9 mm wide and separated by a 1 mm gap, thus yielding a pitch of 1 cm. The DAQ electronics consist of two front-end boards (FEBs) borrowed from the RPC system of the CMS experiment [97, 98]. Each FEB can handle 32 analog inputs channels, each consisting of an amplifier, a discriminator, a monostable and a LVDS driver. The LVDS outputs of all the FEBs are connected to a System-on-Chip module, which is installed on a carrier board with a wireless connection (See Figure 3.1).

3.1. RPC Detector

3.1.1. Detector Casing

The casing for the RPC is an aluminium box, Figure 3.2 with dimensions of 38 $cm \times 29\ cm$ which has holes for the high voltage connector, gas inlets and a connector for readout strips. The detector casing is air-tight and in the final test with a vacuum pump, it reached the leak rate of $10^{-9}\ mbar.l.s^{-1}$ and was considered as air-tight. The leakage tests were done in both CRC, UCLouvain and UGhent. Every time the detector is opened, a vacuum grease is applied to the seal.

3.1.2. Glass plate and resistive coating

The glass plates selected for RPC was 20 $cm \times 20\ cm$ with the thickness of 1.1 mm and ordered from Verrerie Villeurbannaise. The glass plates were painted with a conductive coating in order to create a semi-resistive layer that would result in a uniform voltage distribution. CPM10C Colloidal Dispersion, which contains a colloidal dispersion of antimony-doped tin oxide in water in

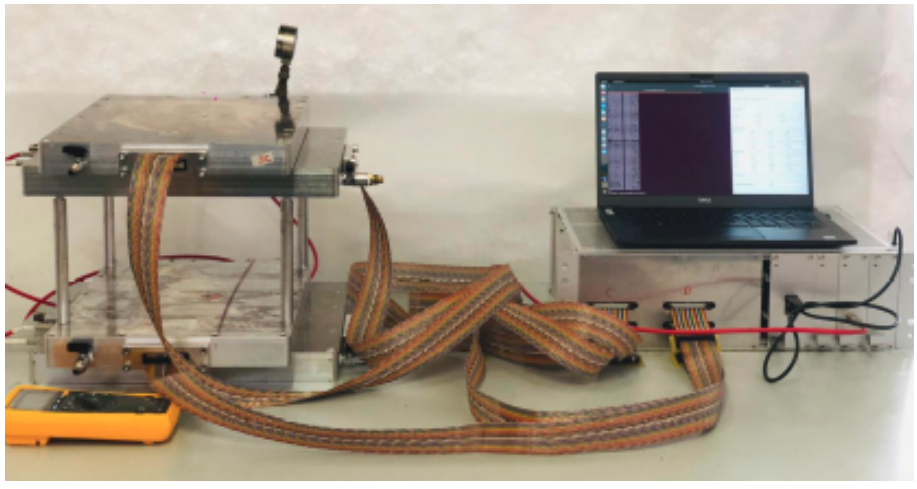

Figure 3.1. | Muoscope at CP3/UCLouvain, The four RPC layers are on the right side, and the data acquisition (DAQ) system is on the left. The four RPC layers are connected to the DAQ system with 34-wire ribbon cables. The 14-inch laptop computer is on the top of DAQ to give the reader an understanding of the size of the full setup.

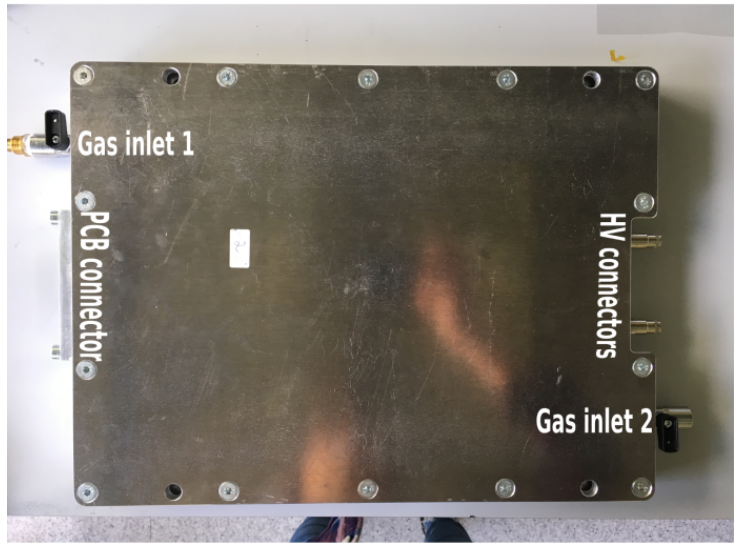

Figure 3.2. | Aluminium casing. Figure from [99].

proportions of 20% powder to 80% water, is used to create the conductive paint. The final mixture of this conductive paint and methanol (which evaporates as it is painted) contains 3 cc of each ingredient.The glass plates are evenly coated with a roller after they have been meticulously cleaned. The edge spacers are

kept out of the active area related to the strip size using a masking tape made of Kapton tape (See Figure 3.3).

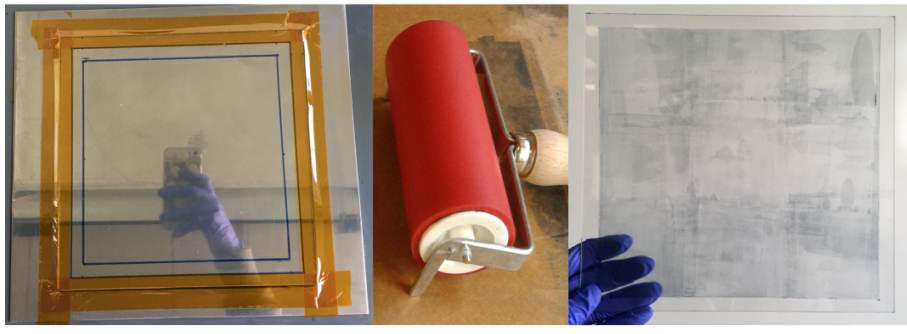

Figure 3.3. | Method to apply the resistive coating on glass plates, (left) Masked glass plate before applying paint, (middle) Roller used to spread paint, (right) Painted a glass plate. Figure from [99].

3.1.3. Spacers for gas gap

The gas gap between two glass plates are made with nine round edge spacers made in PEEK (Polyether ether ketone)(See Figure 3.4). Flat round spacers with a diameter of 2cm and 1.1mm thick and non-flat spacers are available to construct the gap between the glass plates. The latter have a thickness of 1.1mm on the outer corona and 3.1 mm on the inner corona, with a diameter of 1.1cm. They are used to wedge the glass plates in the appropriate way due to their non-flat nature. The second plate is then topped with flat spacers, and they can be screwed together inside the box. (Holes in the detector casing were provided for that).

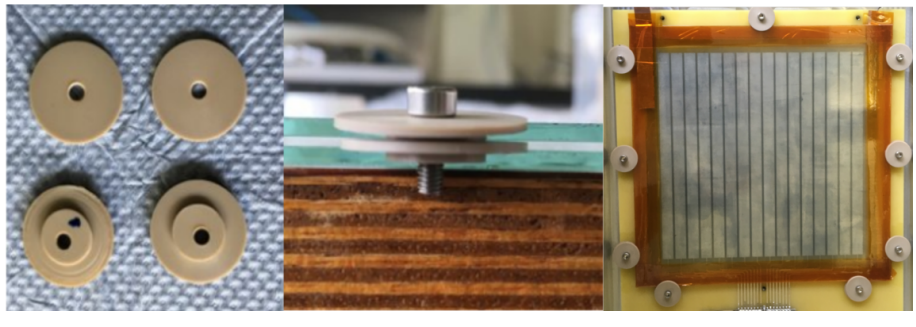

Figure 3.4. | Round edge spacers.Figure from [99].

3.1.4. Readout board (Version 1.0)

The printed circuit boards (PCB) are made up of 16 strips, each measuring 16 cm in length and having a 1 cm pitch (See Figure 3.5). A jumper is soldered on the metallic band near the readout. It is positioned there to create a connection between the readout strips and the high voltage masses. Avoiding large loops is its main goal. The holes that were bored to secure the PCB with tiny screws inside the detector enclosure were visible. For connection with a front-end board, the readout wires are attached to an adapter board. PCB piece is inter-left between the hole in the detector casing and a metallic piece.

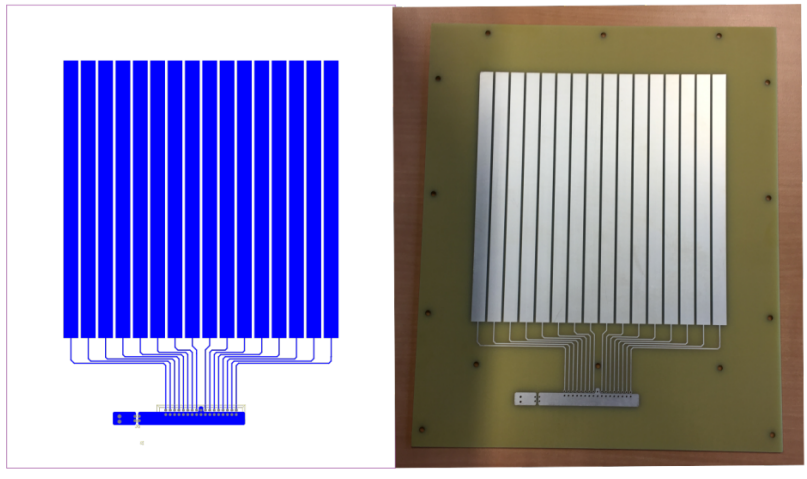

Figure 3.5. | Printed circuit board. Left : Drawing. Right : Physical PCB. Figure from [99].

3.1.5. High voltage connection

A wire compatible with high voltage is soldered between the HV connector from the gas-tight aluminium box and the copper strip glued to the resistive coating of the glass plate, figure 3.6. The same procedure was followed to connect the ground cable to the glass plate. A Kapton tape is used to insulate the inactive part of the glass plate.

3.2. Data acquisition system

The DAQ system of the muoscope consists of following sub systems.

- Computer
- FPGA+CPU module (Trenz Electronic TE0720-03-1CF, Figure 3.10) [100]
- high-voltage power supply (iseg DPS mini DPn, Figure 3.8) [101]
- CMS Front end module electronics board(Figure 3.8) [98]

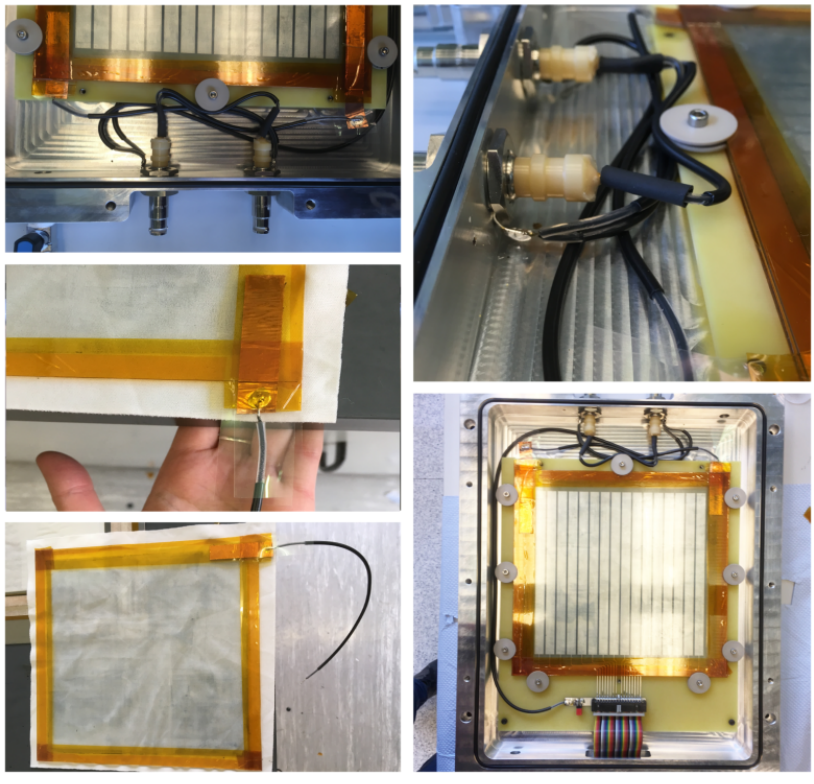

Figure 3.6. | High voltage connection.Figure from [99].

- High-voltage controller
- Digital to analog converter (Analog Devices AD5316) [102]
- Analog to digital converter (Analog Devices AD7417) [103]
- I/O expander for I2C bus (NXP PCF8574AT) [104]

3.2.1. Front End Electronics

The muoscope is consists of two front end electronic boards (figure 3.8 (left))which developed for the CMS experiment [97, 98].The electronic board first amplifies and discriminates the induced signals from the RPC readout strips, and then sends the digitised signals to the trigger electronics (FPGA) via twisted pair cables. The total of 32 channels is provided by the four chips contained in each front-end board (FEB), with each FEB being used for two chambers. Each channel is composed of an amplifier with a charge sensitivity of 2 mV/fC, a discriminator, a mono-stable, and an LVDS driver. A single-channel block diagram is shown in Figure 3.9 Each front-end board (FEB) has 4 chips, containing 8 channels which gives a total of 32 channels. Therefore

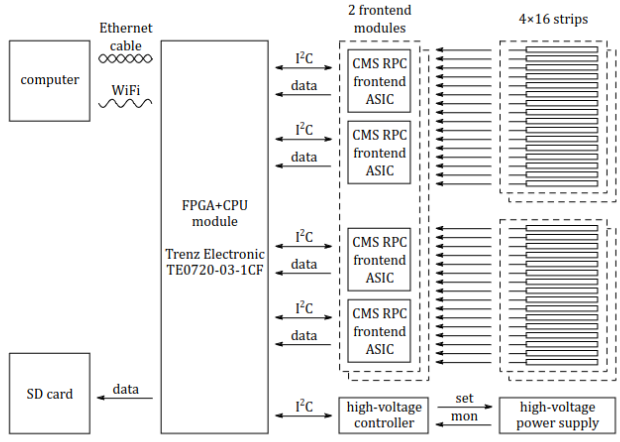

Figure 3.7. | Schematics of the RPC detector with its data acquisition system [105].

one FEB is used for 2 chambers. The discriminators is used to convert the analog RPC signal to a digital pulse and monostable creates a fixed width to the discriminated pulse. The LVDS drive convert the digitize pulse to a signal that could read by FPGA.

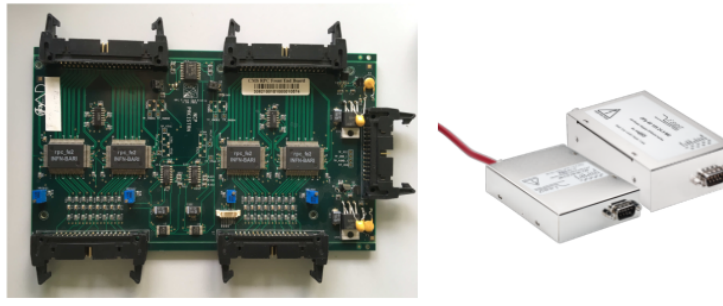

Figure 3.8. | CMS RPC front End electronic board (left) and Iseg DSP mini high voltage supply (right).

3.2.2. High-voltage controller

The high-voltage controller can control up to four high-voltage power supplies. The DAC and ADC intergrated circuits are used to control and monitor the output voltage and current of the power supply.

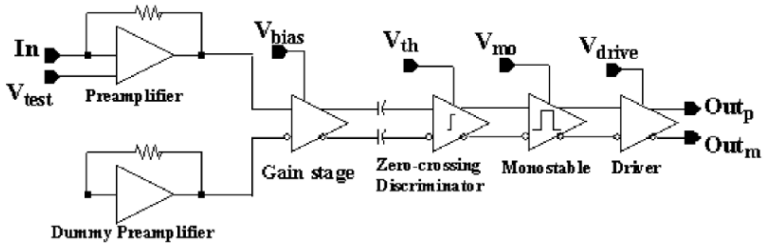

Figure 3.9. | Single channel block diagram. Figure from [97].

3.2.3. FPGA+CPU module

Figure 3.10 shows the layout of the Trenz Electronic TE0720031CF FPGA+CPU module. The Xilinx Zynq XC7X020 system-on-chip (SOC), which combines an FPGA and a dual-core ARM Cortex-A9 CPU on a single integrated circuit, is the foundation for the Trenz Electronic TE0720-03-1CF FPGA+CPU module.The coincidence-detecting algorithm and the time-to-digital converter (TDC) are implemented using the FPGA. The Linux operating system and the data gathering software can both run independently on the CPU's 1 GB of memory.It is possible to communicate to an external computer using either the on-board Gigabit Ethernet interface or a USB-connected WiFi module. The SD card is used to contain the Linux operating system, the FPGA configuration files, and the data acquisition software during data acquisition runs.

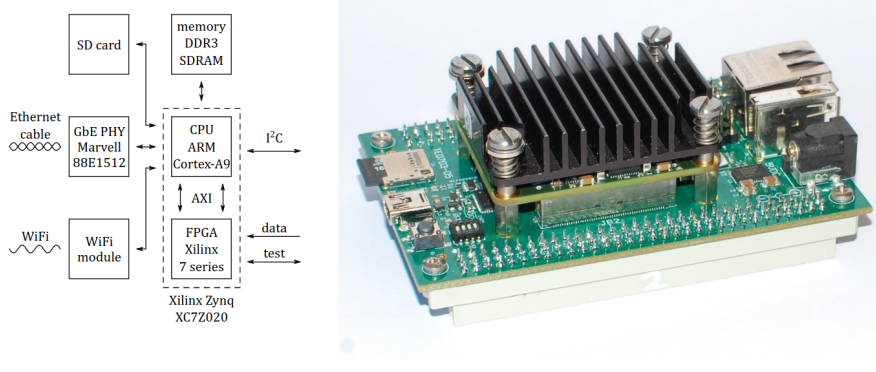

Figure 3.10. | Structure of the FPGA+CPU module [105] (left) Physical view of the module (right).

3.2.4. I2C Bus

All controllable integrated circuits on the high-voltage controller and on the front end modules are connected to the same I^2C bus which is controlled by the CPU on the FPGA+CPU module.

3.3. Software Layer

As previously mentioned (In Section 2.3),information is acquired by detecting the electrical signal produced by the avalanche of ion pairs inside the gap. A time window of 80 ns opens up after a pulse is detected, and all pulses that occur during this time are added (OR-operation between all channels combined). Pre-amplifiers must be utilised to make up for the relatively weak signals acquired in the avalanche mode due to the low electric field. The front-end electronics are located there; they are the electronics that enhance the RPCs' incoming signal and transform it into a logical signal.

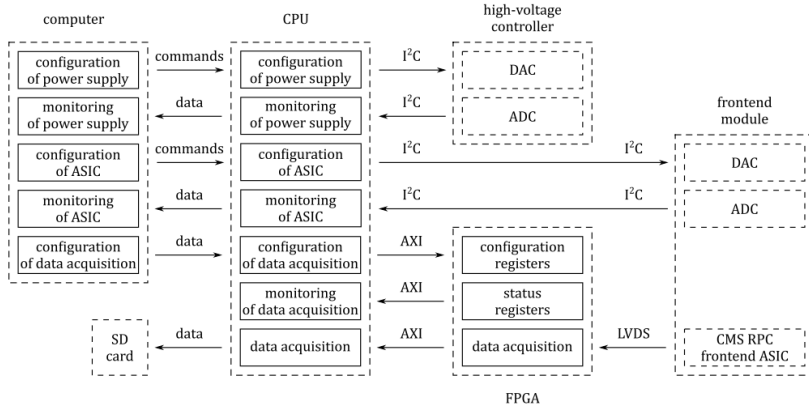

Figure 3.11. | Software subsystems of the data acquisition system.

As shown in the figure 3.11 there are few subsystems in the logical layer. The external computer is used to connect to the DAQ via Ethernet port or WiFi. There is a GUI to control the DAQ, or it can be done using command lines via the terminal. The computer sets the threshold and mono-stable values for data acquisition and the high voltage value, and also monitors set values. After getting commands from an external computer, the CPU inside the DAQ sends HV values to the high voltage controller, threshold and monostable values to CMS FEE (See section 3.2.1), and configures the FPGA for data acquisition. After data acquisition starts, the CPU monitors the acquisition and stores the data on the SD card.

Chapter 4. External scintillator trigger

In the first prototype of the muoscope, there was no trigger system to start the data acquisition process. It was operated in self-trigger mode, which starts the data acquisition when there is a hit in the first layer of the RPC stack (typically Chamber A or the top layer). But with this configuration,It is difficult to properly characterise the RPCs and understand their performances in the assessment of large noise.

This section gives a detailed discussion about the external scintillator setup.

4.1. Design and production

The basic idea of the external scintillators was to place them top and bottom of the muoscope. So initially two identical scintillators were designed and produced. The main features of the trigger setup are follows:

- Portable, to be used out door if needed.
- Should cover the active area of the RPC.
- The Photo multiplier tube (PMT) could be powered with low voltage.

With all the key features mentioned above, the final design included following features:

- A plastic scintillator (16 cm $\times$ 16 cm $\times$ 2.9 cm).
- A black plastic housing with mounting mechanisms for PMT, (See figure 4.1)
- Hamamatsu H11411 Photo-multiplier tube.

4.1.1. Housing for Scintillator

The housing, a plastic box for the plastic scintillators, was designed by Nicolas Szilazi (The mechanical engineer of CP3). The cross section of the housing is in the figure 4.2. The white box is the plastic scintillator hosted inside the box. Four plastic pillars are placed on the bottom corners of the box, and a rectangular piece is mounted to the cap of the box to hold the scintillators. On one side, a hole with a diameter of 6 cm is connected to a 3D-printed frame to mount the Hamamatsu H11411 PMT. The bottom of the housing has four holes, which match the holes in the aluminium box (Figure 3.2), so the scintillators would be exactly on top of the active area of the RPC. In order to mount the PMT properly, a spring mechanism is used with long screws (see figures 4.2,

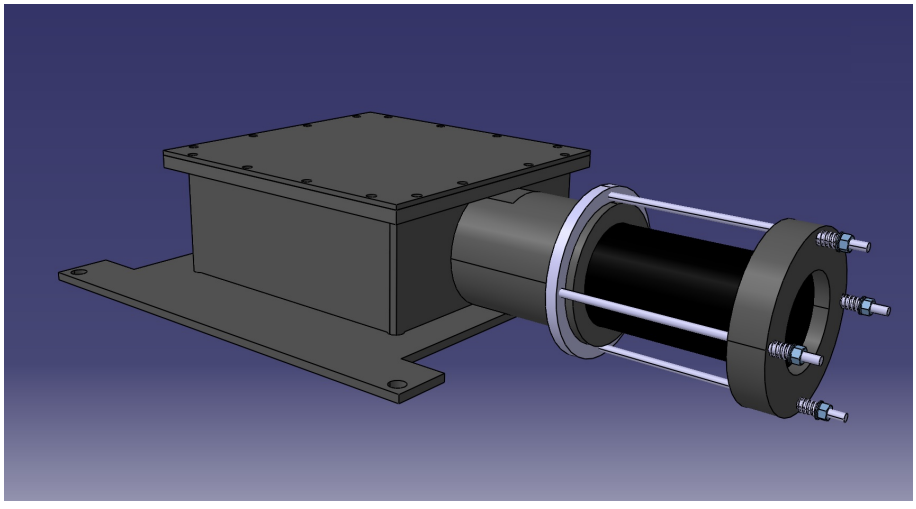

Figure 4.1. | CAD model of the external look of the final design of the external trigger setup.

4.1).

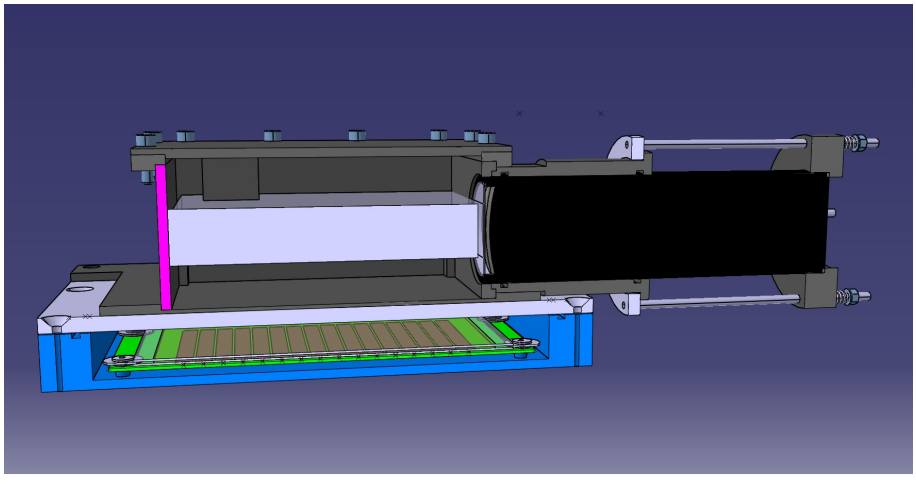

Figure 4.2. | The cross section of the housing for the trigger scintillator.

4.1.2. Hamamatsu H11411 Photo-multiplier tube

The H11411 is a photomultiplier module that combines a high-voltage power supply circuit with a 51 mm diameter head-on photomultiplier tube. With a 46 mm diameter effective photo-cathode area. As this PMT is integrated with a high-voltage supply, to control the gain, it only needs a control voltage supply varying from 0.5 V to 1.8 V. The exact control voltage has to be calibrated with

the experimental data. The photocathode is sensitive to light with a wavelength of 300 nm to 600 nm. A circuit was designed with a potentiometer to power the PMT and set the control voltage (see section 4.1.3).

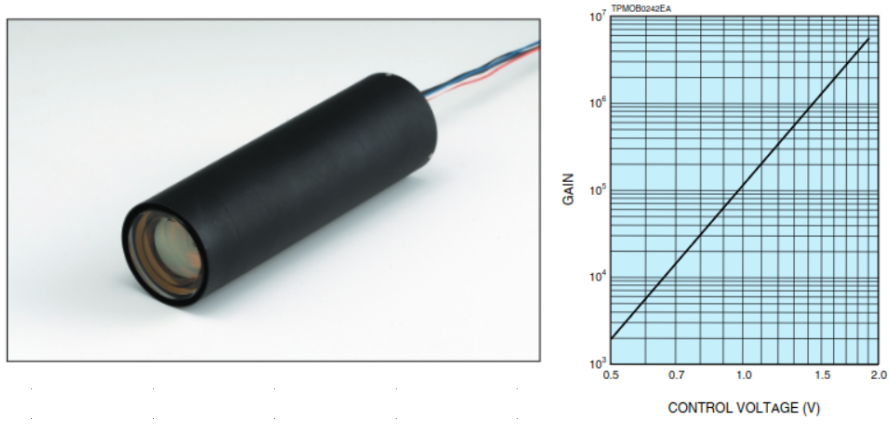

Figure 4.3. The Hamamatsu H11411 photomultiplier module (left) and the gain of the PMT with respect to the control voltage (right) [106].

4.1.3. Potentiometer board for PMT

The purpose of this unit (Figure 4.4) is to power up the PMT and adjust the control voltage of the PMT. It consists of two banana female connectors, which could power the system with a power supply of +15 V and a 67WR500KLF trimmer potentiometer [107] that could be adjusted by a screwdriver in order to change the control voltage of the PMT and a 71251-040/0800 DIN female connector [108] which is compatible with a DIN 4 male connector. This was designed and produced in the CP3 Electronic lab. There is a pin to monitor the control voltage via voltmeter.

4.1.4. Assembly process of the trigger system

The system was produced and assembled over the course of several steps. In the first stage, two plastic housings were created, and two plastic scintillators were cut to specific measurements, polished for greater light transmission, and examined with RPCs for any light leaking through corners. This was done in the Cyclotron workshop at UCLouvain.

Next, white reflecting sheets were wrapped around the polished scintillators, excluding the hole for the PMT, to improve the scintillating light's reflection towards the photocathode. The little pillars were affixed to the plastic box's bottom corners to ensure that the scintillator was positioned correctly.

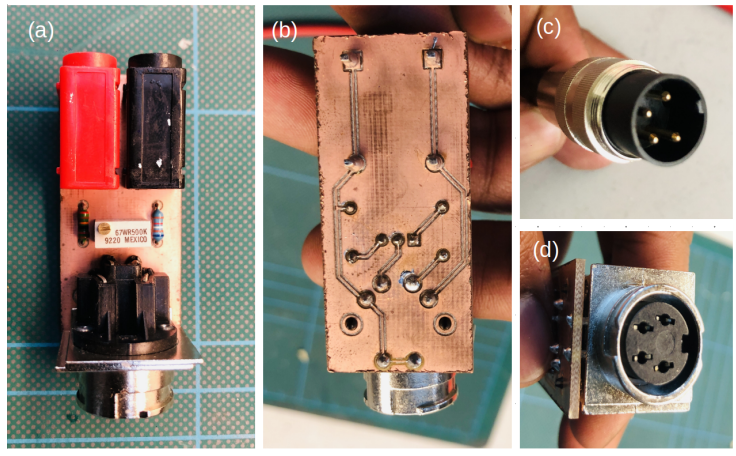

Figure 4.4. (a) potentiometer board with banana connectors (red and black color) and DIN female connector, (b) rear view of the board, (c) DIN 4 male connector, (d) 71251-040/0800 DIN female connector.

The photocathode was treated with optical grease in the final phase, and the PMT was fastened to the box with long screws. Optical grease is used to improve optical contact between the PMT's scintillator and photocathode. The box's cover is put in place and fastened using 16 nuts and bolts after the PMT has been fixed. Black tape was used to seal up all edges to prevent light from passing through. The final product is shown in figure 4.5.(d). Two identical systems were assembled.

4.2. Testing and Calibration

After assembling the two scintillator detectors, the next stage is to calibrate the system and evaluate the output signal of the PMT for cosmic muons.

There are 2 main key calibrations to be done before introducing this trigger system to the muoscope.

- Control voltage calibration.
- Threshold calibration for the discriminator.
- Efficiency of two scintillators.

For this, the following modules and instruments were used.

- QL355TP dual channel power supply. [109]
- LeCroy quad discriminator (Model 821CS) module
- LeCroy quad coincidence (Model 622) module
- CAEN N415A 8 Ch autowalk constant fraction discriminator(CFD) [110]
- Dual timer (IPC type 2255 series)
- Two dual scalers (IPC type DS2)

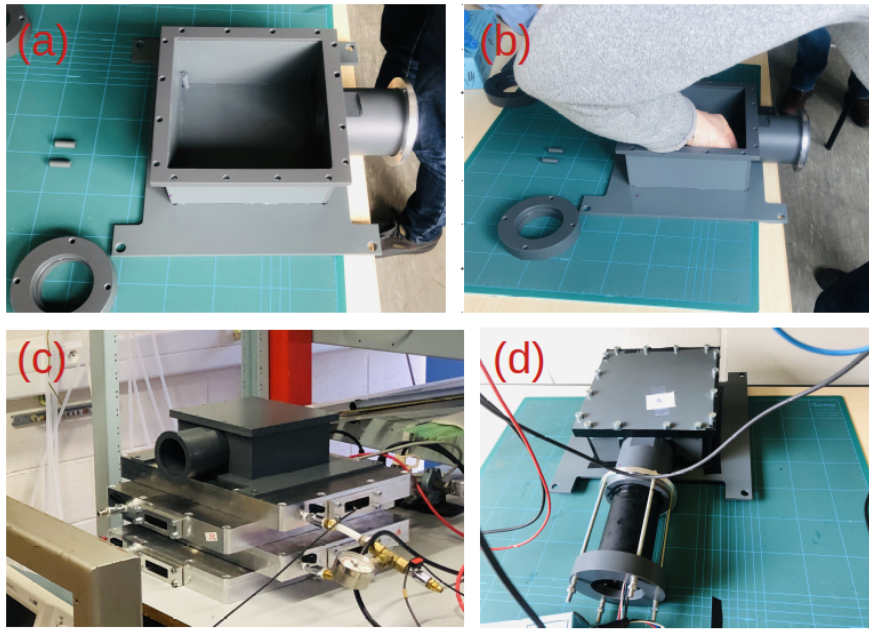

Figure 4.5. | Assembly process of the external trigger.

- Preselection timer counter
- NIM power supply (IPC NPS 100)
- Teltronix TDS 3014 four channel digital oscilloscope [111]
- LEMO cables and onnectors
- delay module
- Two Hamamatsu R9800 PMT + 10 cm× 10cm scintillators
- CAEN HV supply

4.2.1. Initial signal test

Two scintillators were named "top (A)" and "bottom (B)" to distinguish them separately. Then both top and bottom were powered by the QL355TP dual-channel power supply, which has two separate voltage outputs. The control voltage was set to 1.75 V (the reference value of the data-sheet [106]) for each. The output of the PMT was connected to the Teltronix TDS 3014 four channel digital oscilloscope using a standard LEMO connector. The signal observed for the cosmic particles is shown in figure 4.6.

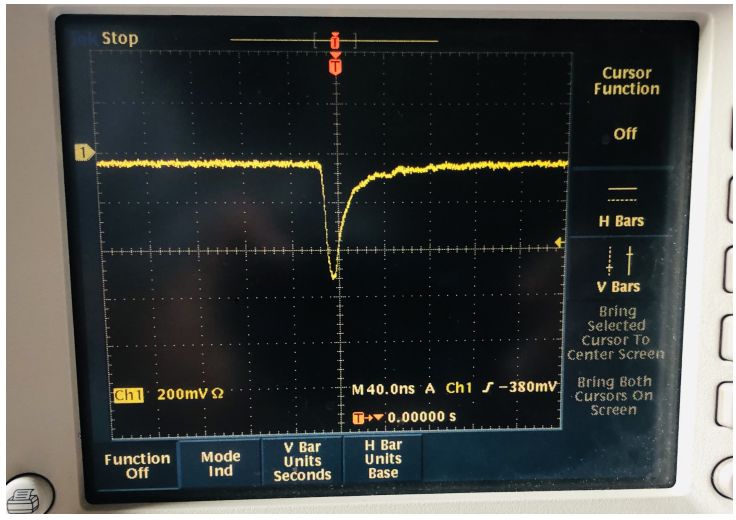

Figure 4.6. | Oscillogram of the scintillator signal of Top(A) PMT . The input impedance of the oscilloscope is 50Ω , voltage scale is 200 mV/square, and the time scale is 40 ns/square. The trigger of the oscilloscope is set to -380 mV.

4.2.2. Coincidence circuit

The coincident circuit was designed with two PMTs in order to evaluate the trigger system's performance. Two scintillator boxes were kept one above the other as in the figure. The readout was created using NIM electronics for ease of use. Figure 4.9 depicts the circuit diagram of the coincidence circuit with two scintillators and a PMT arrangement. After initial PMT signal testing, the two signals are sent to the LeCroy quad discriminator (Model 821CS) module for digitization. However, it has been determined that PMT B is faster than PMT A, so the signal from PMT B must be delayed. Nevertheless, the time delays span from 15 to 35 nanoseconds and are not stable. A delay of 18–20 ns was obtained after using the CAEN N415A 8 Ch autowalk constant fraction discriminator (CFD) (see figure 4.8(left)).

The signals are in the same time window after the delay has been adjusted (See figure 4.8). Then, the coincidence module was provided with two signals. The coincidence window's time window was adjusted to 70 ns (Figure 4.10). And the setup is ready for the calibration of control voltage.

4.2.3. Calibration of control voltage

In counting applications in which the photomultiplier signal is analysed by a discriminator, a straight forward method for determining the working voltage is to conduct a so-called plateau measurement. This entails measuring the total count rate from the counter-discriminator as a function of the applied

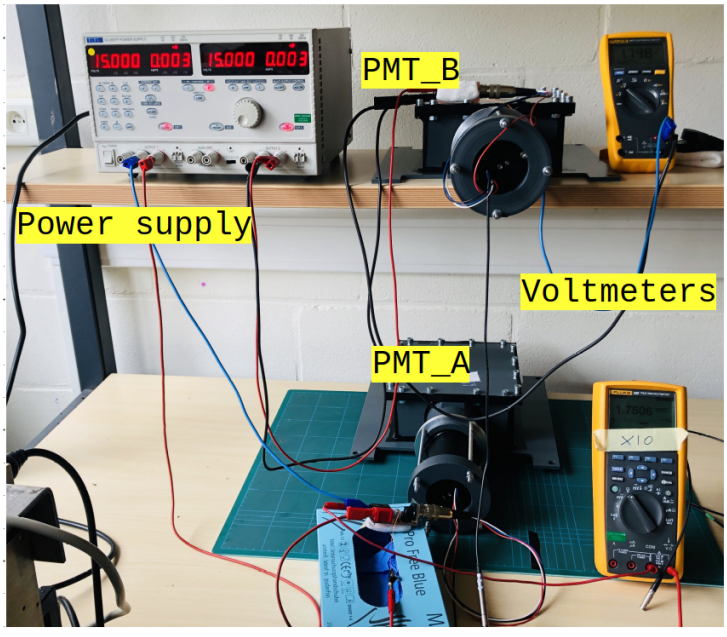

Figure 4.7. | Orientation of two scintillator setup for coincidence measurements.

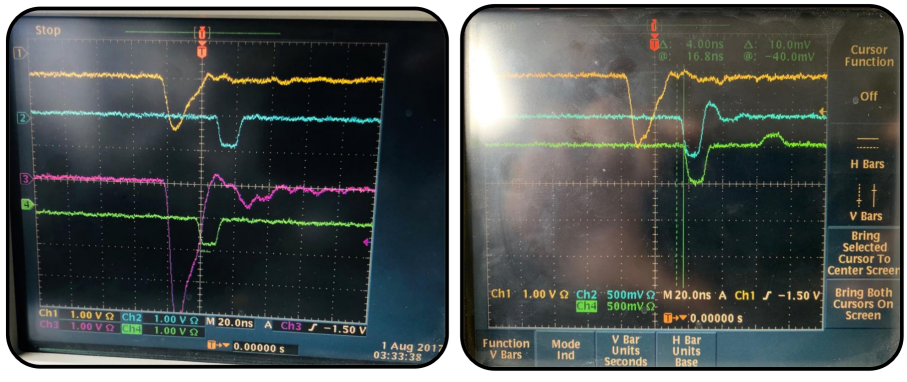

Figure 4.8. | Analog and digitized signal before the delay. Blue and green lines are digitized signal using discriminator (left). The two digitized signals with delay of 20ns in the digitized signal (green) of PMT B (right). control voltage was set at 1.75 V and threshold of the discriminator was at - 1.5 V.

photomultiplier voltage, similar to the plateau curve for Geiger counters [112]. With the external trigger setup (Schematics in figure 4.9) and an additional timer the number of coincidence were taken for 2 cases, while threshold value of the discriminators were set to following values. The experimental setup was

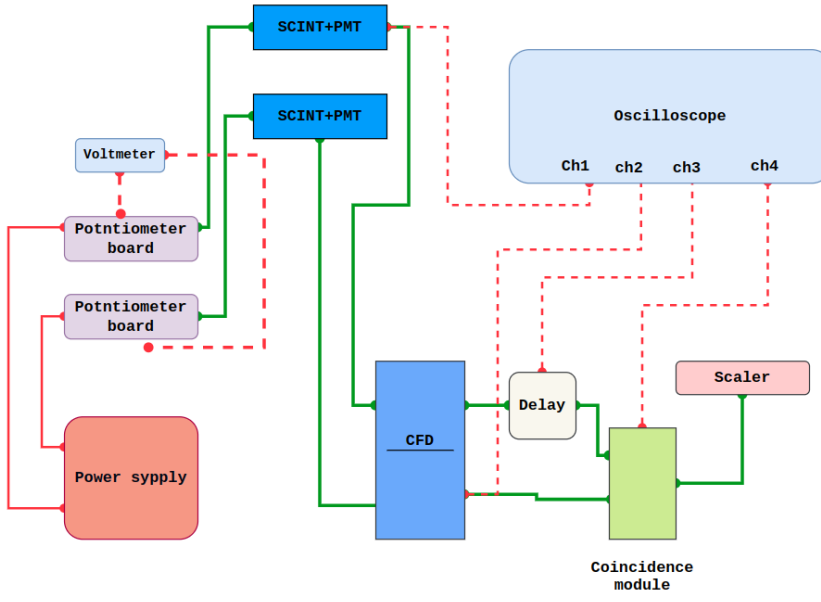

Figure 4.9. | Schematics of a Coincidence Circuit with Two Scintillator + PMT Setup.

Figure 4.10. | Coincidence window (pink) of 70 ns with two digitized signal from PMT.

changed w.r.t setup in figure 4.7, by changing the distance between 3 scintillators for maximum solid angle. The experimental setup is in the Figure 4.11.

Table 4.1. | Setup values of each NIM unit.

PMT	(Threshold ± 0.001)/V
A	1.062
B	1.042

Case 1 : The control voltage of the PMT A was set to 1.8 V, which is the upper limit for the H11411 PMT. Then the total number of coincidences between two PMTs was counted for 100 seconds while changing the control voltage of B from 0.5 V to 1.8 V.

Case 2 : The control voltage of the PMT B was set to 1.8 V, which is the upper limit for the H11411 PMT. Then the total number of coincidences between two PMTs was counted for 100 seconds while changing the control voltage of A from 0.5 V to 1.8 V.

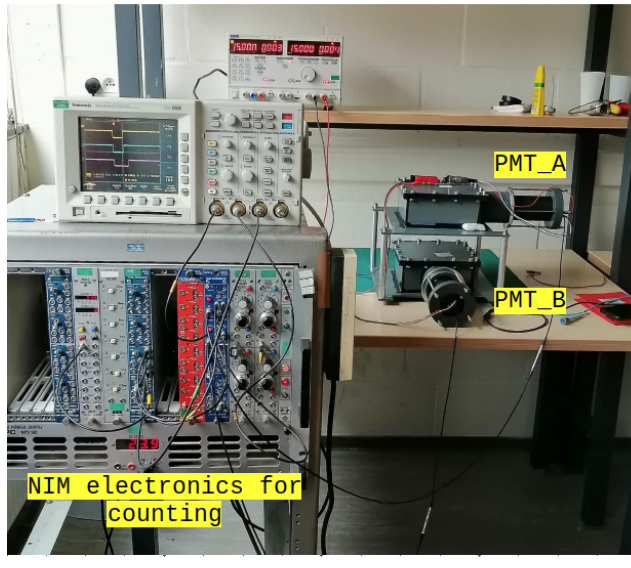

Figure 4.11. | Setup for the calibration for the control voltage.

The control voltages were measured from the plateau of the graph of control voltage vs coincidences (See figure 4.12).

Control voltage of A = 1.25 V (middle point of the plateau)

Control voltage of B = 1.25 V (middle point of the plateau)

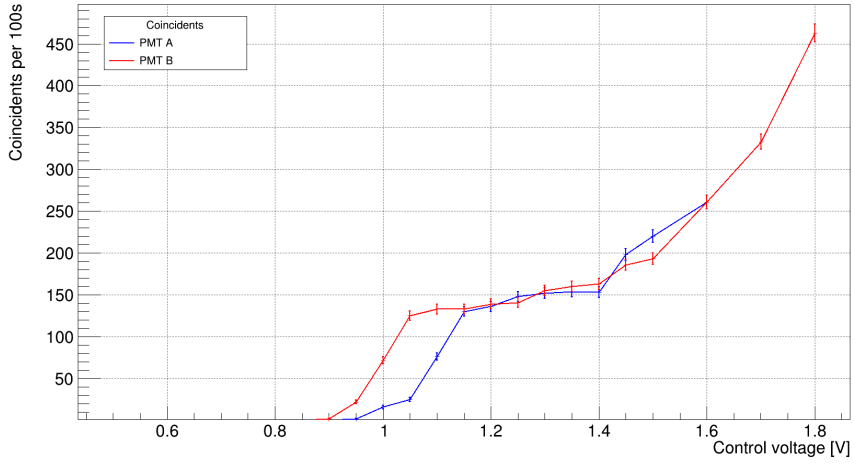

Figure 4.12. | Graph of control voltage vs the coincidences counts for both PMTs. The lower limit of plateau of B, 1.05 V and upper limit is 1.4 V. The lower limit of plateau of A, 1.15 V and upper limit is 1.4 V.

4.2.4. Calibration of discriminator threshold

After fixing the control voltage to 1.25 V, the next test was done to find the optimal value for discriminator. The experiment was done in two cases:

Case 1 : The discriminator threshold of the PMT A was set to - 0.3 V (which corresponds to -30 mV), which is the lower limit of the LeCroy quad discriminator (Model 821CS) module. Then the total number of coincidences between two PMTs was counted for 100 seconds while changing the threshold value of discriminator of PMT B.

Case 2 : The discriminator threshold of the PMT B was set to - 0.3 V (which corresponds to -30 mV), which is the lower limit of the LeCroy quad discriminator (Model 821CS) module. Then the total number of coincidences between two PMTs was counted for 100 seconds while changing the threshold value of discriminator of PMT A.

The coincidence plot can be seen in the figure 4.13 the counts don't vary dramatically from -0.3 V to -1 V, so we decided to use -0.5 V as the threshold value.

4.2.5. Efficiency of PMTs

Since the threshold value and control voltage of the PMTs are fixed, the next step is to calculate the efficiency of the PMTs separately. For this purpose, two sets of Hamamatsu R9800 PMT + 10 cm× 10cm scintillators were used. The setup is simple. Both Hamamatsu R9800 were already calibrated for the high

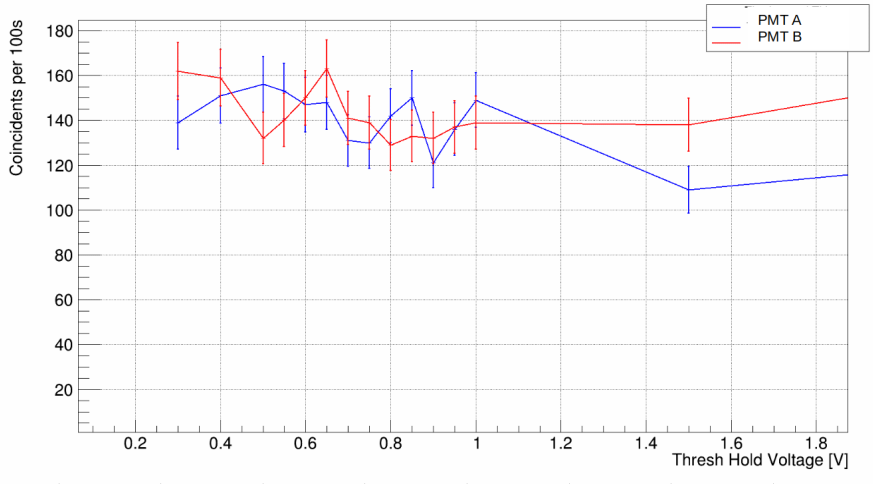

Figure 4.13. | Graph of discriminator threshold vs the coincidences counts for both PMTs.

voltage and threshold values. For ease of use, they were named "Top" and "Bottom", which are placed at the top of trigger setup A and below trigger setup B, as in figure 4.14. The LeCroy quad discriminator (Model 821CS) module was used to set the signal threshold for both PMTs. High voltage was supplied by the CAEN HV module.

Table 4.2. | Setup values of PMT units for efficiency calculation.

Scintillator+ PMT	Threshold/V	High voltage/V
Top (10cm× 10cm)	- 0.4978	1450
A (16cm×16cm)	- 0.5018	1250(*)
B (16cm×16cm)	- 0.5006	1250(*)
Bottom (10cm× 10cm)	- 0.5030	1450

(*) This is the high voltage corresponding to the control voltage of 1.25 V in PMT [106]

The coincidence circuit was made as similar to the section 4.2.2 for coincidences between the following detector configurations.

- Coincidence between Top and Bottom
- Coincidence between Top, Bottom and A
- Coincidence between Top, Bottom and B

Timer was set to 30 minutes. The total counts were recorded and efficiency was calculated.

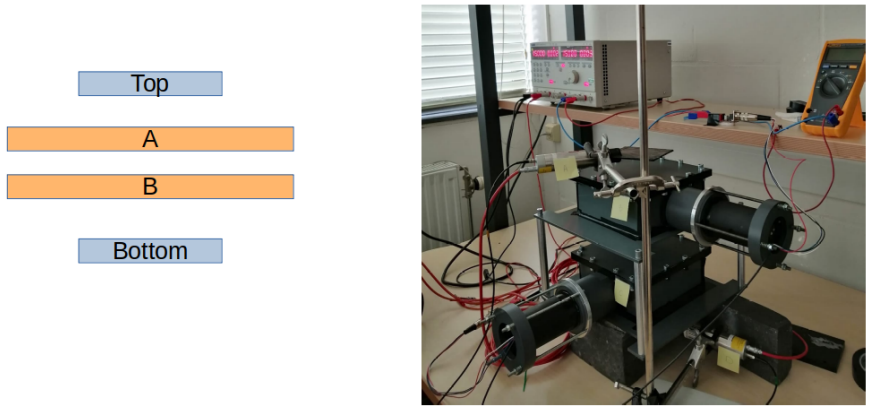

Figure 4.14. | Arrangement of PMT for efficiency measurement of the two scintillators.

Table 4.3. | Experimental values for efficiency calculation

	Top & Bottom	Top & Bottom & A	Top & Bottom & B
counts	169	156	153

$$Efficiency_A(\epsilon_A) = \frac{Top \cap Bottom \cap A}{Top \cap Bottom} \times 100\% \quad (4.1.)$$

$$Efficiency_B(\epsilon_B) = \frac{Top \cap Bottom \cap B}{Top \cap Bottom} \times 100\% \quad (4.2.)$$

Table 4.4. | Efficiency of PMTs

Scintillator + PMT	Efficiency(%)
A	93.30 ± 0.92
B	90.53± 1.11

4.3. External Trigger with RPC

Implementing the external trigger system within the RPC was the next step for the system. Before connecting it to the muoscope's data acquisition system, the delay between the RPC and PMT signals is measured, as the RPC signal is faster than the PMT signal.

There are two unused I/O pins in the FPGA [100]; two wires were soldered to the FPGA board to be used as inputs for the signals of two PMTs. The signals

of the PMTs were discriminated by the CAEN CFD module [110]. Then the discriminated signal was fed to the timer module to use it as a monostable. The monostable signal was converted to an LVDS signal using an LVDS drive to feed it to the FPGA in the DAQ system.The 2 signals from monostable unit and LVDS units are shown in the Figure 4.16.

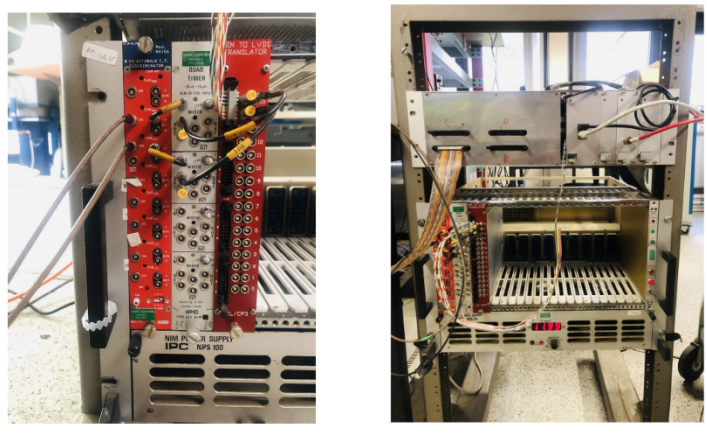

Figure 4.15. | Three modules used for connect external trigger to DAQ (left). The electronic setup DAQ system with external trigger (right).

In the DAQ software, the 2 least significant bits of the time buffer was used to store data from 2 PMTs. The mono-stable value was set to 40 ns after verifying the signal was acceptable for FPGA in DAQ (Figure 4.16). The PMT counts were performed on the same data set using both a DAQ and an external NIM counter to confirm the system's functionality. The data in the Table 4.5, verified the DAQ system reads PMT counts properly.

Table 4.5. | DAQ and External counters hits.

Counter	Top PMT	Bottom PMT	coincidence
DAQ	2470	3511	614
NIM Ex. counter	2474	3512	614

The changes made with the DAQ programs to implement the external trigger is discussed in the performance study section.

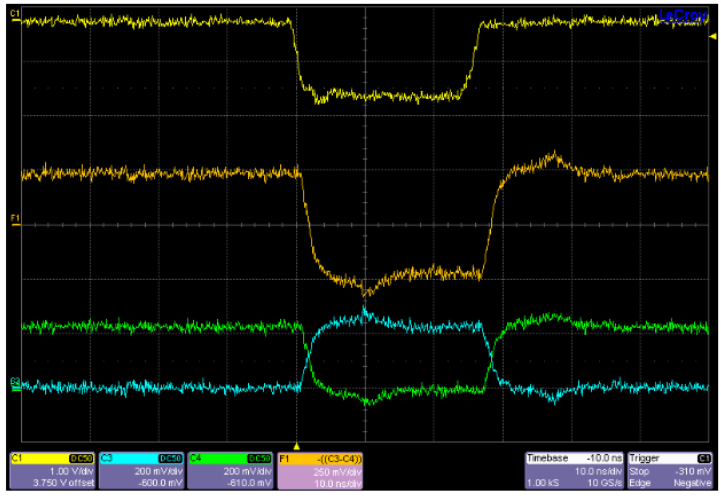

Figure 4.16. | Oscillogram of the LVDS output and monostable output. In the channel 1 (Yellow), it shows the output from monostable and in channels 3 and 4 (blue and green respectively) shows to output from 2 lines of LVDS module.

5. Chapter
Resistive plate production

5.1. Surface resistance and Surface resistivity

"Surface resistance and surface resistivity, also referred to as sheet resistivity, are characteristics of materials typically used to describe insulators or semiconductors. These two concepts can be confusing at times. In this section, we will provide a brief introduction and explanation of both surface resistivity and surface resistance because they play a significant role in the production of RPC.

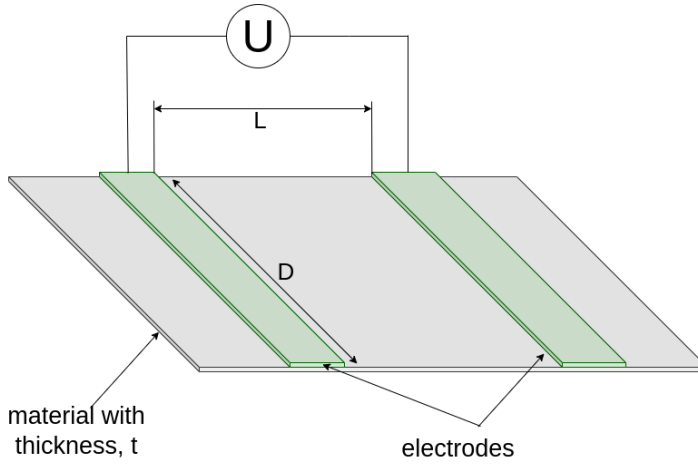

Figure 5.1. | Basic setup for surface resistance and surface resistivity measurement [113].

Surface resistance, R_s is defined as as ratio of a DC voltage U to the current, I_s flowing between two electrodes of specified configuration that are in contact with the same side of a material under test (Figure 5.1) [113].

$$R_s = \frac{U}{I_s} \tag{5.1.}$$

And surface resistivity ρ_s is determined by the ratio of DC voltage U drop per unit length L to the surface current I_s per unit width D.

$$\rho_s = \frac{\frac{U}{L}}{\frac{I_s}{D}} \tag{5.2.}$$

From the equations 5.1 and 5.2, it is obvious that the physical units of both surface resistance and surface resistivity unit are same Ohm (Ω), in order to distinguish between the both, the surface resistivity is frequently stated in Ohm/square(Ω/□), which is not a valid unit from the dimensional point of view.

The concepts of current density (J) and surface current density (J_s) is useful when deriving a relationship between the surface resistance and surface resistivity. Consider the two samples made of same material with different dimensions (Figure 5.2), the current flow through two sample is different under the same voltage, U. But when the voltage remains constant, the current passing through a unit area perpendicular to the flow direction remains the same.

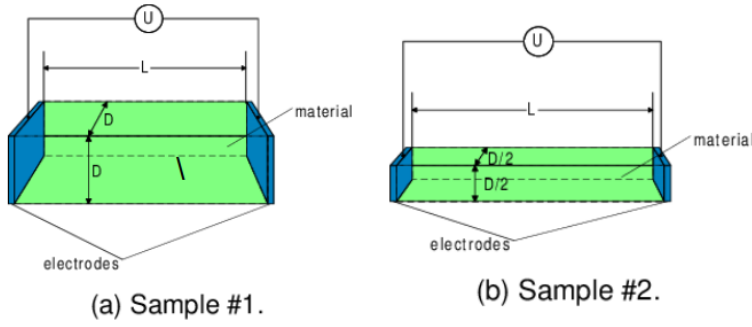

Figure 5.2. | Current density [113].

The current density (J) can be expressed as following when the voltage keeps at constant value:

$$J = \frac{I}{S} \tag{5.3.}$$

Where I is the current following and S is the Surface area perpendicular the flow and J is measured in $A \cdot m^{-2}$. Let's consider the Figure 5.1, since both electrodes are in the same side, it's assumed that current only flows through the surface. In reality current passes through the bulk of the material, but we consider **extremely thin material (Where, $t << D$)**, so the thickness can be neglected. So the surface current density (J_s) is defined as:

$$J_s = \frac{I}{D} \tag{5.4.}$$

where D represents the width of the electrode, while t corresponds to the thickness of the material used to measure the surface resistance.

5.1.1. Surface resistivity and surface resistance measurements using concentric ring probe

By determining a surface current density in the space between rings, it is possible to determine the relationship between surface resistivity and surface resistance for a concentric ring probe design. The electric field intensity between the electrode rings can be calculated from the surface current density (Figures 5.3(left)). Where,

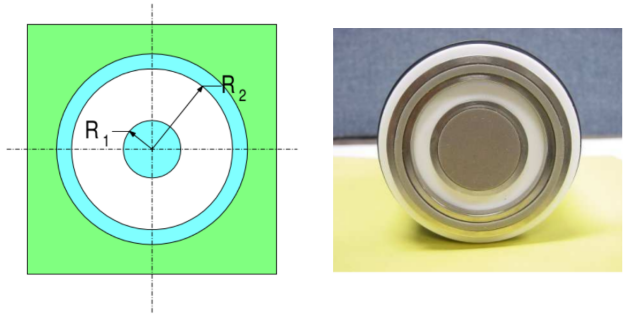

Figure 5.3. | Surface resistivity and resistance measurement configuration for concentric electrodes (left). Concentric ring probe (right) [113].

R1: Outer radius of the center electrode. **R2**: Inner radius of the outer electrode.

Surface current density (J_s) of the concentric ring electrodes can be written as, I_s is the surface current.

$$J_s = \frac{I_s}{2\pi r} \tag{5.5.}$$

radius r varies from R1 to R2. The relationship between a current density J and an electric field intensity E is described by Ohm's law. Also valid surface currents:

$$J_s = \frac{E}{\rho_s} \tag{5.6.}$$

From equations (5.5) and (5.6). the E could be written as,

$$E = \frac{\rho_s I_s}{2\pi r} \tag{5.7.}$$

The voltage ($U_{R1,R2}$) between electrodes can be found by integrating the electric field E from R1 to R2 :

$$
\begin{aligned}
U_{R1,R2} &= \int_{R1}^{R2} E.dr \\
&= \int_{R1}^{R2} \frac{\rho_s I_s}{2\pi r}.dr \\
&= \frac{\rho_s I_s}{2\pi} \ln \frac{R2}{R1}
\end{aligned}
\tag{5.8.}
$$

we can write that,

$$R_s = \frac{U}{I_s} \tag{5.9.}$$

From equations (5.8) and (5.9;)

$$R_s = \frac{\rho_s}{2\pi} \ln \frac{R2}{R1} \tag{5.10.}$$

After the equation is rearranged, the surface resistivity is related to the surface resistance by a constant that depends only on their shape or geometry.

$$\rho_s = R_s \frac{2\pi}{\ln \frac{R2}{R1}} = R_s.k \tag{5.11.}$$

We could purchase probes on the market that are made to have a **k** value with a straightforward integer. The probe we use at CP3 Lab, for instance, has a coefficient factor of 10.

5.2. Resistive Plates version 1.0

These are the plates used in the first prototype of muoscope. The resistive paint is coated in by a hand roller in CP3 lab. The detailed description of the production of the resistive coating on the glass plate is included in the section 3.1.2. As seen in the figure 3.3 the resistive coating is not uniform, and so the resistivity of the glass plates was not uniform. This results in a non-homogeneous electric field in the air gap and affects the behaviour of the RPC.

5.3. Resistive plate version 2.0

The 1^{st} generation of resistive plates (version 1.0) has a tendency to provide some unfavourable non-uniformity in the coating quality (layer thickness, resistivity value), which is known to have a negative impact on gRPC performance.The second version of resistive plate was done using a method called Serigrphy at CEA, Saclay in France.

In serigraphy, also known as screen-printing, paint is transferred using a mesh to a surface, in the current instance, glass plates, with the exception

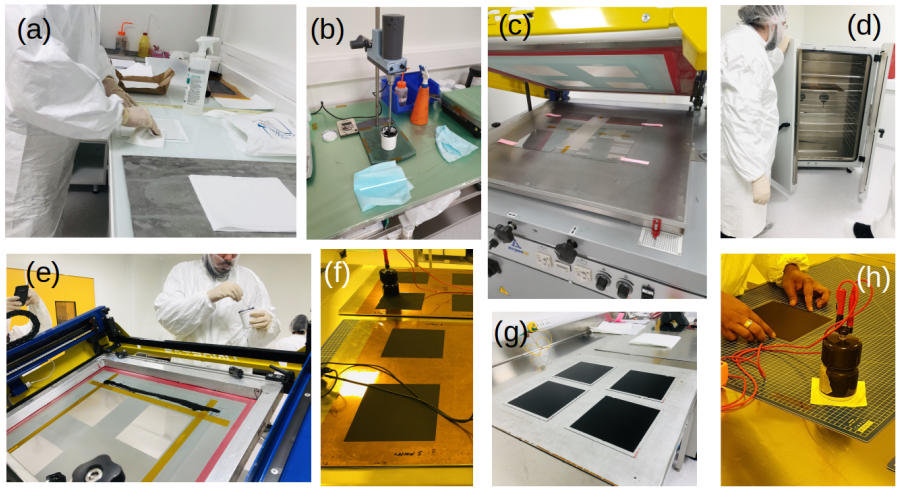

Figure 5.4. | Production process of the resistive plate in Serigraphy Method. (a) Cleaning glass plates with methanol before placing in the serigraphy machine. (b) Mixing two components of the resistive paint. (c) glass plates are placed in the serigraphy machine. (d) Placing painted glass places in the oven. (e) Poured paint on the mesh of the serigraphy machine. (f) painted Kapton sheets (g) glass plates after painted. (h) Measuring the surface resistance.

of the parts where the stencil has been blocked to prevent the paint from penetrating. We recently acquired glass plates with uniform resistive layers using the Saclay, France, CEA facility. Making the conductive compound, or paste, is the initial step in applying coating with serigraphy. To generate this paste, conductive EDAG PM 404 and the neutral EDAG 6017SS component were combined. By altering the quantity of conductive component in the mixture and measuring the ensuing surface resistivity, which is shown in conjunction with an exponential fit in the Figure 5.5, it is possible to identify the precise amount of each component in the mixture. 10.5% conductive component was added to the formulation for our glass plates to achieve a surface resistance of 2 $M\Omega/\square$. After the mixture is prepared, serigraphy is done on a kapton sheet before moving on to the glass surface. The glass is then cured for 4-5 hours at 180°C in a oven. Nine separate locations in the glass were used to test the surface resistivity; a sample measurement is displayed in figure 5.6.

5.3.1. Long term study of the surface resistivity

We produced 8 glass plates with 2 $M\Omega/\square$ and studied the variation of surface resistivity for a long term. The surface resistivity was measured in 9 different places in the glass plate (See 5.12(right)) and the temperature and humidity of the lab was measured when the resistivity was measured.

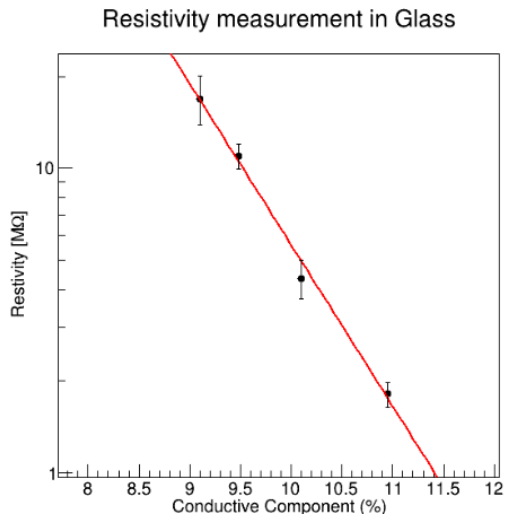

Figure 5.5. Surface resistivity (in MΩ) as a function of conductive component of the paste (in%). The black data points are used for fitting, resulting in the solid red line with equation $R = 13.94.e^{-1.22}$. This graph is used to determine the quantity of the conductive component needed to achieve a specific desired resistivity.

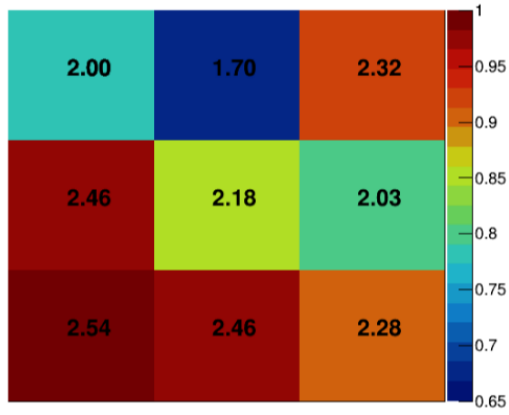

Figure 5.6. Surface resistivity (in $M\Omega/\square$) measurement for one of the glass plates at 9 different locations. In color code 1 represents the highest value of the resistivity measurement in the plate.

Being interested in long-term variations of surface resistivity, eight selected glass plates are being measured since February 2020 in order to check the stability of the resistivity with the time and with respect to the environmental conditions, i.e. temperature and humidity. We present out data in figure 5.7.

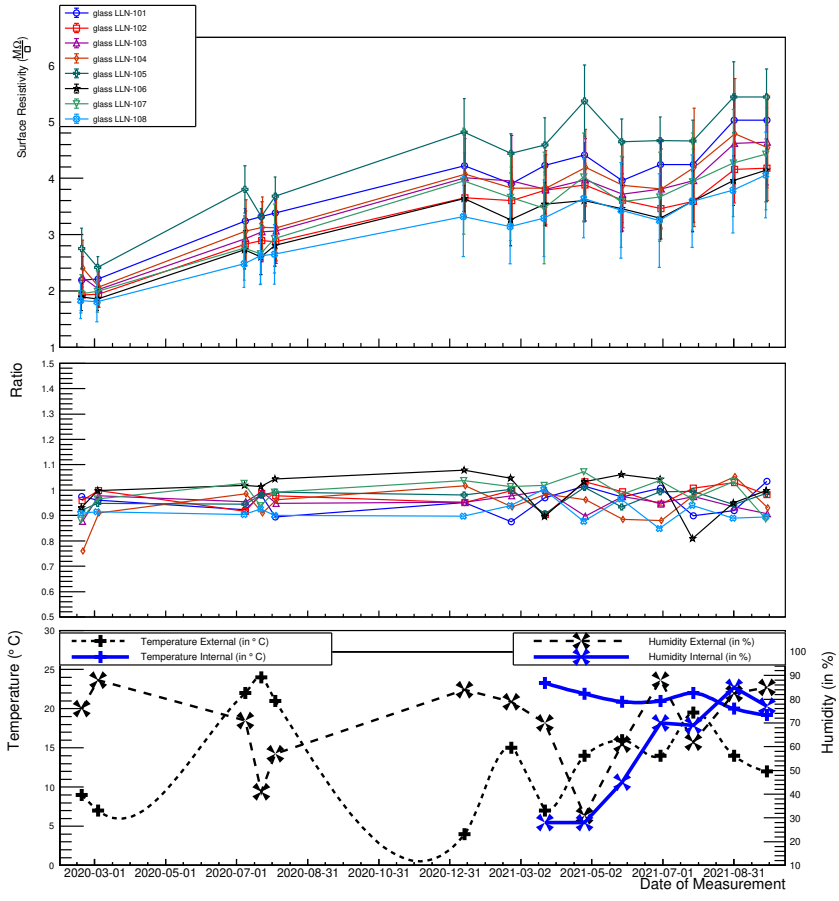

Figure 5.7. | Evolution with time of the following observable of interest. Top: average surface resistivity of eight selected glass plates. The vertical bars represent the standard deviations of the measurements at nine different locations on the same plate. Middle: ratio, for each of the same glass plates, between the resistivity at the center and the average resistivity of the other eight locations. Bottom: temperature and humidity as measured externally (i.e. data from the local weather casting) and internally (i.e. data from an internal Arduino-based sensor).

The large gaps in the time axis are due to Covid-19 pandemic lockdown in Belgium, that limited the access to our laboratory.

The top panel shows, for each glass plate and for each time, the average and standard deviation of the nine different measurements. A clear upward trend is visible with time. Given the interest in spatial uniformity, in the middle panel we show the ratio of the surface resistivity of the central region of each plate to the average of the other eight regions of Figure 5.12(right). Unlike the increasing trend in the overall surface resistivity, the fact that these ratios have been more or

less constant so far is rather reassuring, as it indicates that non-uniformity does not increase with time. Finally, in the bottom panel,it shows the humidity and temperature at the time of resistivity measurement. Initially, the temperature and humidity from the local weather casting ('external' measurements, in black) could only be taken, and then, for the last six months, the temperature and humidity during the resistivity measurements themselves were able to be measured using an Arduino-based sensor ('internal' measurements, in blue).

The new RPCs were assembled in beginning of the year 2022, so the resistivity data are only available upto December 2021.

5.4. Resistive plate version 3.0

Due to the cost and difficulty of accessing a serigraphy printer, the next set of resistive plates developed in the CP3 lab. Both the serigraphy technique and the hand-painted technique used in the initial prototype provided inspiration for the production process.

The goal is to finish production domestically. Glass plates of various thicknesses and surface resistivity ranges can be tested. The entire production process is explained in this section.

5.4.1. Instruments and Materials

We are using few different instrument and material in this process. A detailed description is provided below.

Glass Plates

The glass plates with three different thicknesses were bought from "VERRE INDUSTRIE" with a size of 20 cm × 20 cm and different thicknesses of 0.7 mm, 1.1 mm and 2 mm.

Resistive paint

There are 2 different components for the resistive paint:

- Conductive ink - LOCTITE Electrodag 6017SS
- Non conductive ink - LOCTITE Electrodag PM 404

The mixing of these 2 components in different mass ratios will allow to obtain certain resistive values.

$$r_c = \frac{m_r}{m_r + m_c} \tag{5.12.}$$

where:

- r_c - mass ratio
- m_c - mass of conductive ink
- m_r - mass of non-conductive ink

The reference values for different compositions are given by the manufactures, see figure 5.8.

Electrodag 6017SS (% by weight)	Electrodag PM-404 (% by weight)	@ 25µm dry coating thickness
100	0	35
90	10	50
80	20	70
70	30	105
60	40	170
50	50	290
40	60	675
30	70	2160
25	75	4500
20	80	35,000
10	90	> 1e9

Figure 5.8. | Blending ratios of LOCTITE EDAG PM 404 E&C and EDAG 6017SS, Dried 5 minutes @ 120 ° C, Ω / □ [114].

These two components are specially designed for the screen print method, so we have to adapt the composition for painting with a hand roller. The idea is to make plates with 500 KΩ / □, surface resistivity. So with the data in the Figure5.8, the r_c value we expected is less than 0.2, and we decide to test different values and also different techniques for painting.

Thinner

2-butoxy ethyl acetate (butylglycol acetate) is used as the thinner for the two components.

Mixer

One of the most important steps in the procedure is the mixing of the two components (and thinner, if required). Therefore, we choose to combine the two components using a vacuum mixer called the SmartMix X2, which is commonly used in the dental sector. The specialty of a vacuum mixer is that it generates a vacuum in the container while mixing, preventing the formation of air bubbles during mixing, which results in paint that is homogeneous. There are different containers for this machine with different volumes from 100 ml to 1 litre.

This machine is programmable for few parameters.

- Name - P02
- Mixing time - 5 minutes
- Mixing speed - 350 rpm

- Pre-mixing time - 20 seconds
- Pre-mixing speed - 150 rpm
- Pre-vacuum - 10 seconds

The machine can be programmed for 10 different presets, we set the mixing time from 10 seconds to 5 minutes. The speed of the mixing blade can be adjusted from 150 rpm to 550 rpm. The function of pre-mixing is to mix before fast mixing at a lower RPM. Pre-vacuuming creates a constant vacuum before the mixing process.

Oven for curing

The lab oven, UF750plus, was obtained for the "cooking" process of the glass plates after painting. This oven could be controlled over a computer or remotely via the internet and monitor the temperature in real time with an interface connected via the internet. The temperature deviation is less 2% for 120 ° C and there is an integrated fan to circulate the temperature inside the oven so the glass plates will cook evenly.

5.4.2. Painting Procedure

The painting procedure is done in few steps.

Step 1: Cleaning glass plates.

The glass plate is cleaned with Ethanol and dried with micro-fiber cloth.

Step 2: Making the resistive paint.

The scale was set to zero after the mixing container placed on it so that we can measure the precise amount of paint. We used a syringe to add the two halves of each paint ingredient. Before pouring the paint into the plastic containers, they were thoroughly agitated.

The cover with mixing blade was placed in the beaker after precisely measuring the masses of both components, and the blade was then fastened to the mixer. Using the preset p02 in SmartMix X2 (mentioned in section: 5.4.1), components were blended.

Step 3: Painting

After the completion of the mixing process, the beaker was removed from the SmartMix X2 and left for 15 minutes to settle before the weight of the empty syringe was measured. The mixture was then extracted with the syringe, and the weight was noted.Following that, as seen in the figure 5.10(a), the paint was poured on the glass plate. The paint is applied on the glass plate uniformly using the roller until there are no more holes in it. After painting, the glass plate's weight was measured and it was then baked for five minutes at 120°C.

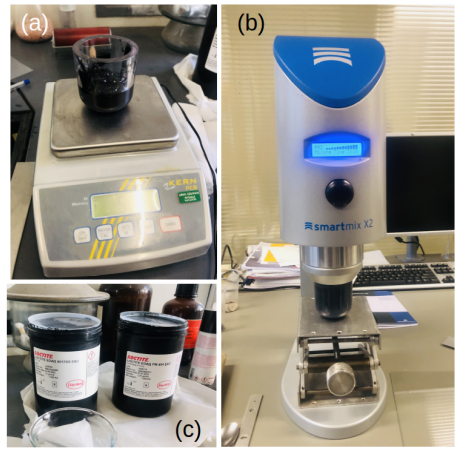

Figure 5.9. | (a) Measuring the wights of the component. (b)SmartMiX X2 mixer while operating. (c) Two components of the resistive paint.

Naming the resistive plates

The resistive plates should be carefully labelled for later identification and testing after being cooked. Four key elements were written on the plate, as seen in the figure 5.12.left). The plate's name or identification number can be found in the bottom left corner. The resistive mixture's composition is then recorded. There, the first number indicates the proportion of PM404, and the second number indicates the percentage of 6017SS's composition. The following value indicates the paint coverage on the plate as determined by the measurements made before and after painting. When measuring resistivity, the final dot represents the ninth position.

Calibration of mass ratio

The calibration of the mass ratio 5.12 for surface resistance of two components were done after the resistivity was measure for different compositions. The plot in Figure 5.13 shows the calibration curve of the mass ratio (r_c) 5.12. Note that the values in horizontal axis is (1 - r_c).

After the calibration, we produced resistive plates with $\sim$ 500 kΩ/ $\square$ and placed in a controlled environment for study the surface resistivity variation with time.

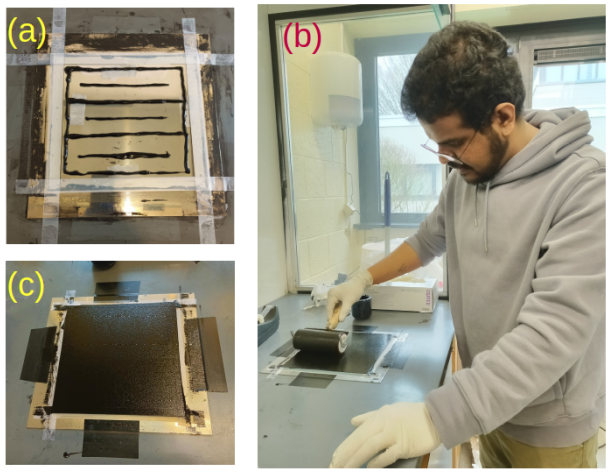

Figure 5.10. | (a) Fixed glass plate with poured paint. (b) painting the plate with the hand roller. (c) Painted plate before cooking.

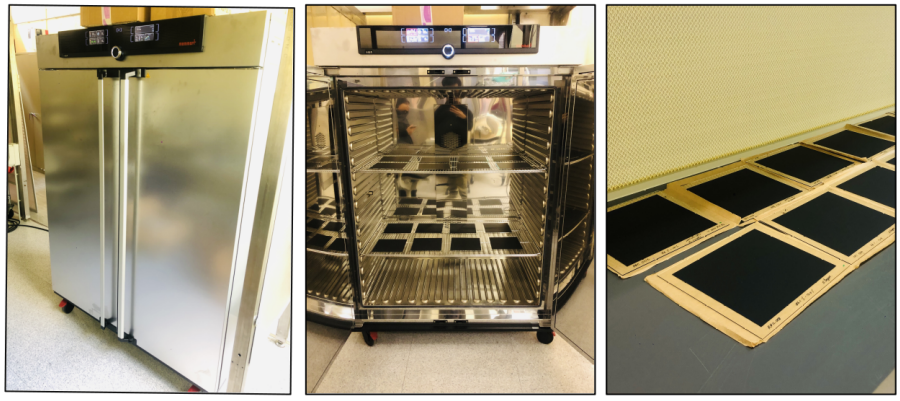

Figure 5.11. | UF750plus lab oven (left). Painted glass plates placed in the oven for curing (middle). The cured plates stored in a white room after measuring the resistivity (right).

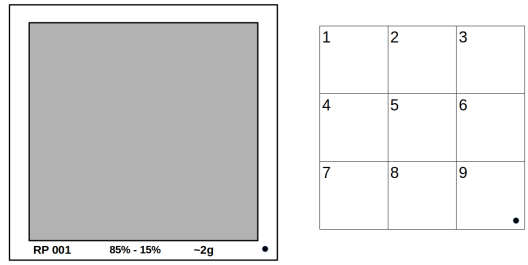

Figure 5.12. | Sketch of glass plates with labeling (left). Nine positions used to measure the resistivity of the paint (right).

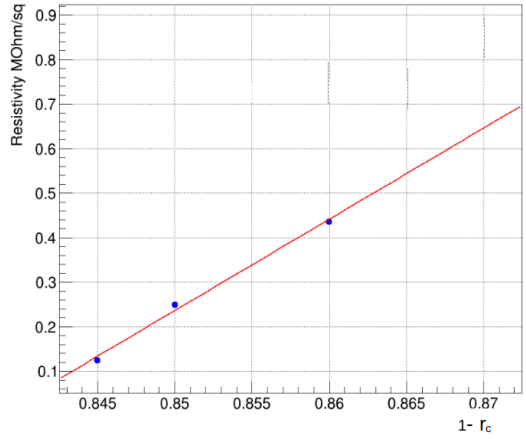

Figure 5.13. | Surface resistance as a function of 1 - r_c. The blue points denote experimental data points and red line is the linear fit. With equation of $R = 20.5\ .(1 - r_c)\ - 17.2$. This graph is used to determine the quantity of the conductive component needed to achieve a specific desired resistivity.

Chapter 6.
Readout boards

There are a few different signal readout boards that have been used in the muoscope project so far. The pitch and width of the all readout boards are 1 cm and 0.9 cm, giving a gap of 0.1 cm between two consecutive strips. And each board consists of 16 strips due to the limitation of readout channels in the DAQ system. Because the current DAQ only have 64 inputs and we need minimum 4 RPC for tracking a path of a muon. They were named in the chronological order of the production. The key factors for using each readout board and their differences will be covered in this chapter.

6.1. Readout version 1.0

This is the readout board used in first prototype of the Muoscope. The detailed description about this readout board is included in the section 3.1.4. The absence of a protective coating caused the copper strips to deteriorate over time (See figure 6.1). And after opening the chamber, it was clearly visible that we needed new readout board.

Figure 6.1. Readout board (V1.0) from with a degraded copper strips.

6.2. Readout version 2.0

The next readout board, which named as version 2.0 is a handmade readout board. There were few doubts regarding the RPC readout board's signal transmitting lines and connector.

6.2.1. Production

The next readout board was made with the same dimensions as the readout version 1.0. The printed circuit in version 1.0 is reused. So, the drilling holes for fix the resistive plates is not needed. For the readout strip, adhesive copper tapes with 9mm width is used. The gap between two strips were kept at 1mm in order to get a 1 cm pitch. Following are the major steps of production:

Step 1

There were few spared readout boards from the first muoscope prototype. They were already damaged as in Figure 6.1. The first step was to remove all the copper tracks and 34 pin male connector. The connector was removed by desoldering all the pins using a soldering iron and desoldering pump. Then all the copper tracks were removed using a sharp blade. Then all the PCB was cleaned.

Step 2

The next step was to mark the tracks on the plate so the adhesive copper tape could be aligned properly. After marking all the tracks on the plate, The copper tapes were placed on the marked tracks. and copper tape was place on the back side of the PCB perpendicular to the tracks in one side of the PCB in order to use as common ground connection of the readout strips.

Step 3

In the next step a 34 pin female connector (17 pairs of signal and ground) was made with flat cable with a length of 10 cm. Then signal/ground pair was soldered to each strip while the both cable from 9th pin was soldered to the ground (It's the ground pin in CMS FEB).

Step 4

In the final stage, all the connections were checked using multi-meter to ensure soldering were properly done and to make sure no any grounding errors.

The few steps of the production process is shown in the figure 6.2.

6.3. Readout version 2.1

Version 2.0 of the readout board has been upgraded to version 2.1. We discovered that the impedance mismatch between RPC, the signal transmission line (a 34-pin flat cable) from RPC to DAQ, and the internal impedance of the

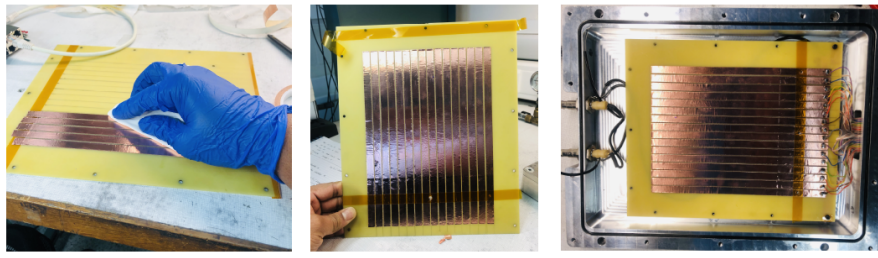

Figure 6.2. | Placing copper adhesive tapes on the marked tracks on the cleaned PCB (left). The 9 mm wide readout strips with 1 mm gap after removing excess tapes from top and bottom of the PCB (middle). Final readout board with soldered flat cable (right).

DAQ FEE caused the reflection of the signal, which resulted in noisy data reads from V2.0 in DAQ.

6.3.1. Simulation study of reflection

A simulation study was done with LTspice simulation software to understand about the signal reflection. LTspice is a strong, quick, and free SPICE simulator software, schematic capture, and waveform viewer that includes upgrades and models for enhancing analog circuit simulation. Its graphical schematic capture interface allows you to probe schematics and generate simulation results, which can be further investigated using the built-in waveform viewer [115]. The figure 6.3 shows the simulation setup of the LTspice used to investigate reflection.

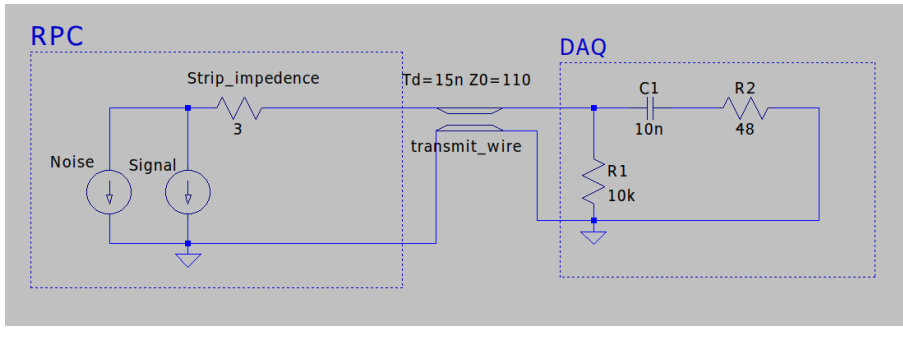

Figure 6.3. | The sketch of the RPC (with readout V2.0) and DAQ with components related to impedance. In the RPC side, The signal mimics the RPC signal and random noise was implemented on the top of the signal. The resistor name as "strip impedance" denotes the impedance of one readout strip. The transmit wire denote one pair of cables of flat cable and Td is transmission delay corresponds to the length of the wire (~ 5ns per 1m) and wire impedance is denoted by Z0, The values are from [116]. The input of CMS FEB are from [98], in the DAQ section.

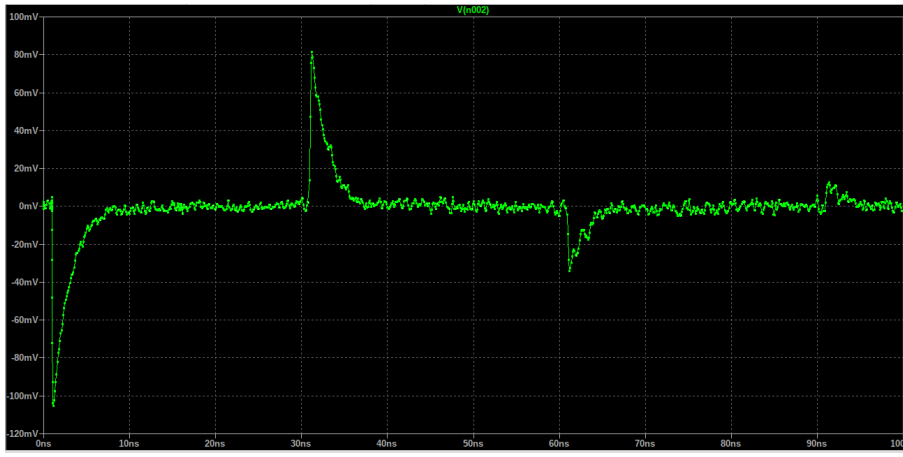

Figure 6.4. | Simulated signal with reflection on the RPC end.

In the figure 6.4, the horizontal axis is the time, and the vertical axis denotes the voltage. The first peak on the negative side of the voltage axis is the actual signal, and the other peaks at 30 ns and 60 ns are from reflections. These reflections didn't cause noise in the DAQ system.

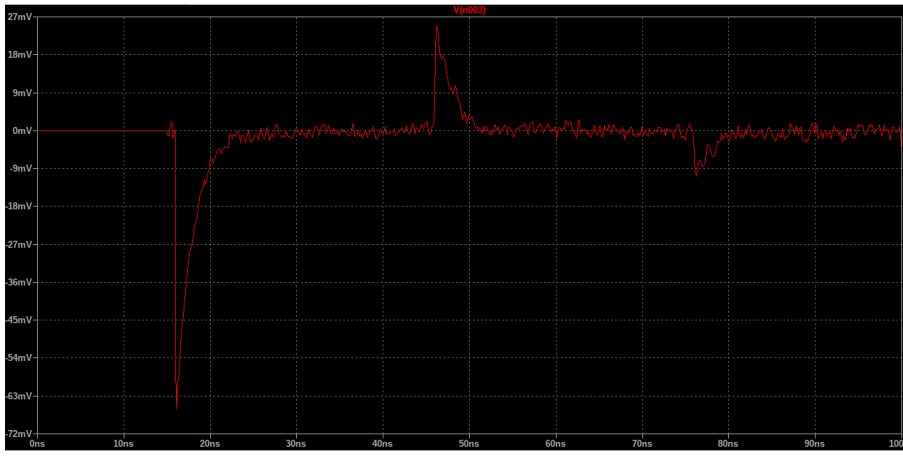

Figure 6.5. | Simulated signal with reflection on the DAQ end.

In the figure 6.5, the horizontal axis is the time, and the vertical axis denotes the voltage. The first peak on the negative side of the voltage axis is the actual input signal, and it appears 15 ns after the signal is produced from the RPC (which corresponds to the transmission delay of the wire). Other peaks at 45 ns and 75 ns are from reflections. These reflected signals can be detected by DAQ electronics and cause false counts. This reflection appeared in the system due to mismatching of the impedance of the system and mainly the transmission

line [117]. This can be minimized by terminating with proper resistors. 100 Ω resistor is used to terminate the RPC end of the wire as in the simulation sketch in figure 6.6.

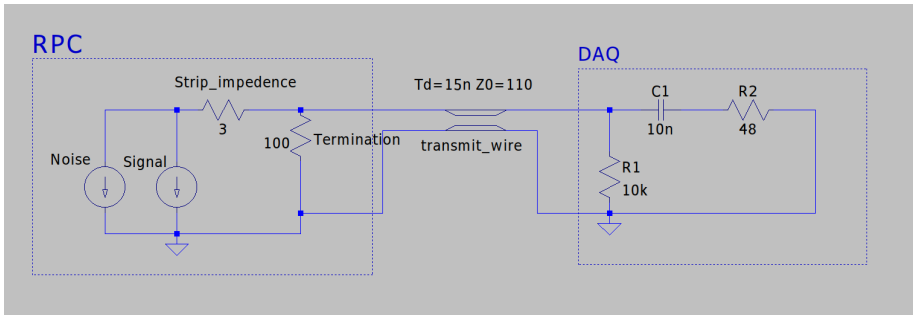

Figure 6.6. | The simulation sketch with 100 Ω resistor between signal and ground wires of the RPC strip. The rest of the setup is same as in figure 6.3.

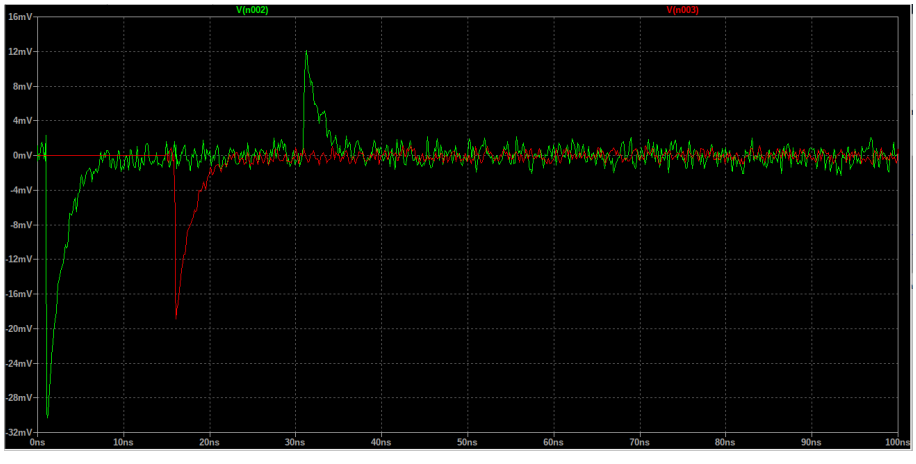

Figure 6.7. | Simulated signal with both RPC end (Green signal) and DAQ end (Red signal).

As seen in the figure 6.7, after terminating the readout strip with a 100 Ω resistor, the signal reflection at the DAQ end is eliminated. The reason for using a 100 Ω resistor is that it is a readily accessible resistor that is near to the transmission wire's impedance.

6.3.2. Production process

The readout version 2.1 was simply made by soldering a 100 Ω resistor between the readout strip and the ground of the readout version 2.0. The connector end of the readout version 2.1 is shown in the figure 6.8.

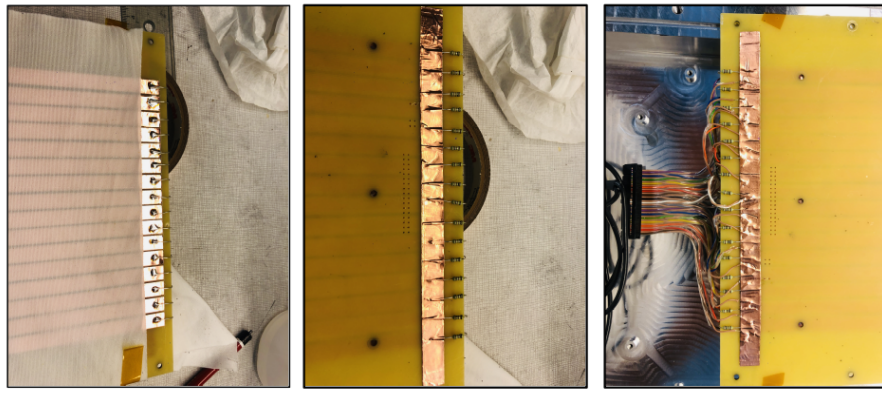

Figure 6.8. The resistors soldered on signal end and ground end of the strip (Left and center figures, respectively). Readout board with 34 pin connector (right).

The performance studies of the readout board will be discussed in the performance study section of the thesis.

6.4. Readout version 3.0

The readout version 3.0 was designed in UCLouvain and produced in a external company, who provides the service for printed circuit boards. This board was made to test the RPC with Nuclear instrumentation modules (NIM) without using the DAQ of muoscope.

The new readout board consists of coaxial cable directly connected to the readout strips (see figure 6.9.(a)). A new "piece" is made to seal the chamber while the 16 coaxial cables come out of the aluminum chamber. Then this cable can be mounted to a board with 16 NIM outputs 6.9.(b). The coaxial cable is small, so we cannot connect that cable directly to the standard 50 Ω NIM connectors. That's the reason for connecting coaxial cables to external boards with standard NIM female connectors.

The RPC chamber is filled with the typical gas mixture; R134a Freon (95.2%), Isobutane (4.5%) and SF_6 (0.3%) and the pressure inside the chambers keep bit higher than 1 atm (~ 0.1 atm). The RPC chamber is sandwiched between two external scintillators + PMT, as shown in figure 6.10. The chamber was powered by the DAQ's integrated high-voltage power supply, while each PMT is powered by a 15 V power supply through voltage regulators. The NIM connector board is taped to the table for the moment. The output was fed into the oscilloscope to see the raw PRC signal. The signal is shown in the figure 6.11. Few studies were done with this setup in order to understand the behavior of the RPC and to see the noise in the lab.

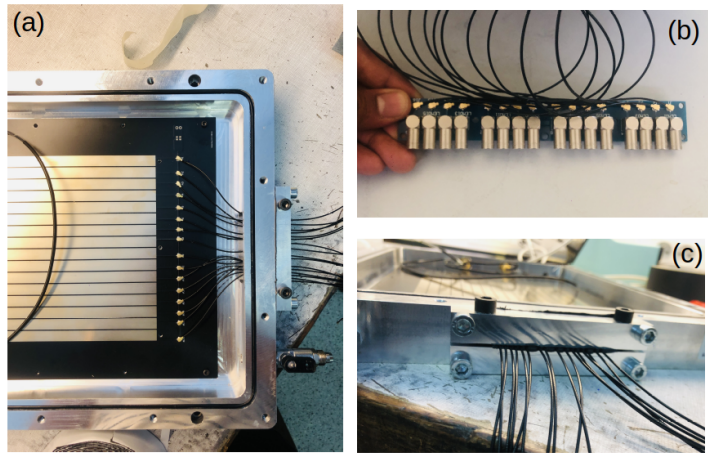

Figure 6.9. | a).Readout board inside the Chamber (b).Board with 50 Ω NIM standard female connectors. (c) New sealing "piece" for RPC.

Figure 6.10. | RPC setup with scintillators.

6.4.1. Cross talk study

The unwanted propagation of signal in neighboring strip due a signal can be simply describes as the cross-talk of a signal. This often happens in RPCs due to the fact that the distance between two consecutive strips are small (in order

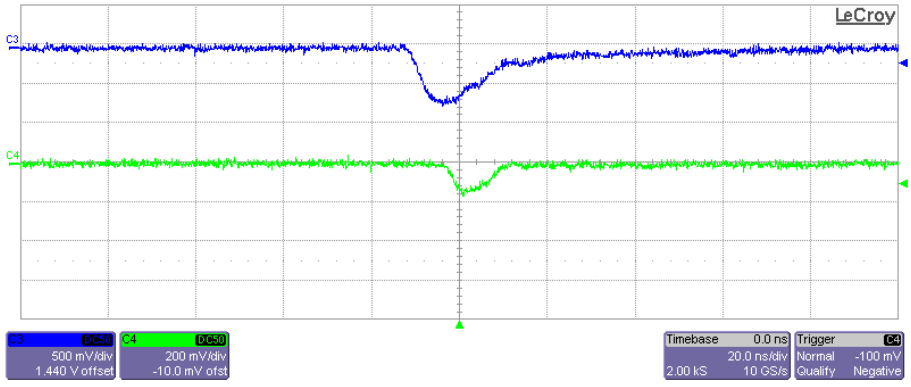

Figure 6.11. | Signal from the PRC readout strip (Blue line is the trigger scintillator and Green line is the RPC signal). The RPC signal was faster than the scintillator signal. A delay of 34 ns was introduced to the system using 3 LEMO cables (10 ns + 16 ns + 8 ns). The trigger was setup to qualify the mode on the oscilloscope.

of mm). Few studies done on cross-talk study can be found in refs. [118,119].

The cross-talk between the adjoining strips is discussed in this section. In figure 6.12 the pink signal denotes the signal that the green signal, or cross talk, caused in the neighbouring strip as opposed to the expected avalanche signal from the RPC. The signal due to cross talk is always with phase difference of 180 °.

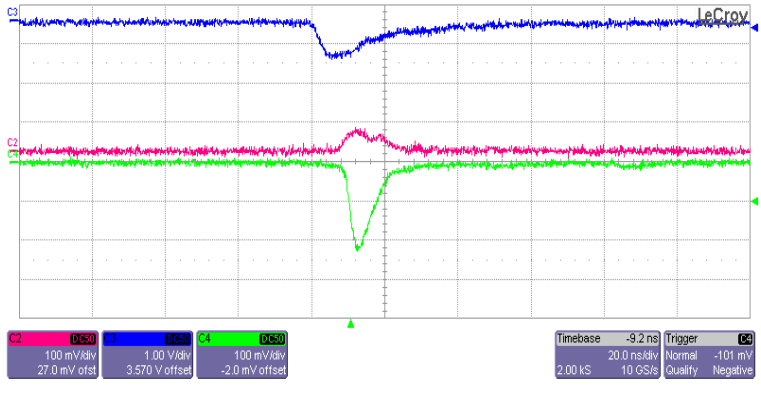

Figure 6.12. | Signal from a single strip of the RPC for HV = 2600, blue line is the trigger scintillator signal; the green is from the RPC; and the red is the cross-talk of the next strip in the RPC lab.

The signal strip was fixed and cross talk signal was measured for different strip from closest strip to furthest strip and signal to cross-talk ratio was calculated. See figure 6.13.

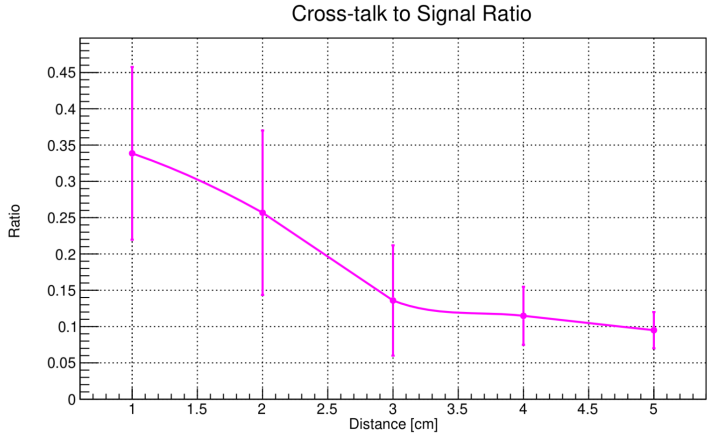

Figure 6.13. Cross-talk to signal ratio in relation to the location of the individual readout strip. Since the triggered strip is not clearly visible beyond 5 cm, the data was only obtained from the first 5 cm of the strip.

A large cross talk between strips was observed, as seen in Figure 6.13; in particular, neighboring strips have a cross talk of 35%. And it decrease with the distance.

6.5. Readout version 4.0

The readout version 4.0 was produced by an external company for printed circuit boards after being developed at UCLouvain. After Version 2.1 produced findings that were deemed acceptable, this board was created. A 34-pin male connector and locations for soldering appropriate resistors are included in the design. The signal is transferred to the copper strip with 1mm copper tracks from the RPC's 16cm $\times$ 16 cm active area. 100 Ω resistors were soldered as in the readout version 2.1 in order to avoid the reflections. The high quality copper was used in this strips. See figure 6.14. The copper tracks from strips to connector were placed with maximum distance possible to get minimum cross-talk between tracks.

Two RPC chambers were assembled with readout board version 4.0 and tested. Results are shown in Performance study section.

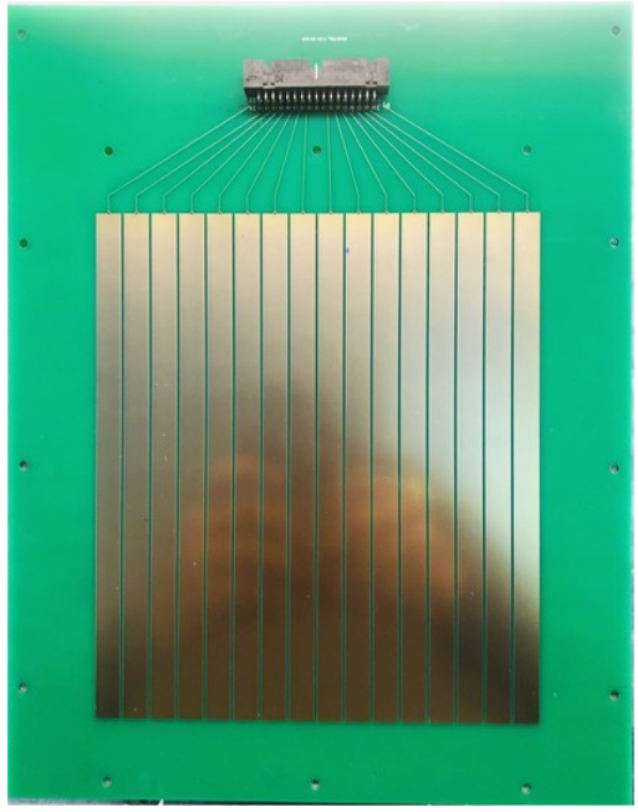

Figure 6.14. | Printed readout board with better quality copper and connection for flat cable (compatible with DAQ) with 100 Ω termination.

7. Chapter
Noise study in RPC lab

There was a background noise which affect the detector performance in the RPC lab. This chapter describes the study of noise and some discoveries about the noise.

7.1. Baseline noise of RPC

There was a baseline noise in the RPC. It is common to have noise, but the base line has a high amplitude level. Which makes the signal-to-noise ratio low, and DAQ will read this noise as a signal. The Figure 7.1 shows the baseline noise in the RPC inside the RPC lab at UCLouvain. As seen in Figure 7.1, the amplitude

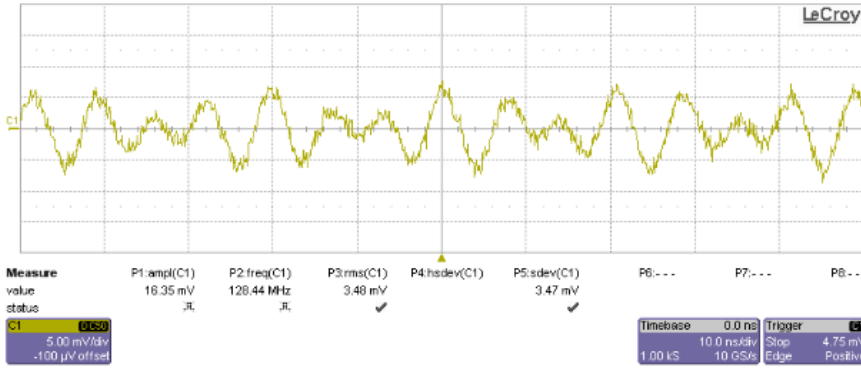

Figure 7.1. | Base-line noise oscillogram when connected to the RPC readout strip. There is no signal from the RPC since it is powered at a high voltage of 4 kV, which is lower than its operating voltage. In the oscillogram horizontal axis denotes the time axis and vertical line denotes the voltage.

(peak to peak) of the noise is around 20 mV, and the baseline in Figure 7.2 shows that the typical baseline should be less than 5 mV (peak to peak). So the RPC readouts catch noise from somewhere. The first assumption was that it was generated by the high-voltage power supply, so a test was done to verify if there was any relation between the high-voltage power supply and the noise.

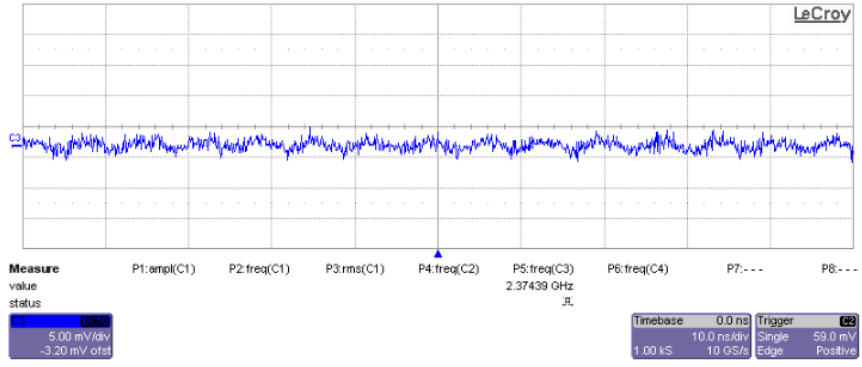

Figure 7.2. | Base-line oscillogram when RPC is not connected to the oscilloscope.

7.2. Baseline noise and high voltage supply

Since the mean value of the amplitude of the noise signal is close to zero, the standard deviation of the signal amplitude was calculated for different high voltage values. To calculate the standard deviation (sigma), 500 different noise signal were recorded from the oscilloscope and plotted. The standard deviation of amplitude of noise signal for 800 V is shown in the figure 7.3.

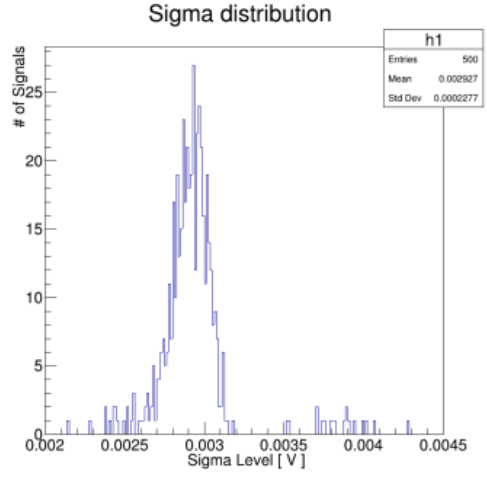

Figure 7.3. | The standard deviation of noise amplitude. The high voltage supplied for RPC was 800 V.

The mean value of sigma of noise was measured for various high voltages and plotted against, high voltage value in order to understand the behaviour of noise as a function the high voltage.

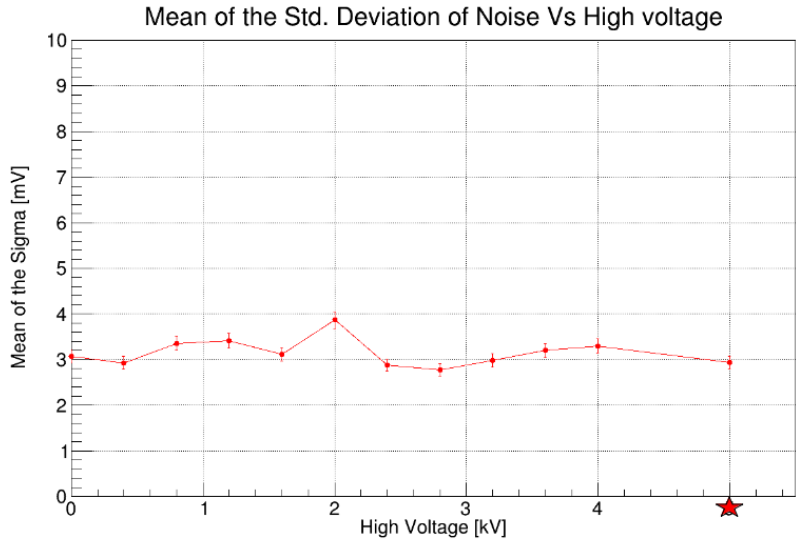

Figure 7.4. Mean of standard deviation with respect to high voltage of the RPC, note that data point with (*) symbol is the Mean of standard deviation of noise amplitude when high voltage supply disconnected from the RPC.

In the plot in figure 7.4, it is clearly visible that the noise doesn't change with the supplied voltage to the RPC, because the curve only deviates within small range of values. So it conclude that readout strip is sensitive to some background independent of the RPC.

7.3. Frequency of the noise

As the source of the noise was external, the first step was to determine what type of noise it was. As seen in figure 7.1, it has a pattern, so the frequency of the signal can be calculated. The frequency distribution of the noise is shown in the figure 7.5.

The mean value of the frequency was 141 MHz. This belongs to the frequency range of the radio signal. It concludes that the experiment is affected by a radio signal and we hypothesise that copper strips or aluminum box act as an antenna for this signal.

7.4. Shielding the chamber

The simplest method to eliminate this electromagnetic interference was to construct a Faraday cage around the RPC. In the first attempt, one chamber was covered with bubble wrap (See figure 7.6(left)) and then covered with aluminium foil (kitchen-use foils with a thickness of 16 micrometres). At the

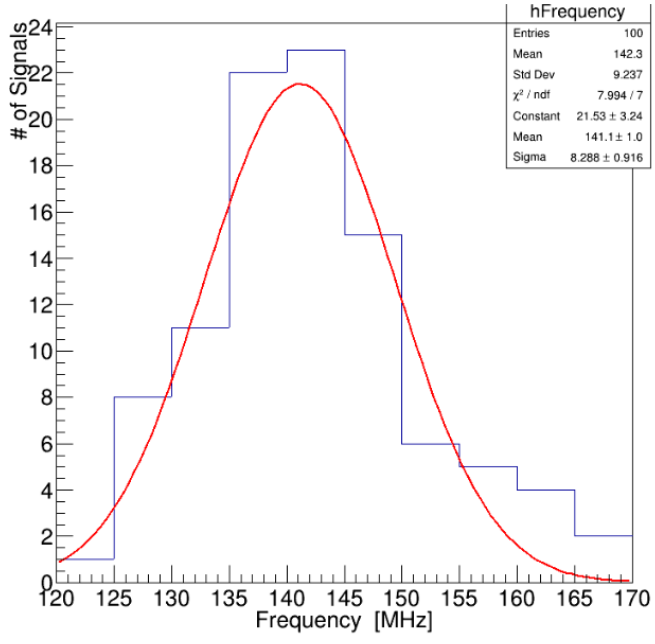

Figure 7.5. The frequency distribution of the noise, calculated from the signal pattern of the oscilloscope.

same time, the signal from this configuration and the signal from the uncovered RPC were analysed. However, there was no impact on the noise level.

The RPC was inserted inside a cardboard box and then wrapped in aluminium foil as shown in the figure 7.6(right), for the next attempt. The signal from this configuration and the signal from the uncovered RPC were analysed simultaneously.

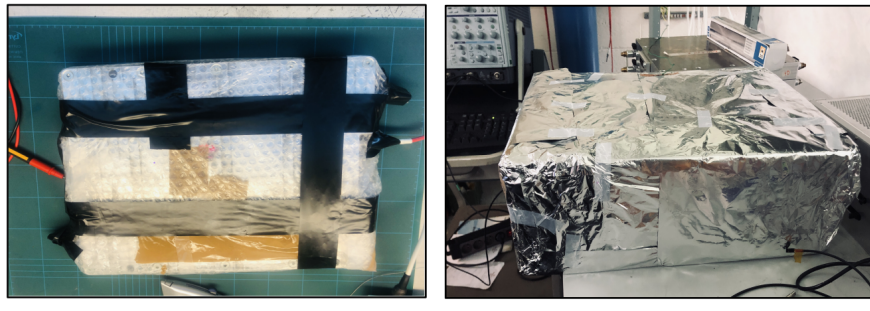

Figure 7.6. The wrapped RPC with bubble wrap before covering it with Al foil (left) . The cardboard box covered with Al foil after placing RPC inside the box.

Three tests were done with Faraday cage's ground connection and Noise ratio was calculated with respect to the noise of uncovered RPC.

$$A_r = \frac{A_f}{A_{uc}} \tag{7.1.}$$

Where,
A_r : Noise ratio
A_f : Peak-to-peak amplitude of signal from RPC covered with Faraday cage
A_{uc} : Peak-to-peak amplitude of signal from uncovered RPC

The figures 7.7, 7.8, 7.9 depict the two signals: Ch2 (pink) is the signal from the exposed RPC, while Ch4 (green) is the signal from the RPC inside the Faraday cage for various grounding experiments.

7.4.1. Baseline noise with the Faraday cage without connecting to ground

In this test, the Faraday cage was not grounded, and A_r 7.1 was calculated from the amplitudes of two channels (See figure 7.7).

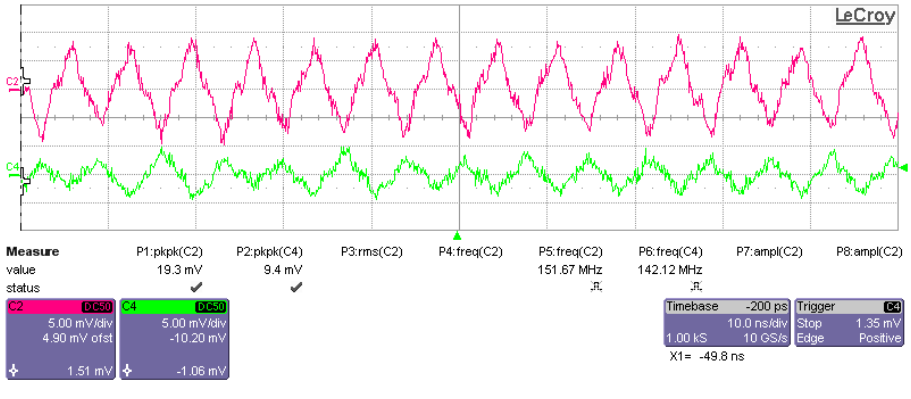

Figure 7.7. | Two signals from Ch2 and Ch4 when Faraday cage without connecting to ground.

From equation 7.1, noise ratio:

$$A_r = 0.49$$

7.4.2. Baseline noise with the Faraday cage connected to the electric ground

In this test, the Faraday cage was connected to the electric ground of the lab. And A_r was calculated from the amplitudes of two channels (See figure 7.8).

From equation 7.1, noise ratio:

$$A_r = 0.76$$

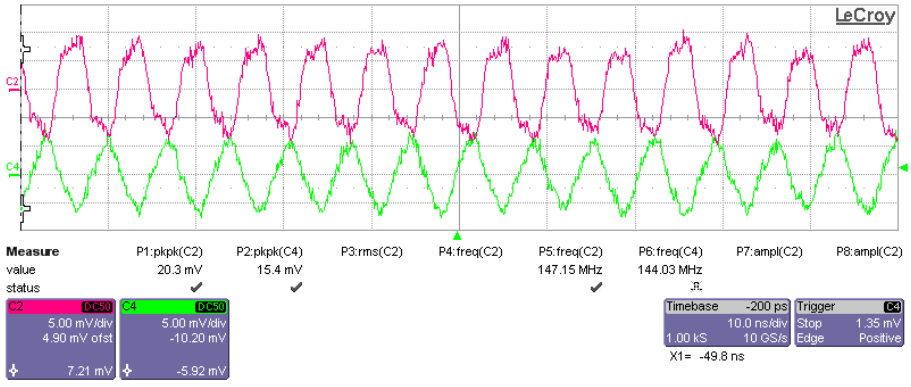

Figure 7.8. | Two signals from Ch2 and Ch4 when Faraday cage is connected to the electric ground of the lab.

7.4.3. Baseline noise with the Faraday cage connected to the real ground

In this test, the Faraday cage was connected to the floor of the lab using a copper tape and wire. And A_r was calculated from the amplitudes of two channels (See figure 7.9).

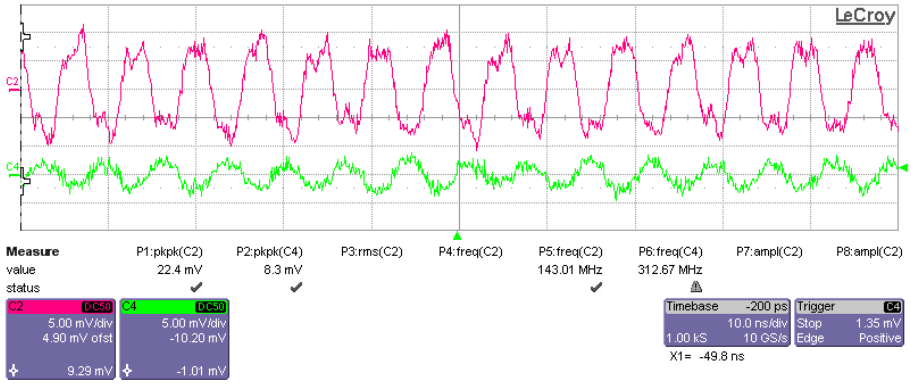

Figure 7.9. | Two signals from Ch2 and Ch4 when Faraday cage connected to the real ground.

From equation 7.1, noise ratio:

$$A_r = 0.37$$

From the noise ratio value, we can get a understanding about effect of the Faraday cage. When Faraday cage is not grounded, it reduce the signal amplitude by ~ 50% while the grounding the Faraday cage through electric ground reduce the amplitude by ~ 25%. And when Faraday cage is grounded

through floor of the lab, it reduces the amplitude of the noise signal by ~ 65%. This gives an important information about the electric ground that it's not properly grounded.

The next step is to find the source of this ~ 141 MHz signal affecting the experiment.

7.5. Source of VHF radio frequency noise

In order to find the noise source we borrowed ANRITSU MS2713E spectrum analyzer [120] from the electronic engineering department of UCLouvain. This is a portable device with 3-D antenna, and it will output the power of the signal as a function of the frequency of the signal.

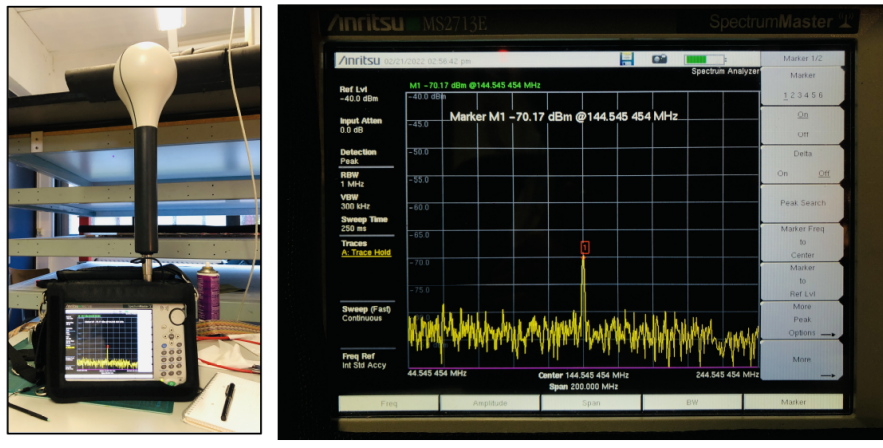

Figure 7.10. | ANRITSU MS2713E spectrum analyzer [120] (left). The screenshot of the screen of spectrum analyzer in the RPC lab, there is signal of frequency 144.5 MHz signal in the lab (right).

Figure 7.10(left), shows the spectrum analyzer we used to measure the noise in the RPC lab and to locate the noise source. The spectrum analyzer connected to the 3-D antenna (the bulb like antenna) to measure the electromagnetic spectrum. From the Spectrum analyzer, we measured the exact frequency of the noise, which is 144.54 MHz with a signal strength of -70.1 dBm.

We measured the signal strength of this 144.5 MHz signal through out the whole ground floor of the "Marc de Hemptinne" building and in Tower E in every level, and found that this specific signal is not from a source inside the building.

And later we found that, a new beacon with 144.4 MHz frequency was installed in the rooftop of tower E, by Royal Belgian amateur radio association since late 2019 [121]. We contacted the project co-coordinator of UCLouvain and switched off the transmitter of 144.4 MHz signal.

8. Chapter
Performance studies

8.1. Data Acquisition system

This section describes a few performance tests conducted using the muoscope DAQ. These tests' primary objective was to validate the DAQ's proper functionality.

8.1.1. Channel testing

The objective of this test to check the functionality of the 64 input channels of the CMS FEBs integrated in the DAQ. For this we feed pulse using a signal generator TPG 110 10 MHz pulse generator [122] to the each channel of the DAQ. Note that there are 4 separate 34-pin male connectors in the DAQ named as **A, B, C, D**, each of the have 16 channels. Setup is shown in figure 8.1.

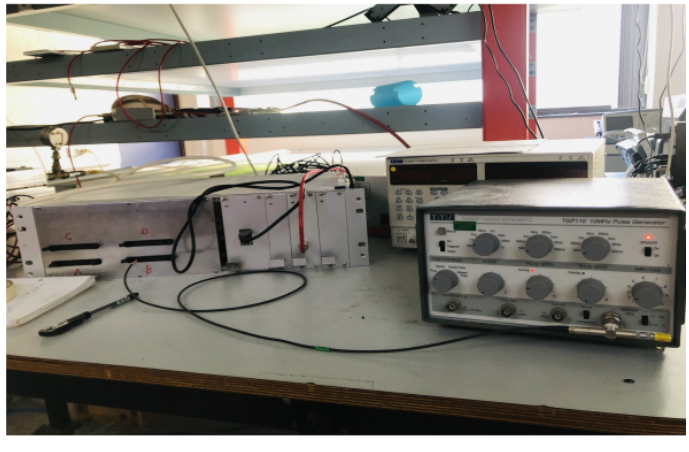

Figure 8.1. | The experimental setup of the channel test, DAQ is in the left side and pulse generator in the right side, and signal was send via coaxial cable.

Features of the test signal :

- Mode - Pulse
- Amplitude - 150 mV
- Width - 50 ns
- Frequency - 1 KHz
- Polarity - positive (+)

In the DAQ setting, the threshold of each channel was set to 60, and the number of coincidences was set to 1 from the GUI of the muoscope. The data was collected for 30 seconds for each channel. The number of counts from each channel was plotted for each of the 16 channels. The results are shown in figure 8.2.

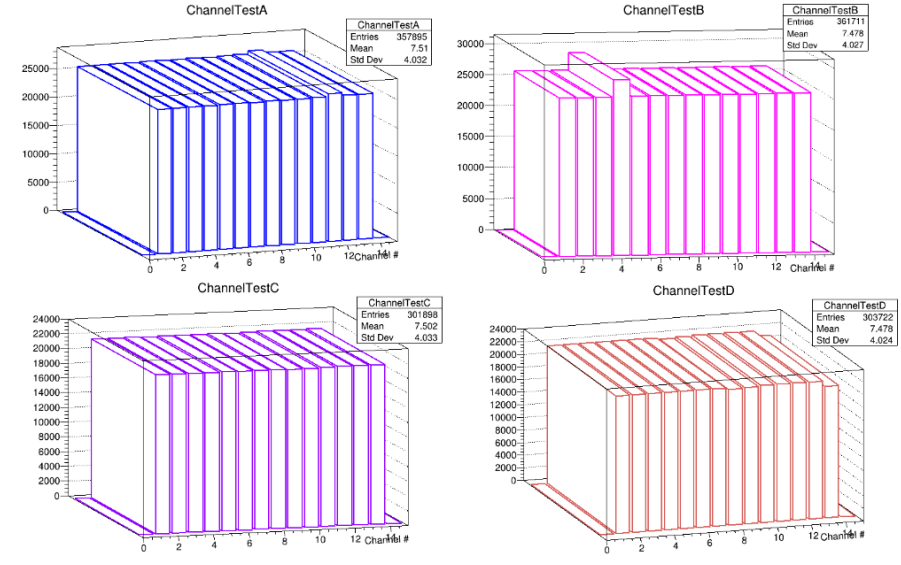

Figure 8.2. The number of counts for each channel in CMS FEB for connections A, B, C, and D are shown in four graphs. The three-dimensional visualisation of the plots makes it easy to distinguish between the channels. The 0th and 15th channels of each A, B, C, and D module were not included in the plots since the data gathering program excluded two corner channels because the borders of the RPCs were noisy.

As seen the plots in figure 8.2 clearly, all channels are operational, but the fifth channel in sector B is more active than the others, and the fifteenth channel in sector D is less active than the others in that sector. Due to the fact that we could only control a handful of parameters in the CMS FEB, this behaviour cannot be adequately explained. However, the front-end board performs as anticipated overall. Since it worked well with a 1 KHz signal, it could also manage cosmic muon signals, whose frequency is much lower (about 1 muon per square centimetre per minute).

8.1.2. Minimal threshold of the DAQ

In the DAQ, one of the two parameters we could control in the CMS RPC front-end electronic module is the threshold of the discriminator in the readout

chip. As mentioned in Section 3.2.1, muoscope DAQ consists of two front-end modules that have eight readout chips. We can change the threshold of the discriminator of each chip using the control program of the DAQ or the graphical user interface (GUI) of the muoscope (see figure 8.3.

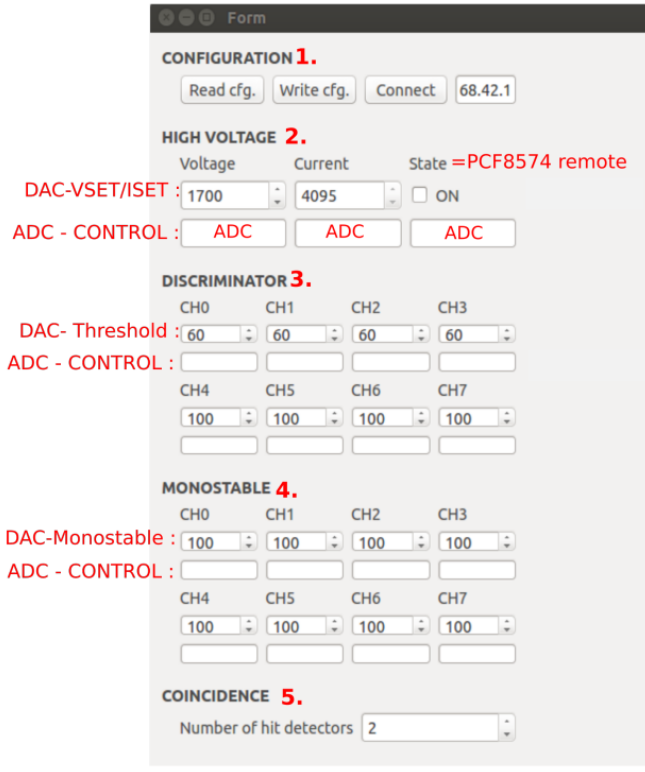

Figure 8.3. | High voltage, threshold and monostable interface.

But this threshold value doesn't have any units; it's a conversion value from digital to analog converter, and there is no way to know the conversation factor of this number for the actual input value of the discriminator in the readout chip. So all conclusions are based on experimental values when comparing thresholds. We are using the term DAQ threshold units for this since it was setup in the DAQ.

8.1.3. Configuration

The "Read cfg." and "Write cfg" commands are used to save the present configuration and read the old configuration that is already saved. The "Connect" button is crucial as it acts as a bridge between the computer and the CPU of

the detector (located in the rack). It permits access to the CPU, launches data acquisition, copies data to your computer using the scp command.

8.1.4. High voltage

The voltage box is used to set the high voltage value in the HV supply. The Values entered via this interface is DAC units. The conversion of the DAC value to voltage value can be done using the equation below. And we use term 'DAQ HV units' for the sake of identifying.

$$V_{out}[volt] = \frac{V_{in}[DAQ\ unit]}{4095} \times 10000 \tag{8.1.}$$

8.1.5. Coincidence

The amount of coincidence input depends on the number of detectors attached. This means that if the number of coincidences is four, for example, one hit on each detector will start the acquisition system. Also, we called this parameter as **online coincidence** and the coincidence calculation after analysing the data as **offline coincidences**. We did few threshold scan of the DAQ, to get understanding about the behaviour of the threshold.

8.1.6. DAQ counts without RPC connected

One of the tests we did with DAQ was to see how electronic noise affects the front-end module of the muoscope. A threshold scan was done with the following configurations:

- Flat cable for signal and HV cable was disconnected
- 2 online coincidences
- HV = 0
- Threshold from 0 to 200 with step size of 10

15 minutes of data were taken for each threshold value. According to the data, the electronic noise from the system affects only threshold values of 0, and for all other thresholds, the data counts were zero. We concluded that electronics function well.

8.1.7. DAQ behavior with cables

Although the electronics were working fine when the cables were connected to the DAQ, it caught the noise in the background. The plot in figure 8.5 shows the threshold scan for both cases with signal cable and without signal cable. With this noise, we cannot go below the threshold of 50 DAQ units.

The next section will discuss the high-voltage scans and threshold scans of the RPCs. Note that the below-mentioned tests are done with **positive high**

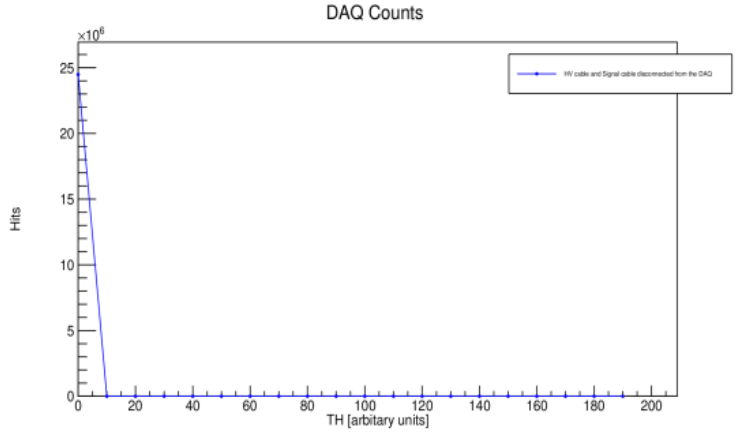

Figure 8.4. | DAQ counts without any connection, The counts observed here are pure electronic noise from the system.

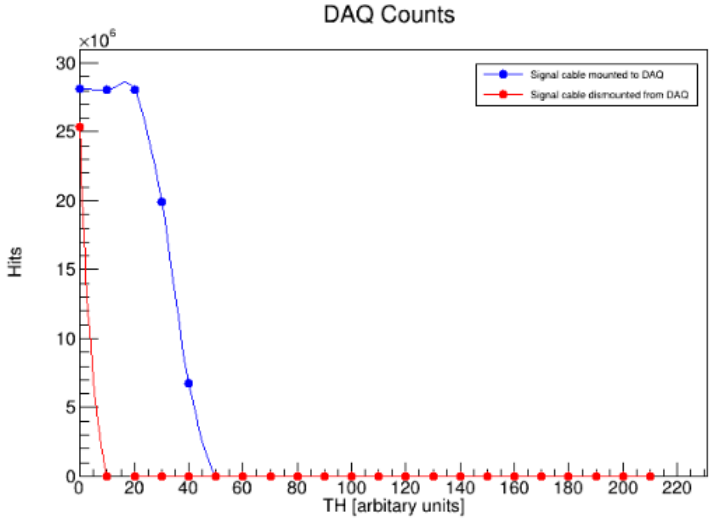

Figure 8.5. | Noise scan by signal cable: the blue line corresponds to the threshold scan when the signal cable is connected to the DAQ, and the red line corresponds to the threshold scan when the cable is not connected to the DAQ.

voltage supply, which gives the signals a **positive polarity** until we shift to the negative power supply. The CMS front end module is capable of reading signals from both polarities.

8.2. Self trigger mode

The DAQ was operated under the self-trigger mode, which only considers the hits on RPC layers depending on the online coincidences (see section 8.1.5) set in the GUI. As an example, consider the following scenario: When 4 RPCs are connected to the DAQ, if we enter value 1 in coincidences, the DAQ will start recording data when there is one strip fired (inducing a signal above the threshold of the discriminator in the FEB) in any of the chambers. It will record data for 64 strips. If we enter value 2 in coincidences, the DAQ will start recording data when there is one strip fired in at least two out of four chambers; it will record data for 64 strips.

8.2.1. High voltage Scan

In this test, we were trying to understand the behaviour of the RPC as a function of the high voltage provided to it. We have 4 RPC detectors, and they are named A, B, C, and D as the connection slots in the DAQ. The RPCs can be powered in two ways:

1. Built-in power supply in muoscope DAQ or 'internal power supply'
2. FuG-Series HCE 35-20000 High voltage supply [123] or 'external powers supply'

Figure 8.6. | fug HCE 35-20000 high voltage power supply [123], this can reach high voltage of 20 kV from 0 V.

Single hits in RPC

In this test, we were trying to understand the behaviour of the RPC as a function of the high voltage provided to it. We have 4 RPC detectors, and they are named A, B, C, and D as the connection slots in the DAQ. The RPCs is powered with internal power supply.

The total number of hit in the detector for 5 minutes is too high in the DAQ. The total number of muons passed by one detector (with the rate of 1 muon/cm^2 / min) should be around 1300, but it reaches up to the order of 10^6. This means

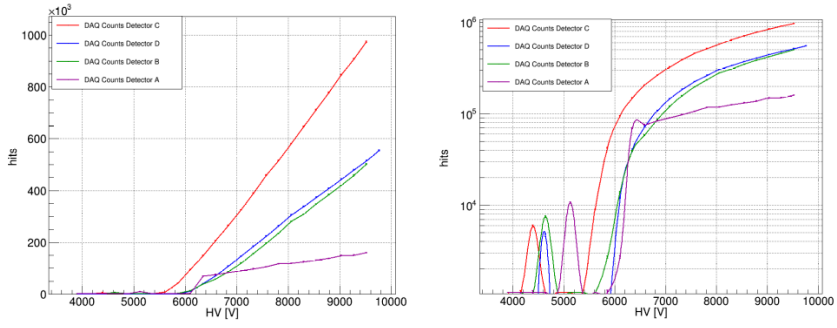

Figure 8.7. The total hits in each RPC as a function of High voltage supplies. The left figure shows the the hits in linear scale and right figure shows the hits in log scale for better understanding of the counts in low voltages.

the system is exposed to noise, which we didn't understand at the time of the test. We selected 115 as the threshold value to get rid of the noise induced in the signal cables from RPC to DAQ.

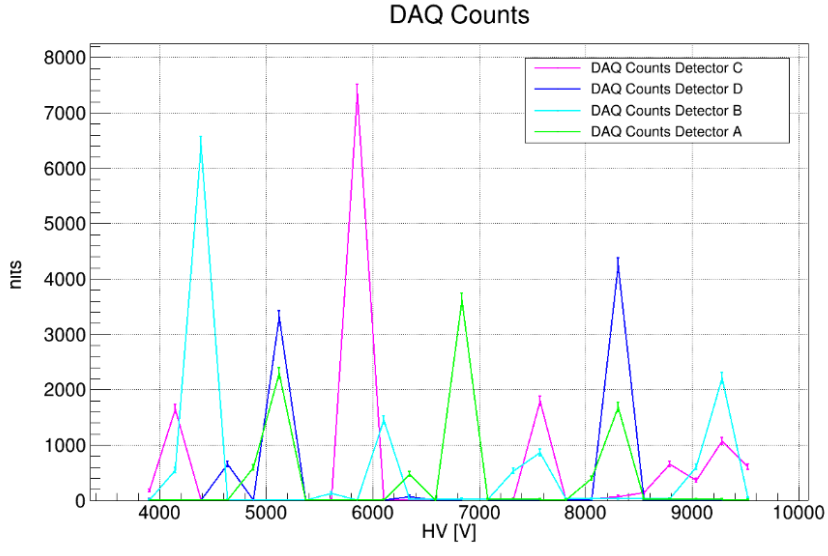

Figure 8.8. The total hits in each RPC as a function of High voltage supplies with 4 coincidences.

Coincidences in RPC

High-voltage scan was done with four online coincidences. In this test, 3 RPCs were powered by the 'external' power supply at a fixed voltage of 7 kV, and the

other RPC was powered by the "internal' power supply from ~ 4000 V to 9500 V with a step size of 244.2 V (we used the internal power supply, and this value corresponds to 100 DAQ units in HV). This scan for all four RPC detectors are shown in the figure 8.8.

With four online coincidences (see figure 8.8), the number of hits in the detector is reduced by an order of 10^3, but the peaks in every detector don't have an explanation except that the proper count is masked by noise induced in the readout strips. One of the major noise sources that we found was discussed in Chapter 7. Since we discovered the noise in the lab, we shifted the setup to the CMS clean room in CP3/UCLouvain with the permission of the CMS group.

We are interest of two major parameters.

Multiplicity - Multiplicity is the total number of strips fired in an event. This number is between 1 and 16 in our detectors. Offline analysis is used to get less than multiplicity 3 for clean data.

Occupancy - Occupancy can be described as how many times each strip was fired for the whole data set, which will give us an understanding of the behaviour of each strip.

8.2.2. Comparison between RPC lab and Clean room

The same study was done in the RPC lab and CMS clean room to look for better working conditions for the RPC. The three RPCs were used and stacked as in the figure 8.9. The online coincidences were set to three, and RPCs were powered by an internal power supply at -6.6 kV. The data were taken for 12 hours.

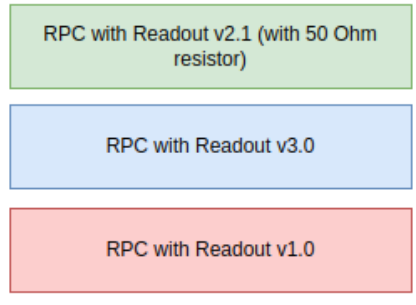

Figure 8.9. | Sketch of arrangement of RPCs with different readout boards.

The three RPCs behave differently from one another. The multiplicity of all chambers is greater than three, and chamber with readout v4.0 is the worst of them. This is probably due to impedance mismatching in the system. In the occupancy plot, it's clear that the corner strips are firing more than the middle

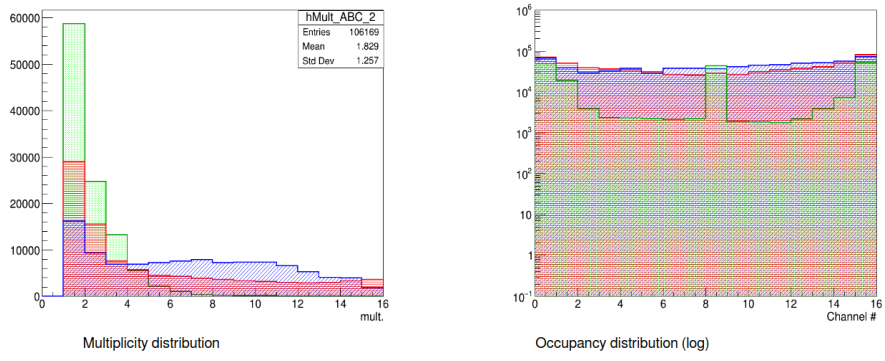

Figure 8.10. | Multiplicity and occupancy distributions of three different RPCs in the RPC lab. The green plot represents the readout version 2.1 (see section 6.3), but with 50Ω termination, the blue plot represents the RPC with readout board version 3.0 (see section 6.4) and red represents the chamber with the readout board Version 1.0 (See section 6.4)

strips, which is not acceptable, and we found that the 8th strip had a loose connection with the signal cable, which explains the highest counts, due to the noise caused by the loose connection.

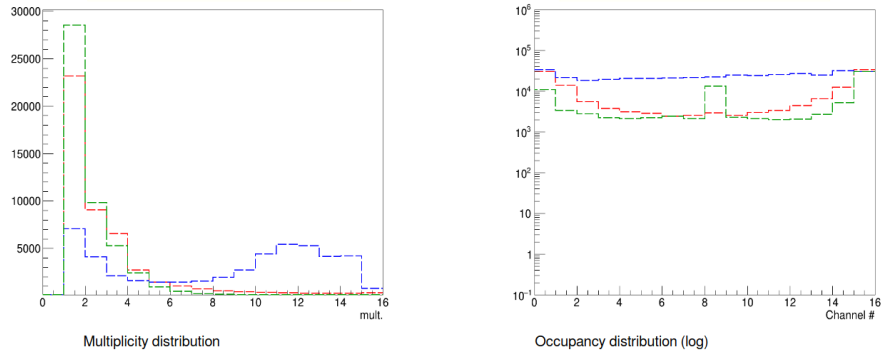

Figure 8.11. | Multiplicity and Occupancy distributions of 3 different RPCs in the CMS clean room. The green plot represents the Readout version 2.1 (See section 6.3), but with 50Ω termination, the blue plot represents the RPC with readout board version 3.0 (See section 6.4) and red represents the chamber with readout board Version 1.0 (See section 6.4).

From the figures 8.10 and figure 8.11, it is clearly visible that the total number of hits, is reduced in the clean room, which therefore reduces the ambient noise inside the clean room, which is a Faraday cage.

8.3. Tests with external trigger

The experimental results in the section 8.2 led us to develop an external scintillator to trigger the setup. The process of developing the system is described in Chapter 4. The implementation of the external trigger setup in the performance studies was done in two steps.

8.3.1. PMT to the CMS FEB

Connecting outputs from two scintillators directly to the two connection modules (34 pin male connectors) in the DAQ, so we don't have to re-program the FPGA inside the DAQ for another data acquisition program and solder new connectors or wires to the main board of the DAQ. So the discrimination of the PMT signal is done by the CMS FEB. Since the amplitude of the PMT signals is higher than the RPC signals, we had to use two modules from connections A, B, C, and D. We chose A and D to connect the PMT + Scintillator setup for convenience. Since the working threshold of the DAQ varies depending on the pulse amplitude, we did a threshold scan for the 2 online coincidences of the DAQ for 2 minutes in each threshold.

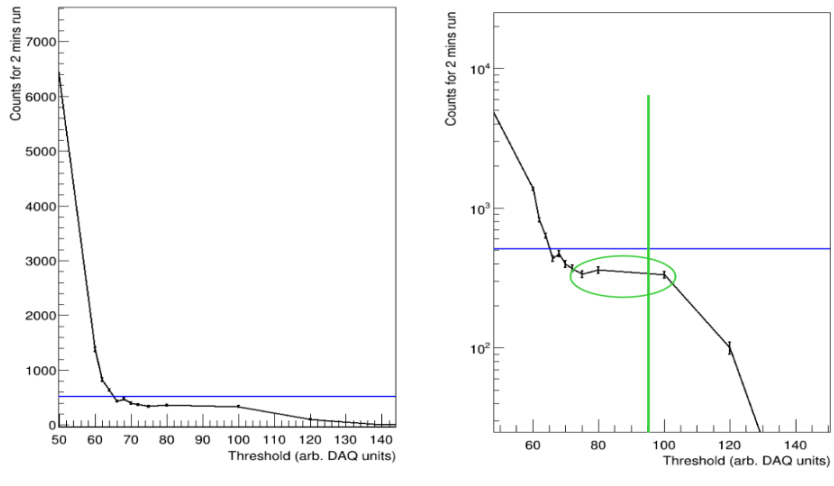

Figure 8.12. The plot of the number of coincidences in PMT as a function of the threshold. The left figure shows the count axis in the linear scale, and the right figure shows it in the log scale for better visibility of the plateau.

The scan results are shown in the figure 8.12. The horizontal blue line represents the roughly expected number of events in 2 minutes, which is 512. The vertical green line denotes the threshold of 95 DAQ units, which we chose as PMT's threshold. Since DAQ was designed and programd for RPCs only, when we plug in the PMT+Scintillator setup. We needed to adjust the program for both

PMTs and RPCs. After many iterations, we concluded the data acquisition program as shown in the figure 8.13. New timing parameters were introduced to the system. We are now able to delay each channel (A, B, C, and D) separately, and also setup the coincidence window (Equation 8.2) between all detectors. These parameters can be adjusted from the shell script and both GUIs.

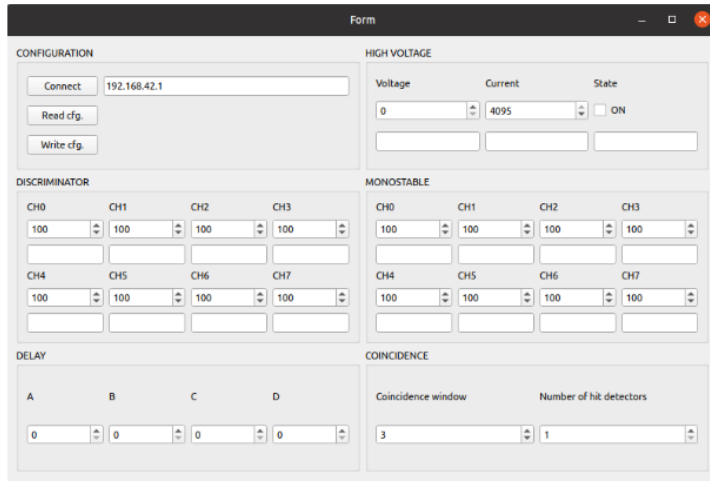

Figure 8.13. | Data acquisition program compatible with PMTs and RPCs.

$$CoinWindow\,[ns] = (coinValue\,[DAQ\ units] + 2) \times 5\,ns \qquad (8.2.)$$

8.3.2. Delay scan for RPC

The RPC signals are faster than the PMT signals (see Figure 8.14). So to find the calibration for the delay between two signals in the DAQ, an experiment was designed as follows:

- One RPC chamber sand-witched between 2 scintillators.
- High voltage of the RPC : - 6.6 kV
- Threshold value of RPC : 50 DAQ units
- coincidence window of the DAQ : 20 ns
- Delay : 3 -15 DAQ time units (one time unit in DAQ is equal to 5 ns, which corresponds to the clock frequency of the FPGA, so it is 20 ns to 60 ns with the step size of 5 ns)
- Time for 1 data point : 10 minutes

The data were taken for each delay value, and the number of coincidences between PMTs and RPC is shown in the plot in Figure 8.15. According to this plot, the delay value of 35 ns can be used in the data collection process. This experiment was done in the CMS clean room.

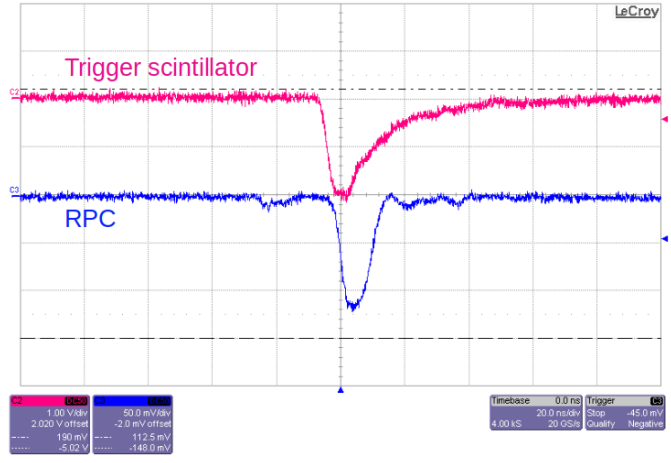

Figure 8.14. | The coincidence between RPC signal from 1 strip of the RPC and scintillator, The RPC signal was delayed by 50 ns using cables and a delay module.

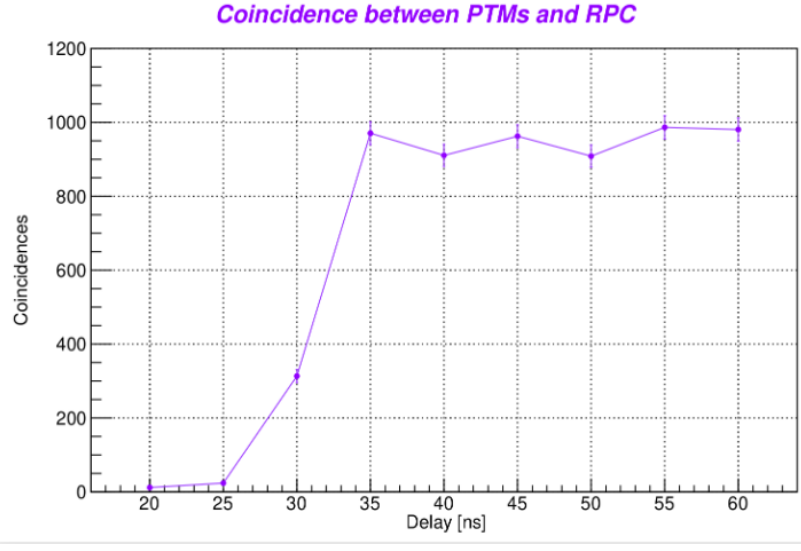

Figure 8.15. | Number of coincidences for different delay values of the RPC signal.

Although the delay scan shows 35 ns is the proper delay, we had to change the signal cable to be an additional 1 m long for the RPC, so we are using the delay of 30 ns in the DAQ, which corresponds to 6 DAQ delay units. Since we have a working external trigger, we proceed with the efficiency calculation of the RPC using the DAQ system. Before this setup, we could only do it using external

NIM electronics, and we didn't have multiplicity data to verify the quality of the RPC.

8.3.3. High voltage scan with external trigger

The high voltage scan of the RPC D (name of the chamber) with readout board v2.1 was sandwitched between the two scintillators used in the experiment. By that time, we already had readout versions 1.0, 2.1, and 3.0. But the data from v1.0 always had more noise, so we decided to go with v2.1. In this scan, an internal negative high voltage supply is used to change the high voltage, and the threshold of the RPC was set to 50 DAQ units. And the time for each data point was 10 minutes.Online coincidence was set to two. But in the data analysis, three coincidences were taken into account to account for the behaviour of the RPC.

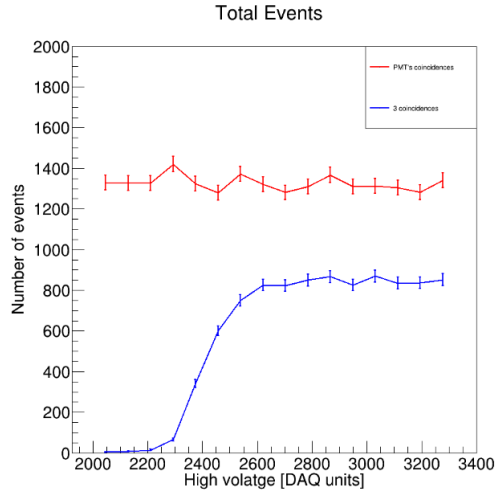

Figure 8.16. | Behaviour of RPCs (blue) and PMTs (red) as a function of the high voltage supplied. The PMT coincidence count isn't affected by the high voltage because it's powered by a fixed power supply. Note that high voltage is in the DAQ unit (the conversion factor can be found in equation 8.1)

The efficiency of the RPC as a function of the high voltage is calculated from the equation A.1. The efficiency variation of the RPC as a function of high voltage supplies is shown in the figure 8.17. With this setup, we could reach up to 60% of efficiency.

$$Efficiency(\epsilon) = \frac{T\&B\&RPC}{T\&B} \tag{8.3.}$$

Where T and B are trigger scintillators place on top and bottom of the RPC.

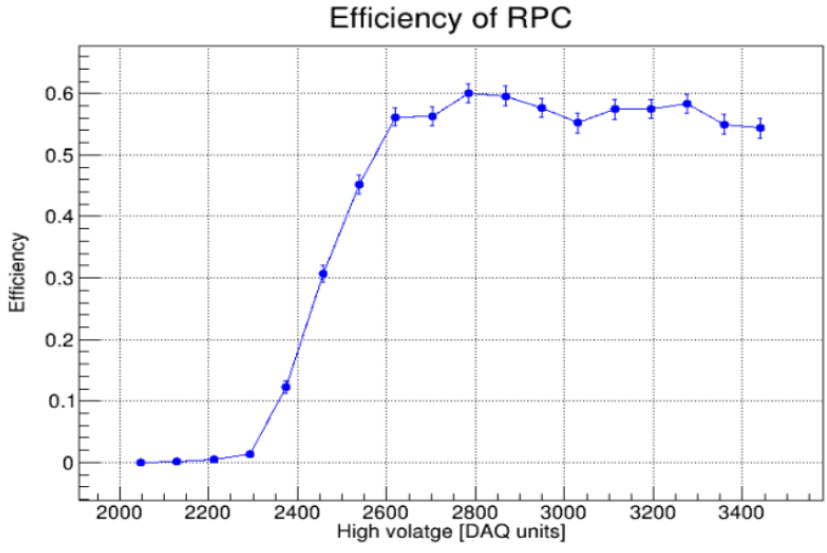

Figure 8.17. | Efficiency variation of the RPC as a function of high voltage.

The multiplicity and occupancy plots are shown in the figure 8.18 for the -8 kV (~ 3277 DAQ unit). In the multiplicity plot more than 80% of hits are with 1 hit per layer and more than 90% of the data are limited to 2 hits per layer. And in the occupancy plot, the more hits are in the middle of the RPC and corner strips fired less than middle, which is expected behaviour of the RPC.

8.3.4. Threshold scan

This section provides an understanding of the lowest threshold we could reach with the trigger system. The plot in the figure 8.19.

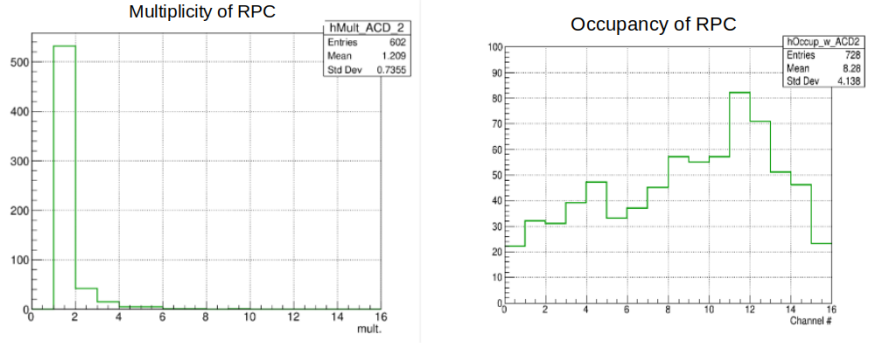

Figure 8.18. | Occupancy and multiplicity plots for -8 kV of high voltage.

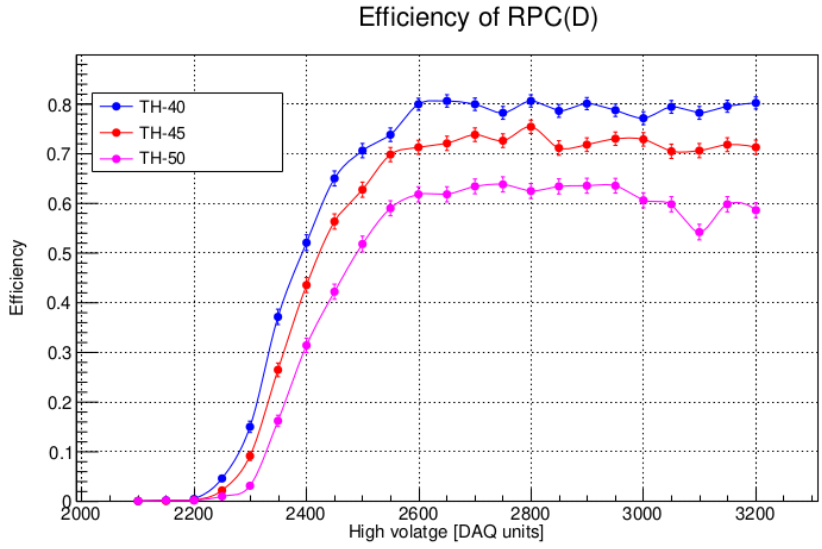

Figure 8.19. | High voltage scan for different threshold values.

We could reach up to 80% of efficiency with a threshold value of 40. The PMT coincidences removed the noise we saw in the self-trigger mode.

8.3.5. Joint data taking with UGent detector

We have a collaboration between UCLouvain and UGhent for muography. With this setup, We did a joint data taking campaign in University of Ghent to cross validate the performances although the 2 RPCs are slightly different from each other. The main differences between prototypes 1.L (UCLouvain) and 1.G (UGhent) are summarized in Table 8.1.

We made a joint data taking of two prototypes connected to the DAQ of Prototype 1.L in order to cross-validate their performances. Working points were set to our first estimated values which are HV = 7 kV and a threshold discriminator value of 90 DAQ units. In Fig. 8.20 the occupancy (i.e. number of times each strip fired throughout the run) and the multiplicity (i.e. total number of strips fired per event) are shown. Although both detectors have 16 strips, the plots only shows the result from the last 8 strips, as the first 4-5 strips in the Prototype 1.G were affected by hardware related issues that were fixed only after this data collection.

In Fig. 8.20, both distributions are normalized to the 1.L active area. The occupancy distributions of both prototypes are in general agreement. So we can conclude the two detectors behave in the same way, which cross-validates each. However, we observe a difference in the multiplicity distribution, which is higher in 1.G. This could be explained with the difference in the resistivity of

Property	Prototype 1.G	Prototype 1.L
Active area	28×28 cm^2	16×16 cm^2
Gas Flow	Continuous	Sealed
Glass thickness	1.3 mm	1.1 mm
Strip Width	15 mm	9 mm
Strip Pitch	16.6 mm	10 mm
Semi-resistive coating	Hand-sprayer (~ 450 $K\Omega/\square$)	Serigraphy (~ 4 $M\Omega/\square$)
DAQ	NIM + CAEN integrated	Custom made
Portability	Not yet	Portable

Table 8.1. Main differences between the two RPC prototypes developed so far [124].

the glass plates, which is smaller for 1.G than 1.L.

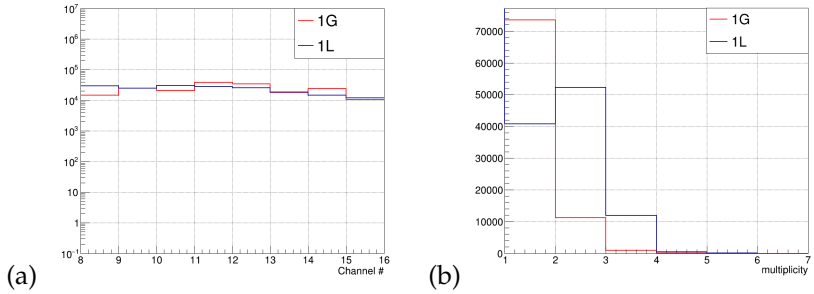

Figure 8.20. (a) Occupancy: number of times each strip fired throughout the data-taking run. (b) Multiplicity: total number of strips fired per event. [124]

8.4. PMT to the FPGA through external electronics

8.4.1. FPGA testing

Connecting external trigger directly to the FPGA in the main board of the DAQ (This is described in the section 4.3). After finalizing the electronics for the trigger, the DAQ is re-programd with a trigger system. The LVDS termination is enabled in the FPGA, because we saw some reflections from the FPGA output. We had to add 2.5 V power supply to the FPGA board.

In the muoscope DAQ, we have pins of the FPGA connected to the LIMO output cable in order to spy on the signals when needed. We can program this pin when needed. The blue line in Figure 8.21 is when one of the pins was programd to output the edge trigger of the PMT signal.

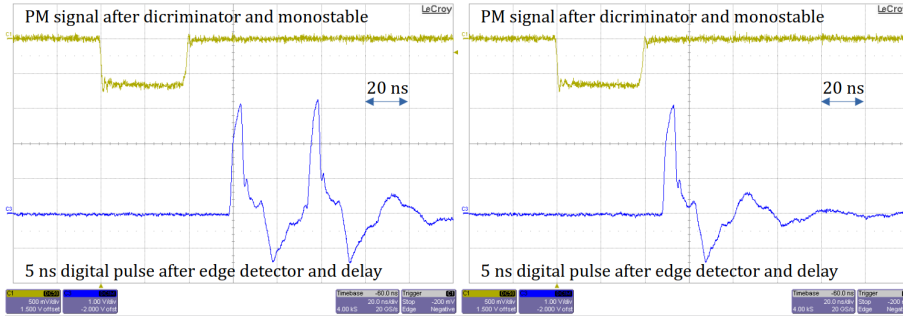

Figure 8.21. | FPGA output before and after termination enable. The yellow line corresponds to the output signal from the monostable of the external electronics and the blue line corresponds to the output of edge detector in the FPGA. Before termination enables, there are two or more edge detection happens in the FPGA due to the reflections.

8.4.2. Delay testing

We had to measure the time difference between the RPC signal and the PMT signal because we introduced three new modules to the system. The FPGA signals of RPC and PMT were output by the two spying pins. Figure 8.22's oscillogram displays the signal coming from both RPCs and PMTs. The PMT signal and RPC signal, which are in the same 20 ns time bin when the RPC is delayed by 50 ns, are visible in the oscillogram.

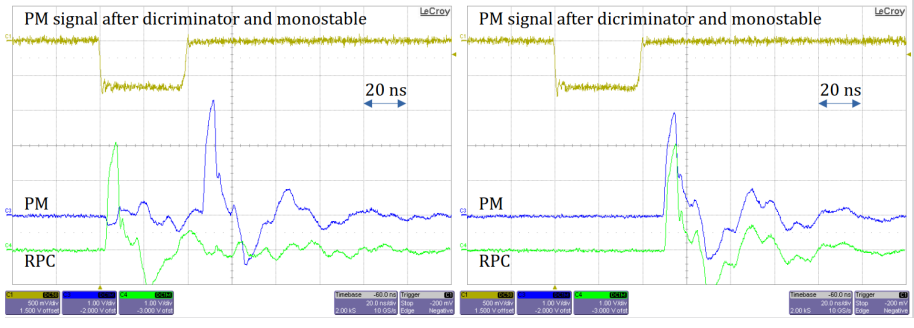

Figure 8.22. | RPC (green) and PMT (blue) signal without any delay (left).RPC (green) signal is delayed with 50 ns and PMT (blue) signal without any delay (right).

Delay measurements with DAQ system

With the DAQ, we measured the delay. Two coincident PMT signals are used as the trigger in the DAQ program, and the RCP's delay was set to 75 ns. After the trigger, 50 LVDS input samples were continuously captured. We counted and showed the number of samples with one hit and with multiple hits (see Figure 8.23.)

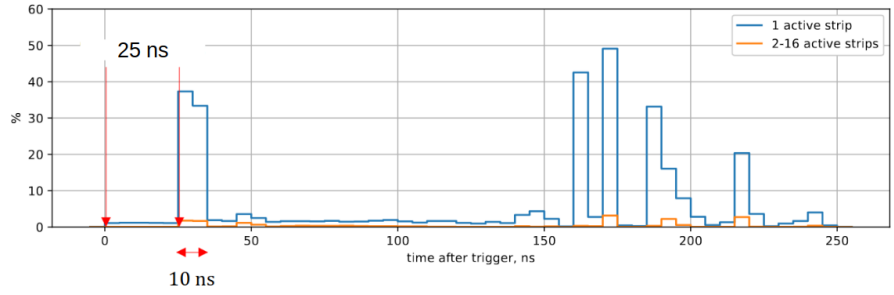

Figure 8.23. Hits in RPC after triggering. In this plot, the Y-axis denotes the efficiency of the detector with respect to the trigger, and X-axis is the time after trigger, the size a time bin is 5 ns.

After 25 ns, the RPC signal is visible in two consecutive bins in the figure 8.23. This demonstrates that the RPC signal was delayed by 50 ns, as the RPC signal was delayed by 75 ns and appeared in the data 25 ns later, concluding that the time difference between RPC and PTM is 50 ns. We chose a 10 ns coincidence window for data collection due to the fact that the signal is in two bins.

Validation of delay and coincidence window size

The purpose of this test was to validate the delay value and the extent of the coincidence window. The coincidence window was set to 10 ns, the delay was set to 50 ns, and data collection was triggered by a PMT coincidence.

The multiplicity (or hits per detector) and occupancy of the data were shown in the figure 8.24. The multiplicity of the RPC is limited to the maximum of three and occupancy is acceptable.

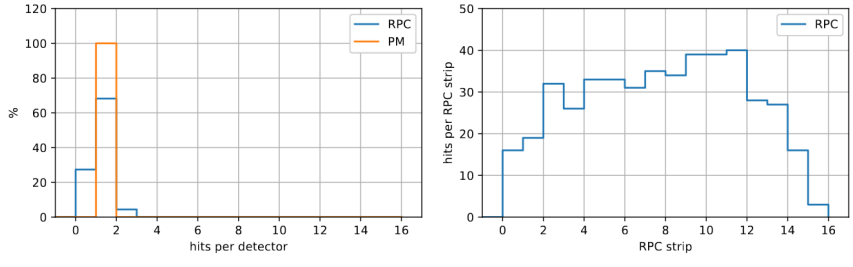

Figure 8.24. Multiplicity and occupancy of the RPC with the 10ns coincidence window and 50 ns of delay setup by the DAQ.

8.4.3. The muoscope's latest data acquisition program

After several iterations, we decided to use two PMT coincidences as the trigger and capture 250 data samples in succession after the trigger. The duration of

each sample is 5 nanoseconds. We delay the RPC signal by 670 nanoseconds. Thus, we could examine the behaviour of the readout strips (noise) prior to the avalanche signal and the behaviour of the strips following the signal (tail).

The diagram 8.25 depicts the timing distribution of the latest DAQ program.

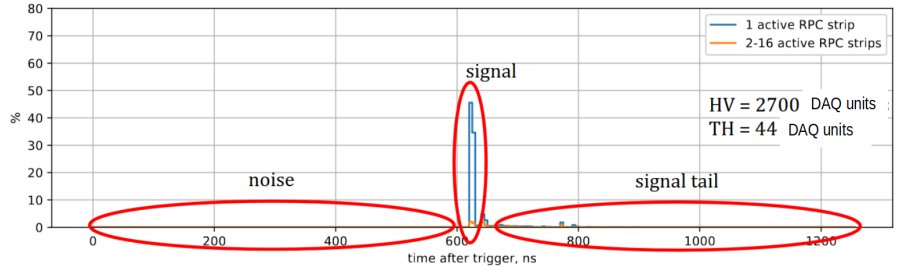

Figure 8.25. Noise, signal and signal tail of the RPC. The Y-axis denotes the efficiency with respect to the PMT trigger.

8.4.4. Noise and signal study

This test was done with RPC chamber with readout v2.1. The noise was observed as a function of efficiency (hits with respect to PMT trigger). The data were taken with different high voltage values and threshold values.

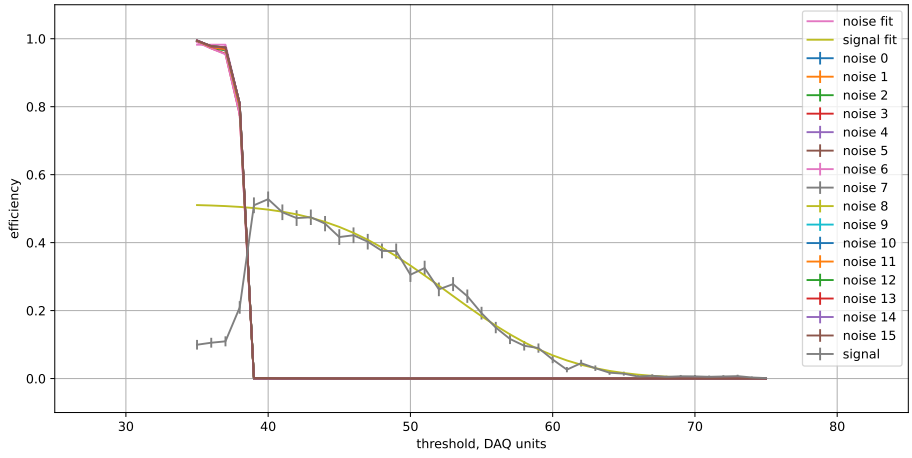

Figure 8.26. Threshold scan for signal and noise in the RPC, the high voltage supplied for the RPC is -5.8 kV.

The figure 8.26 shows the noise and signal as functions of the threshold. As seen, for thresholds less than 40 DAQ units, it fires every strip with an efficiency of 100% and after 40, the noise level goes almost up to 0 and signal efficiency is

visible. This plot is for -5.8 kV (2400 high voltage DAQ units), see figure 8.17, which is below the average working high voltage.

The noise as a function of high voltage and threshold is shown in the figure 8.27.

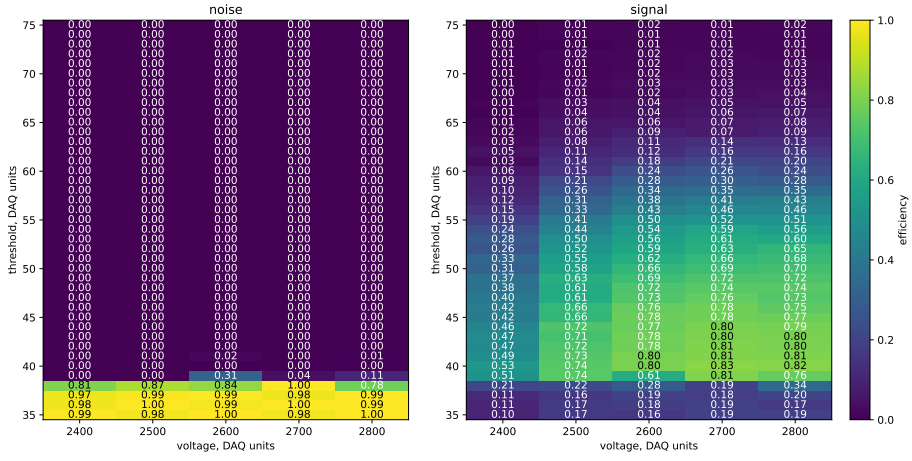

Figure 8.27. Noise as a function of threshold and high voltage (left). The efficiency of the RPC as a function of high voltage and threshold setting. The colour represents the efficiency, normalised between 0 and 1.

There are a few observations from the plots in the figure 8.27. The noise before the signal doesn't change with the high voltage supplied to the detector. and for low thresholds, it fires every strip. Later, we found that this noise was reduced with proper grounding of the detector and electronics. For the low threshold values, the signal is masked by the constant firing of the strips with noise.The highest efficiency the detector reached was 83% and high voltage was set to 2700 DAQ HV units, within the threshold of 40.

8.5. Readout Board behaviors

In this section, we are comparing the behaviour of detectors assembled with different readout boards (v2.1, see section 6.3 and v4.0, see section 6.5). The data were taken for 15 hours with a high voltage supply of -6.6 kV (~2700 DAQ HV units) and a threshold of 42. The timing distribution of detector A with a v4.0 readout board is shown in figure 8.28, and detector D with a v2.1 readout board is shown in figure 8.29). In both detectors, the noise prior to the signal is zero, and there are a few tails after the signal. For the moment, we neglect the post noise. The most needed part is the two signal bins. The efficiency of both chambers is not the same.

Although the efficiencies of the detectors are different, the behaviors of multiplicity and occupancy look alike (see figure 8.30). The readout boards are

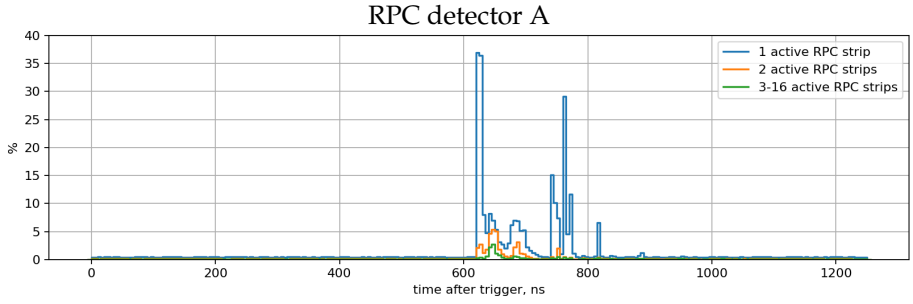

Figure 8.28. Time distribution of the Chamber A

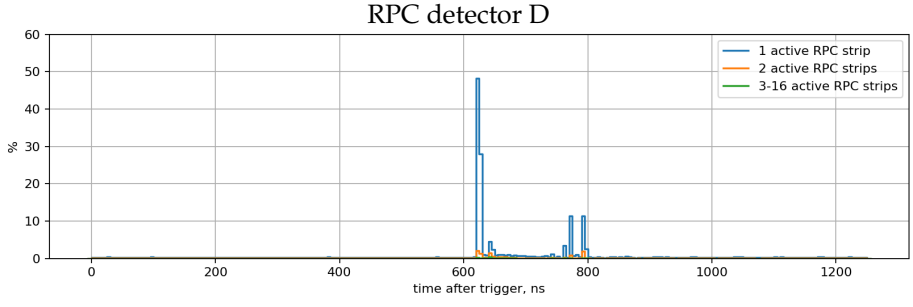

Figure 8.29. Time distribution of the Chamber D

working fine, so we decided to go with v4.0 since we can reproduce it easily via a company.

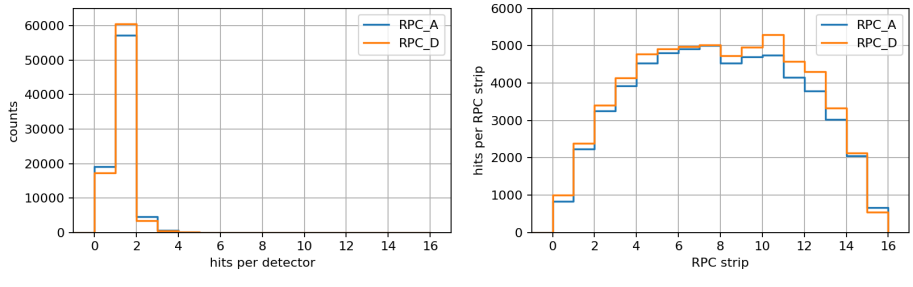

Figure 8.30. Occupancy and multiplicity plots for Chambers A and D.

8.5.1. Current drawn by RPC

To determine the operating HV of the avalanche mode, the ohmic behaviour of the detector can be used. The current drawn by the detector was measured as a function of HV. In avalanche mode, the current drawn by the detector behaves linearly with respect to HV. This determined a working point between 6.4 kV and 7.0 kV.

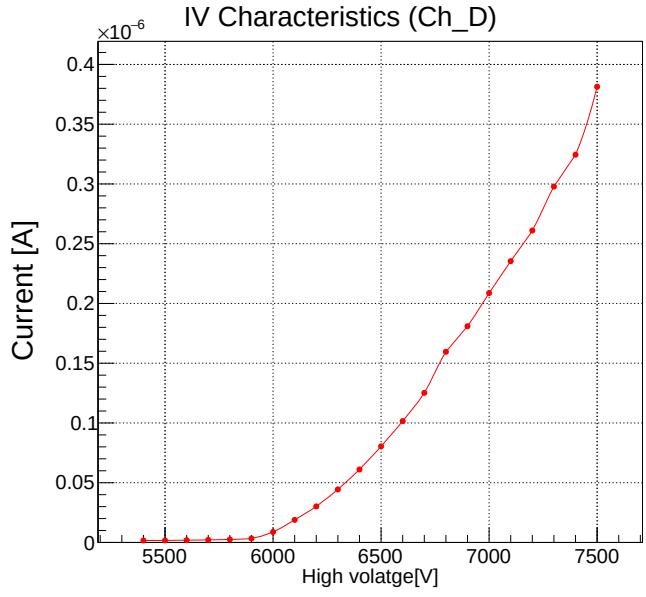

Figure 8.31. | The current drawn by then detectors as a function of high voltage supplied.

And with the IV curve, we can tell that the detector has some current leakage through the spacers and connectors. So after assembling a chamber, we do a current scan before the data collection process using atmospheric air.

Conclusion

Presently, there is an overwhelming demand for research and development (R&D) related to various Non-Destructive Evaluation (NDE) techniques for their application in numerous scientific and technological fields. Many imaging techniques fail in dangerous situations where human intervention is physically impossible, such as at the Fukushima reactor, the Khufu pyramid, and active volcanoes, among others. In other situations, partial or total destruction of targets is frequently required to identify flaws. Muography is a passive, non-hazardous NDE technique that uses the interaction between muons and matter to identify and image the target materials. Introduced in the 1950s, this technique gained popularity in the last decade of the 20th century as an alternative method for imaging natural and man-made structures. Later, it was found to have numerous applications in a variety of fields, such as detecting radioactive materials in cargo containers at borders, managing spent nuclear fuel and other waste, and monitoring. Numerous scientists all over the world are working on various aspects of muography, ranging from its instrumentation involving radiation detectors and electronics to the improvement of reconstruction algorithms and signal extraction via image processing.

This thesis focuses primarily on the development of resistive plate chamber (RPC) detectors. Typically, RPC detectors operate while the gas is flushing through the detector, which is not ideal for muography in a variety of applications. Although RPC detectors have been available since the 1980s, airtight RPC detectors are a recent development in the fields of muography and high-energy field physics.

We are part of the CP3 muography team, which is designing portable RPC detectors for muography, i.e. muoscope with sealed chambers and an integrated data acquisition system. The current muoscope prototype consists of two major components: four identical RPCs of $16 \times 16\,\mathrm{cm}^2$ active area housed in an airtight aluminium box and a data acquisition system (DAQ) with an integrated high-voltage supply. The initial prototype, however, required a number of upgrades. The system has a scintillator-based trigger system, and we are evaluating the system's RPC performance. Implementing the muoscope's trigger system was a significant improvement to the project. The trigger system has now been properly tested and calibrated, and we are using it to test each changes in the RPC like resistive plates with different surface resistivity, different versions of the readout boards etc. We are interested in the detector's efficiency, and the

RPC's multiplicity and occupancy, and its trigger system.

The RPC detector consists of three major components: the resistive plate, the gas mixture, and the readout system. In the CP3 laboratory, our RPC detectors use the gas mixture used in the CMS experiment. In the context of resistive plates, we use glass plates with a thickness of 1.1 mm. It is the most widely available and easily handled glass plate on the market. We examined various methods for applying resistive paint to glass plates with varying surface resistances. The production of glass resistive plates at the CEA facility in Saclay, France, using serigraphy method was a success; the RPCs demonstrated acceptable efficiencies and good multiplicities. With these plates, we observed the long-term stability of the resistivity. However, the production process is complex and costly. Thus, we initiated our own production in the laboratory as explained in the section 5.4. We calibrated the quantities of two components used to achieve the required surface resistivity values. The production procedure is accurately calibrated and thoroughly documented for future use. In addition, we are investigating the consistency of the resistivity of the initial batch. Due to the fact that we are still investigating the stability of the resistive coating, it has not been tested in RPC.

Utilisation of the readout board is the next critical aspect of the project. We determined after testing several boards to use readout version 4.0. Our current readout board's spatial resolution is 1 cm, with a width of 9 mm and a gap of 1 mm between each strip. We are terminating the readout strip with a 100-ohm resistor to reduce reflections on the front-end electronics of the DAQ. We discovered that this decreased the noise within the DAQ. We created several new readout boards (v5.0) with a grounding plane, whose investigation will be the topic of the future study.

We discovered that our laboratory's electrical grounding is poorly managed, resulting in enormous system noise. We are grounding our system to a different, less noisy ground. Even though the electromagnetic noise in the laboratory is not excessively high after turning off the radio antenna on the roof of our building, the aluminium chambers act as antennas for these noises and induce interference in sensitive electronics. With these system enhancements, we now have a working detector and could achieve efficiencies of up to 80%, which is an enormous improvement since the project's beginning. The system is equipped with the necessary software and hardware to test new prototypes. We have not conducted a systematic study to determine the stability of the detector's performance in sealed chambers over time, although we observed good performance in the context of the efficiency over 6–8 months after the initial filling of the chamber. Priority was placed on acquiring properly characterised and functioning detectors with adequate efficiency and performance. We will conduct a long-term investigation of detector performance.

While the first muoscope prototype is still in the research and development stage, we have laid the groundwork for the next high-resolution prototype. Since we are observing electromagnetic interference from the aluminium box, we will replace it with a frame that has been 3D printed. We will achieve the frame's gas tightness by adhering the resistive plates to the frame. The 3D printer is currently being tested with various frame materials. We will use a plastic box for the system's protection. The CMS front-end module will be replaced with a 64-channel MAROC 3A chip for each chamber. Thus, we are able to conduct high-resolution muography with our detector by giving 64 readout strips for each chamber. The spatial resolution must be precisely determined.

A. Chapter
Additional Material

A.1. Efficiency measurement with standard NIM electronics

This experiment is done with standard NIM electronic instead of the muoscope DAQ. The experimental setup was made as in the Figure 1.1, with the following electronic modules and LEMO cables. The NIM modules used in the setup are shown in the figure 1.2.

1. 3 Lecroy Model 623B Octal discriminator (18 discriminators were used).
2. 1 Lecroy Model 429A Logic fan in/ fan out unit.
3. 1 Lecroy Model 622 Quard coincidence module.
4. 1 borer delay module.
5. 16 Channel counter.
6. IPC Pre-selection timer counter.
7. 3 Dual scalers.
8. 32 2ns LIMO cables.
9. 18 1ns LIMO cables.
10. 10 LIMO cables (4-8 ns).
11. Wave pro 7300 A Oscilloscope.
12. RPC with new readout and DAQ intergrated high-voltage power supply (iseg DPS mini DPn)(figure 3.8 power supply.
13. 2 external scintillators and power supply.
14. Multimeter.

With this setup, it's possible to count individual hits from each strip in the RPC and two PMT counts, coincidences between two scintillators, OR operations of the 16 strips, coincidences between two scintillators, and OR operations of the 16 strips. 16 strips of RPC were connected to 16 separate discriminators (1–16). The threshold of the discriminator was set to -100 mV (-1 V from the value measured using a multimeter). The output signal was digitised with a width of 20 ns. There are three different outputs from the discriminator: one is connected to the 16-channel counter, and another is connected to the Lecroy Model 429A Logic fan in/fan out unit. The output of this module is the OR operation of 16 strips. The output of this module is connected to the delay module, and the delay is set to 35 ns.

The PMTs (T,B) were connected to two discriminator modules with a threshold of -400 mV (-4V from the value measured using a multimeter) and an output

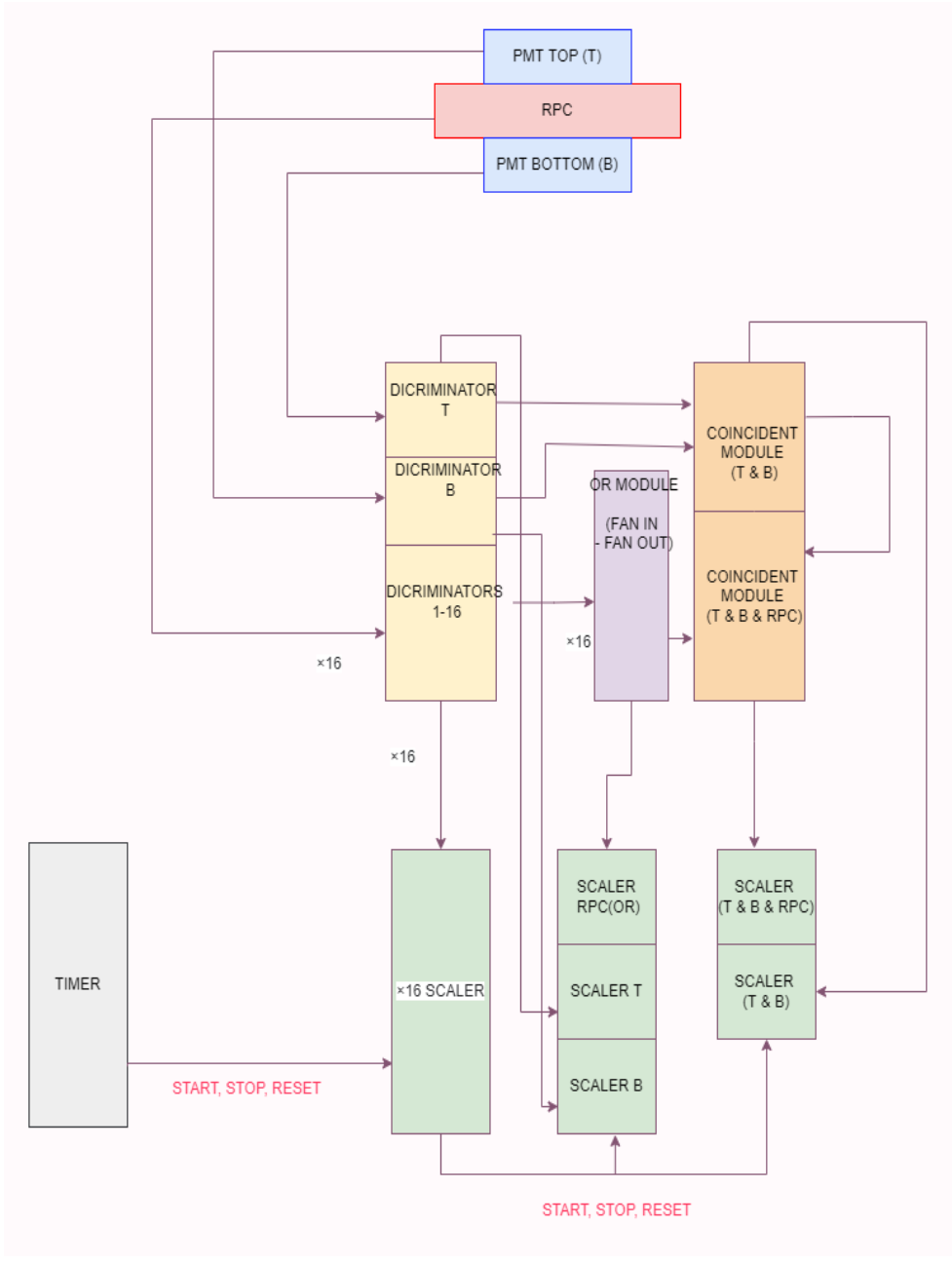

Figure 1.1. | Sketch of the Experimental Setup.

signal of 20 ns in width. One output of each discriminator (T, B) is connected to one channel of the dual scalar, and the other output is connected to the

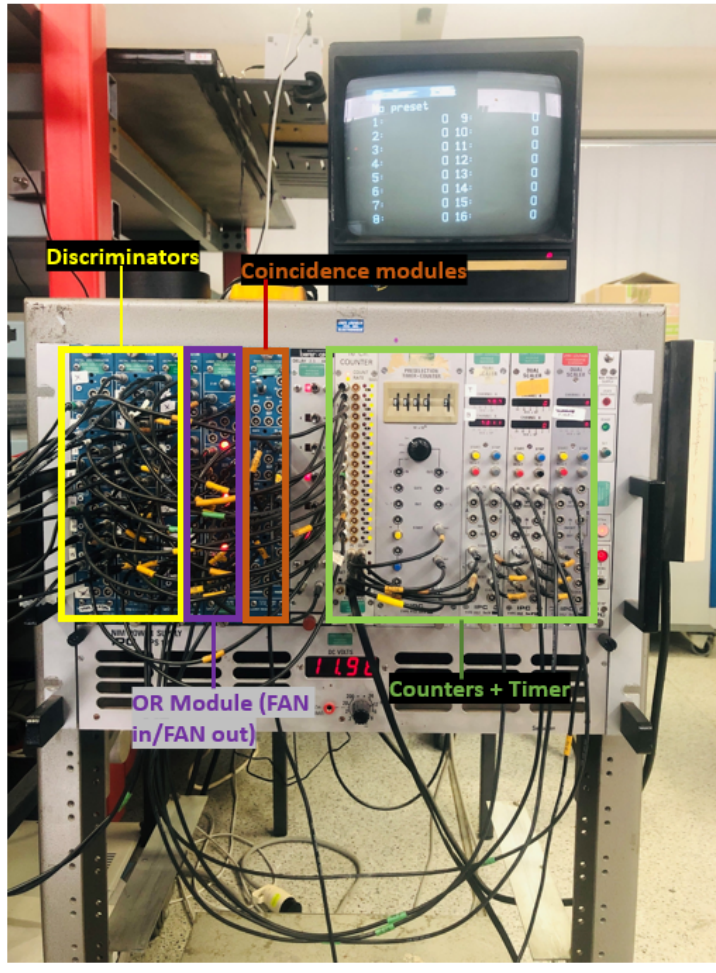

Figure 1.2. | NIM crate with all modules.

coincidence module (T&B). The output form (T&B) is connected to a counter and to another coincidence unit (T&B&RPC) while the other input of T&B&RPC is the delayed signal of the OR of 16 strips. The output of T&B&RPC is connected to a single channel of the dual scalar. The IPC pre-selection timer counter is connected to each counter to provide a signal to start, stop, and reset the counters. (Figure 1.1).

The counts for 600s from all the 5 scalars were recorded for different high voltage values from 2400 DAQ units to 3900 DAQ units with an increment of 100 DAQ units. And another set of readings of high voltage values 2540, 2580, 2620, and 2660.

Table 1.1. | Setup values of each NIM unit.

NIM Module	Threshold Value	Width of output
1-16 Discriminator	-100 mV	20 ns
T, B Discriminator	-400 mV	20 ns
OR module	-	40 ns
T&B Coincidence unit	-	40 ns
T&B&RPC Coincidence unit	-	40 ns

Delay unit	35 ns
Timer	600s

$$Efficiency(\epsilon) = \frac{T\&B\&RPC}{T\&B} \tag{A.1.}$$

References

[1] V.F. Hess, *Über Beobachtungen der durchdringenden Strahlung bei sieben Freiballonfahrten*, *Phys. Z.* **13** (1912) 1084.

[2] I.A. Grenier and A.K. Harding, *in Albert Einstein Century International Conference*, .

[3] S.H. Neddermeyer and C.D. Anderson, *Note on the Nature of Cosmic-Ray Particles*, *Phys. Rev.* **51** (1937) 884.

[4] P. Galison, *The Discovery of the Muon and the Failed Revolution against Quantum Electrodynamics*, *Centaurus* **50** (2008) 105.

[5] H. YUKAWA, *On the Interaction of Elementary Particles. I*, *Proceedings of the Physico-Mathematical Society of Japan. 3rd Series* **17** (1935) 48.

[6] M. Conversi, E. Pancini and O. Piccioni, *On the Disintegration of Negative Mesons*, *Phys. Rev.* **71** (1947) 209.

[7] C.M.G. LATTES, H. MUIRHEAD, G.P.S. OCCHIALINI and C.F. POWELL, *PROCESSES INVOLVING CHARGED MESONS*, *Nature* **159** (1947) 694.

[8] Particle Data Group collaboration, *Review of Particle Physics*, *PTEP* **2022** (2022) 083C01.

[9] M. Guan, M.-C. Chu, J. Cao, K.-B. Luk and C. Yang, *A parametrization of the cosmic-ray muon flux at sea-level*, 1509.06176.

[10] P.L. Rocca, D.L. Presti and F. Riggi, *Cosmic Ray Muons as Penetrating Probes to Explore the World around Us*, in *Cosmic Rays*, Z. Szadkowski, ed., (Rijeka), IntechOpen (2018).

[11] D.E. GROOM, N.V. MOKHOV and S.I. STRIGANOV, *MUON STOPPING POWER AND RANGE TABLES 10 MeV–100 TeV*, *Atomic Data and Nuclear Data Tables* **78** (2001) 183.

[12] V.L. Highland, *Some practical remarks on multiple scattering*, *Nuclear Instruments and Methods* **129** (1975) 497.

[13] G. Moliere, *Theorie der Streuung schneller geladener Teilchen II Mehrfach-und Vielfachstreuung*, *Zeitschrift für Naturforschung A* **3** (1948) 78.

[14] J.L. Uretsky, *Penetration of cosmic ray muons into the earth*, *Nuclear Instruments and Methods in Physics Research Section A: Accelerators, Spectrometers, Detectors and Associated Equipment* **399** (1997) 285.

[15] L. Bonechi, R. D'Alessandro and A. Giammanco, *Atmospheric muons as an imaging tool*, *Reviews in Physics* **5** (2020) 100038.

[16] H.K.M. Tanaka, T. Uchida, M. Tanaka, M. Takeo, J. Oikawa, T. Ohminato et al., *Detecting a mass change inside a volcano by cosmic-ray muon radiography (muography): First results from measurements at Asama volcano, Japan*, *Geophysical Research Letters* **36** (2009) [https://agupubs.onlinelibrary.wiley.com/doi/pdf/10.1029/2009GL039448].

[17] L. Oláh, G.G. Barnaföldi, G. Hamar, H.G. Melegh, G. Surányi and D. Varga, *CCC-based muon telescope for examination of natural caves*, *Geoscientific Instrumentation, Methods and Data Systems* **1** (2012) 229.

[18] Y.-S. Tsai, *Pair production and bremsstrahlung of charged leptons*, *Rev. Mod. Phys.* **46** (1974) 815.

[19] E.P. George, *Cosmic Rays Measure Overburden of Tunnel*, *Commonwealth Engineer* **July 1** (1955) 455.

[20] L.W. Alvarez, J.A. Anderson, F.E. Bedwei, J. Burkhard, A. Fakhry, A. Girgis et al., *Search for Hidden Chambers in the Pyramids*, *Science* **167** (1970) 832.

[21] K. Nagamine, M. Iwasaki, K. Shimomura and K. Ishida, *Method of probing inner-structure of geophysical substance with the horizontal cosmic-ray muons and possible application to volcanic eruption prediction*, *Nuclear Instruments and Methods in Physics Research Section A: Accelerators, Spectrometers, Detectors and Associated Equipment* **356** (1995) 585.

[22] H. Tanaka, K. Nagamine, N. Kawamura, S.N. Nakamura, K. Ishida and K. Shimomura, *Development of the Cosmic-Ray Muon Detection System for Probing Internal-Structure of a Volcano*, *Hyperfine Interactions* **138** (2001) 521.

[23] H.K.M. Tanaka, T. Kusagaya and H. Shinohara, *Radiographic visualization of magma dynamics in an erupting volcano*, *Nature Communications* **5** (2014) 3381.

[24] H.K.M. Tanaka, *Instant snapshot of the internal structure of Unzen lava dome, Japan with airborne muography*, *Scientific Reports* **6** (2016) 39741.

[25] H.K.M. Tanaka, *Visualization of the Internal Structure of Volcanoes with Cosmic-ray Muons*, *Journal of the Physical Society of Japan* **85** (2016) 091016.

[26] D. Carbone, D. Gibert, J. Marteau, M. Diament, L. Zuccarello and E. Galichet, *An experiment of muon radiography at Mt Etna (Italy)*, *Geophysical Journal International* **196** (2013) 633.

[27] N. Lesparre, D. Gibert, J. Marteau, Y. Déclais, D. Carbone and E. Galichet, *Geophysical muon imaging: feasibility and limits*, *Geophysical Journal International* **183** (2010) 1348.

[28] D. Gibert, F. Beauducel, Y. Déclais, N. Lesparre, J. Marteau, F. Nicollin et al., *Muon tomography: Plans for observations in the Lesser Antilles*, *Earth, Planets and Space* **62** (2010) 153.

[29] J. Marteau, D. Gibert, N. Lesparre, F. Nicollin, P. Noli and F. Giacoppo, *Muons tomography applied to geosciences and volcanology*, *Nuclear Instruments and Methods in Physics Research Section A: Accelerators, Spectrometers, Detectors and Associated Equipment* **695** (2012) 23.

[30] C. Carloganu, *Density Imaging of Volcanoes With Atmospheric Muons using GRPCs*, *PoS* **EPS-HEP2011** (2012) 055.

[31] G. Ambrosi, F. Ambrosino, R. Battiston, A. Bross, S. Callier, F. Cassese et al., *The MU-RAY project: Volcano radiography with cosmic-ray muons*, *Nuclear Instruments and Methods in Physics Research Section A: Accelerators, Spectrometers, Detectors and Associated Equipment* **628** (2011) 120.

[32] F. Ambrosino, A. Anastasio, D. Basta, L. Bonechi, M. Brianzi, A. Bross et al., *The MU-RAY project: Detector technology and first data from Mt. Vesuvius*, *Journal of Instrumentation* **9** (2014) C02029.

[33] G. Saracino, L. Amato, F. Ambrosino, G. Antonucci, L. Bonechi, L. Cimmino et al., *Imaging of underground cavities with cosmic-ray muons from observations at Mt. Echia (Naples)*, *Scientific Reports* **7** (2017) 1181.

[34] E. Caffau, F. Coren and G. Giannini, *Underground cosmic-ray measurement for morphological reconstruction of the "grotta gigante" natural cave*, *Nuclear Instruments and Methods in Physics Research Section A: Accelerators, Spectrometers, Detectors and Associated Equipment* **385** (1997) 480.

[35] L. Malmqvist, G. Jönsson, K. Kristiansson and L. Jacobsson, *Theoretical studies of in-situ rock density determinations using underground cosmic-ray muon intensity measurements with application in mining geophysics*, *GEOPHYSICS* **44** (1979) 1549.

[36] K. Morishima, M. Kuno, A. Nishio, N. Kitagawa, Y. Manabe, M. Moto et al., *Discovery of a big void in Khufu's Pyramid by observation of cosmic-ray muons*, *Nature* **552** (2017) 386.

[37] "ScanPyramids." `http://www.scanpyramids.org/index-en.html`.

[38] H. Gómez, C. Carloganu, D. Gibert, J. Jacquemier, Y. Karyotakis, J. Marteau et al., *Studies on muon tomography for archaeological internal structures scanning*, *Journal of Physics: Conference Series* **718** (2016) 052016.

[39] S. Aguilar, R. Alfaro, E. Belmont, R. Cadena, V. Grabski, T. Ibarra et al., *Searching for cavities in the teotihuacan pyramid of the sun using cosmic muons*, .

[40] S. Barnes, A. Georgadze, A. Giammanco, M. Kiisk, V.A. Kudryavtsev, M. Lagrange et al., *Cosmic-Ray Tomography for Border Security*,

Instruments **7** (2023) .

[41] K.N. Borozdin, G.E. Hogan, C. Morris, W.C. Priedhorsky, A. Saunders, L.J. Schultz et al., *Radiographic imaging with cosmic-ray muons*, *Nature* **422** (2003) 277.

[42] L. Schultz, K. Borozdin, J. Gomez, G. Hogan, J. McGill, C. Morris et al., *Image reconstruction and material Z discrimination via cosmic ray muon radiography*, *Nuclear Instruments and Methods in Physics Research Section A: Accelerators, Spectrometers, Detectors and Associated Equipment* **519** (2004) 687.

[43] K. Gnanvo, L.V. Grasso, M. Hohlmann, J.B. Locke, A. Quintero and D. Mitra, *Imaging of high-Z material for nuclear contraband detection with a minimal prototype of a muon tomography station based on GEM detectors*, *Nuclear Instruments and Methods in Physics Research Section A: Accelerators, Spectrometers, Detectors and Associated Equipment* **652** (2011) 16.

[44] P. Baesso, D. Cussans, C. Thomay and J. Velthuis, *Toward a RPC-based muon tomography system for cargo containers.*, *Journal of Instrumentation* **9** (2014) C10041.

[45] V. Anghel, J. Armitage, F. Baig, K. Boniface, K. Boudjemline, J. Bueno et al., *A plastic scintillator-based muon tomography system with an integrated muon spectrometer*, *Nuclear Instruments and Methods in Physics Research Section A: Accelerators, Spectrometers, Detectors and Associated Equipment* **798** (2015) 12.

[46] S. Pesente, S. Vanini, M. Benettoni, G. Bonomi, P. Calvini, P. Checchia et al., *First results on material identification and imaging with a large-volume muon tomography prototype*, *Nuclear Instruments and Methods in Physics Research Section A: Accelerators, Spectrometers, Detectors and Associated Equipment* **604** (2009) 738.

[47] D. Poulson, J. Durham, E. Guardincerri, C. Morris, J. Bacon, K. Plaud-Ramos et al., *Cosmic ray muon computed tomography of spent nuclear fuel in dry storage casks*, *Nuclear Instruments and Methods in Physics Research Section A: Accelerators, Spectrometers, Detectors and Associated Equipment* **842** (2017) 48.

[48] A. Clarkson, D. Hamilton, M. Hoek, D. Ireland, J. Johnstone, R. Kaiser et al., *Characterising encapsulated nuclear waste using cosmic-ray muon tomography*, *Journal of Instrumentation* **10** (2015) P03020.

[49] A. Clarkson, D. Hamilton, M. Hoek, D. Ireland, J. Johnstone, R. Kaiser et al., *The design and performance of a scintillating-fibre tracker for the cosmic-ray muon tomography of legacy nuclear waste containers*, *Nuclear Instruments and Methods in Physics Research Section A: Accelerators, Spectrometers, Detectors and Associated Equipment* **745** (2014) 138.

[50] X. Wang, M. Zeng, Z. Zeng, Y. Wang, Z. Zhao, X. Yue et al., *The cosmic ray muon tomography facility based on large scale MRPC detectors*, *Nuclear Instruments and Methods in Physics Research Section A: Accelerators, Spectrometers, Detectors and Associated Equipment* **784** (2015) 390.

[51] G. Jonkmans, V. Anghel, C. Jewett and M. Thompson, *Nuclear waste imaging and spent fuel verification by muon tomography*, *Annals of Nuclear Energy* **53** (2013) 267.

[52] S. Chatzidakis, C. Choi and L. Tsoukalas, *Interaction of cosmic ray muons with spent nuclear fuel dry casks and determination of lower detection limit*, *Nuclear Instruments and Methods in Physics Research Section A: Accelerators, Spectrometers, Detectors and Associated Equipment* **828** (2016) 37.

[53] S. Bouteille, D. Attié, P. Baron, D. Calvet, P. Magnier, I. Mandjavidze et al., *A Micromegas-based telescope for muon tomography: The WatTo experiment*, *Nuclear Instruments and Methods in Physics Research Section A: Accelerators, Spectrometers, Detectors and Associated Equipment* **834** (2016) 223.

[54] J.M. Durham, E. Guardincerri, C.L. Morris, J. Bacon, J. Fabritius, S. Fellows et al., *Tests of cosmic ray radiography for power industry applications*, *AIP Advances* **5** (2015) 067111 [https://doi.org/10.1063/1.4922006].

[55] *Muon Imaging*, TECDOC Series, INTERNATIONAL ATOMIC ENERGY AGENCY, Vienna (2022).

[56] L. Cimmino, F. Ambrosino, A. Anastasio, M. D'Errico, V. Masone, L. Roscilli et al., *A new cylindrical borehole detector for radiographic imaging with muons*, *Scientific Reports* **11** (2021) 17425.

[57] C. Bozza, L. Consiglio, N. D'ambrosio, G.D. Lellis, C.D. Sio, S. Miyamoto et al., *Nuclear emulsion techniques for muography*, *Annals of Geophysics* **60** (2017) S0109.

[58] D. Di Ferdinando, *Nuclear emulsions in the OPERA experiment*, *Radiation Measurements* **44** (2009) 840.

[59] R. Nishiyama, A. Ariga, T. Ariga, S. Käser, A. Lechmann, D. Mair et al., *First measurement of ice-bedrock interface of alpine glaciers by cosmic muon radiography*, *Geophysical Research Letters* **44** (2017) 6244 [https://agupubs.onlinelibrary.wiley.com/doi/pdf/10.1002/2017GL073599].

[60] R. Nishiyama, A. Ariga, T. Ariga, A. Lechmann, D. Mair, C. Pistillo et al., *Bedrock sculpting under an active alpine glacier revealed from cosmic-ray muon radiography*, *Scientific Reports* **9** (2019) 6970.

[61] V. Tioukov, A. Alexandrov, C. Bozza, L. Consiglio, N. D'Ambrosio, G. De Lellis et al., *First muography of Stromboli volcano*, *Scientific Reports* **9** (2019) 6695.

[62] G. Charpak, R. Bouclier, T. Bressani, J. Favier and Zupančič, *The use of multiwire proportional counters to select and localize charged particles*, *Nuclear Instruments and Methods* **62** (1968) 262.

[63] D. Varga, G. Nyitrai, G. Hamar, G. Galgóczi, L. Oláh, H. Tanaka et al., *Detector developments for high performance Muography applications*, *Nuclear Instruments and Methods in Physics Research Section A: Accelerators, Spectrometers, Detectors and Associated Equipment* **958** (2020) 162236.

[64] R.C. Fernow, *Drift chambers*, in *Introduction to Experimental Particle Physics*, p. 234–258, Cambridge University Press (1986), DOI.

[65] N.I. Bozhko, A.A. Borisov, A.S. Kozhin and R.M. Fakhrutdinov, *Cosmic-Ray Muon Tomography Setup: Long-Term Life of Drift Tube Chambers*, *Physics of Atomic Nuclei* **83** (2020) 258.

[66] J. Burns, S. Quillin, M. Stapleton, C. Steer and S. Snow, *A drift chamber tracking system for muon scattering tomography applications*, *Journal of Instrumentation* **10** (2015) P10041.

[67] V. Anghel, J. Armitage, J. Botte, K. Boudjemline, D. Bryman, E. Charles et al., *Cosmic ray muon tomography system using drift chambers for the detection of Special Nuclear Materials*, *IEEE Nuclear Science Symposium Conference Record* (2010) .

[68] Y. Giomataris, P. Rebourgeard, J. Robert and G. Charpak, *MICROMEGAS: a high-granularity position-sensitive gaseous detector for high particle-flux environments*, *Nuclear Instruments and Methods in Physics Research Section A: Accelerators, Spectrometers, Detectors and Associated Equipment* **376** (1996) 29.

[69] R. Santonico and R. Cardarelli, *Development of resistive plate counters*, *Nuclear Instruments and Methods in Physics Research* **187** (1981) 377.

[70] R. Cardarelli, V. Makeev and R. Santonico, *Avalanche and streamer mode operation of resistive plate chambers*, *Nuclear Instruments and Methods in Physics Research Section A: Accelerators, Spectrometers, Detectors and Associated Equipment* **382** (1996) 470.

[71] I. Crotty, J. Lamas Valverde, G. Laurenti, M. Williams and A. Zichichi, *Further studies of avalanche mode operation of resistive parallel plate chambers*, *Nuclear Instruments and Methods in Physics Research Section A: Accelerators, Spectrometers, Detectors and Associated Equipment* **346** (1994) 107.

[72] I. Crotty, J. Lamas Valverde, G. Laurenti, M. Williams and A. Zichichi, *The non-spark mode and high rate operation of resistive parallel plate chambers*, *Nuclear Instruments and Methods in Physics Research Section A: Accelerators, Spectrometers, Detectors and Associated Equipment* **337** (1994) 370.

[73] M. Abbrescia, A. Colaleo, G. Iaselli, M. Maggi, B. Marangelli, S. Natali et al., *Properties of C2H2F4-based gas mixture for avalanche mode operation of resistive plate chambers*, *Nuclear Instruments and Methods in Physics Research Section A: Accelerators, Spectrometers, Detectors and Associated Equipment* **398** (1997) 173.

[74] P. Camarri, R. Cardarelli, A. Ciaccio and R. Santonico, *Streamer suppression with SF6 in RPCs operated in avalanche mode*, *Nuclear Instruments and Methods in Physics Research Section A: Accelerators, Spectrometers, Detectors and Associated Equipment* **414** (1998) 317.

[75] E. Cerron Zeballos, I. Crotty, D. Hatzifotiadou, J. Lamas Valverde, S. Neupane, M. Williams et al., *A new type of resistive plate chamber: The multigap RPC*, *Nuclear Instruments and Methods in Physics Research Section A: Accelerators, Spectrometers, Detectors and Associated Equipment* **374** (1996) 132.

[76] M. Williams, *The development of the multigap resistive plate chamber*, *Nuclear Physics B - Proceedings Supplements* **61** (1998) 250.

[77] M. Abbrescia, A. Colaleo, G. Iaselli, F. Loddo, M. Maggi, B. Marangelli et al., *The rpc system for the cms experiment at the lhc*, *Nuclear Instruments and Methods in Physics Research Section A: Accelerators, Spectrometers, Detectors and Associated Equipment* **508** (2003) 137.

[78] G. Aielli, M. Alviggi, A. Ammosov, M. Biglietti, E. Brambilla, P. Camarri et al., *Test and performances of the rpc trigger chambers of the atlas experiment at lhc*, *Nuclear Instruments and Methods in Physics Research Section A: Accelerators, Spectrometers, Detectors and Associated Equipment* **533** (2004) 193.

[79] A. Akindinov, A. Alici, P. Antonioli, S. Arcelli, Y. Baek, M. Basile et al., *Construction and tests of the mrpc detectors for tof in alice*, *Nuclear Instruments and Methods in Physics Research Section A: Accelerators, Spectrometers, Detectors and Associated Equipment* **602** (2009) 658.

[80] CALICE collaboration, *Description and stability of a RPC-based calorimeter in electromagnetic and hadronic shower environments*, *JINST* **18** (2023) P03035 [2207.06291].

[81] H. Bethe and W. Heitler, *On the stopping of fast particles and on the creation of positive electrons*, *Proceedings of the Royal Society of London. Series A, Containing Papers of a Mathematical and Physical Character* **146** (1934) 83.

[82] W. Riegler, C. Lippmann and R. Veenhof, *Detector physics and simulation of resistive plate chambers*, *Nuclear Instruments and Methods in Physics Research Section A: Accelerators, Spectrometers, Detectors and Associated Equipment* **500** (2003) 144.

[83] F.E. Taylor, *A model of the limited streamer mechanism*, *Nuclear Instruments and Methods in Physics Research Section A: Accelerators, Spectrometers, Detectors and Associated Equipment* **289** (1990) 283.

[84] W. Shockley, *Currents to Conductors Induced by a Moving Point Charge*, *Journal of Applied Physics* **9** (1938) 635 [https://pubs.aip.org/aip/jap/article-pdf/9/10/635/8059000/635_1_online.pdf

[85] S. Ramo, *Currents Induced by Electron Motion*, *Proceedings of the IRE* **27** (1939) 584.

[86] W. Riegler, *Induced signals in resistive plate chambers*, *Nuclear Instruments and Methods in Physics Research Section A: Accelerators, Spectrometers, Detectors and Associated Equipment* **491** (2002) 258.

[87] C. Lu, *Rpc electrode material study*, *Nuclear Instruments and Methods in Physics Research Section A: Accelerators, Spectrometers, Detectors and Associated Equipment* **602** (2009) 761.

[88] X. Xie, G. Aielli, Z. Xue, J. Ge, Y. Sun, H. Liang et al., *A new approach in simulating RPC and searching for the causes of large cluster size of RPC*, *Journal of Instrumentation* **14** (2019) C09012.

[89] Q. Li, X. Xie, Z. Xue, J. Ge and Y. Sun, *A new layout about the graphite layers in RPC*, 2021.

[90] S. Basnet, E.C. Gil, P. Demin, R.M. Gamage, A. Giammanco, M. Moussawi et al., *Towards portable muography with small-area, gas-tight glass Resistive Plate Chambers*, *Journal of Instrumentation* **15** (2020) [2005.09589].

[91] M. Abbrescia, V. Peskov and P. Fonte, *Resistive Gaseous Detectors* (2018), 10.1002/9783527698691.

[92] G. Rigoletti, R. Guida and B. Mandelli, *Studies on RPC detectors operated with environmentally friendly gas mixtures in LHC-like conditions*, *Nuclear Instruments and Methods in Physics Research Section A: Accelerators, Spectrometers, Detectors and Associated Equipment* **1048** (2023) 167961.

[93] R. Guida, B. Mandelli and G. Rigoletti, *Studies on alternative eco-friendly gas mixtures and development of gas recuperation plant for RPC detectors*, *Nuclear Instruments and Methods in Physics Research Section A: Accelerators, Spectrometers, Detectors and Associated Equipment* **1039** (2022) 167045.

[94] R. Guida, B. Mandelli and G. Rigoletti, *Performance studies of RPC detectors with new environmentally friendly gas mixtures in presence of LHC-like radiation background*, *Nuclear Instruments and Methods in Physics Research Section A: Accelerators, Spectrometers, Detectors and Associated Equipment* **958** (2020) 162073.

[95] M. Abbrescia, A. Colaleo, G. Iaselli, F. Loddo, M. Maggi, B. Marangelli et al., *The simulation of resistive plate chambers in avalanche mode: charge spectra and efficiency*, *Nuclear Instruments and Methods in Physics Research Section A: Accelerators, Spectrometers, Detectors and Associated Equipment* **431** (1999) 413.

[96] I. Crotty, E. Cerron Zeballos, J. Lamas Valverde, D. Hatzifotiadou, M. Williams and A. Zichichi, *The wide gap resistive plate chamber*, *Nuclear Instruments and Methods in Physics Research Section A: Accelerators, Spectrometers, Detectors and Associated Equipment* **360** (1995) 512.

[97] M. Abbrescia, A. Colaleo, G. Iaselli, F. Loddo, M. Maggi, B. Marangelli et al., *New developments on front-end electronics for the CMS Resistive Plate Chambers*, *Nuclear Instruments and Methods* **456** (2000) 143.

[98] C. Binetti, R. Liuzzi, F. Loddo, B. Marangelli and A. Ranieri, *A new Front-End Board for RPC detector of CMS*, *CMS Note-1999/047* (1999) .

[99] S. Wuyckens, *Development of a compact telescope for cosmic muon flux and density measurements*, Master Thesis, Université catholique de Louvain.

[100] "renz Electronic TE0720-03-1CF." https://wiki.trenz-electronic.de/display/PD/TE0720+TRM.

[101] "Iseg DPS mini." https://iseg-hv.com/en/products/detail/DPS.

[102] "ADC AD7417." https://www.analog.com/en/products/ad7417.html.

[103] "DAC AD5593R." https://www.analog.com/en/products/ad5593r.html.

[104] "PCF8574AT I2C BUS." https://www.nxp.com/part/PCF8574AT#/.

[105] P. Demin, *Data acquisition system for the RPC detector Development documentation*, Tech. Rep. .

[106] "Hamamatsu 11411 Photo-multiplier tube." https://www.hamamatsu.com/eu/en/product/optical-sensors/pmt/pmt-module/current-output-type/H11411.html.

[107] "67WR500KLF trimmer potentiometer." https://be.farnell.com/en-BE/tt-electronics-bi-technologies/67wr500klf/trimmer-potentiometer-500kohm/dp/1782676?ost=67wr500k.

[108] "71251-040/0800 DIN female connector." https://be.farnell.com/en-BE/prehkeytec/71251-040-0800/socket-din-pcb-4pin/dp/1193183?st=71251.

[109] "QL355TP dual channel power supply." https://www.tme.eu/html/EN/multichannel-power-supplies-qlx-series/ramka_11372_EN_pelny.html.

[110] "CAEN N415A 8 Ch autowalk constant fraction discriminato." https://www.caen.it/products/n842/.

[111] "Teltronix TDS 3014 four channel digital oscilloscope." https://www.allaboutcircuits.com/test-measurement/oscilloscopes/tds3000-series-tds-3014/.

[112] R.L. William, *Techniques for Nuclear and Particle Physics Experiments*, Springer-Verlag Berlin Heidelberg GmbH, second rev ed. (1994).

[113] W. Maryniak, T. Uehara and M. Noras, *Surface Resistivity and Surface Resistance Measurements Using a Concentric Ring Probe Technique*, .

[114] "LOCTITE EDAG PM 404 EC." https://www.henkel-adhesives.com/be/en/product/industrial-inks-and-coatings/loctite_edag_pm_404ec0.html.

[115] "LTspice simulator." https://www.analog.com/en/design-center/design-tools-and-calculators/ltspice-simulator.html.

[116] "Twisted Pair Flat Cable." https://www.farnell.com/datasheets/688120.pdf.

[117] Y. Yu, Y. Wang, D. Han, X. Chen, P. Lyu, F. Wang et al., *Study of transmission-line impedance of strip lines in an MRPC detector*, *Nuclear Instruments and Methods in Physics Research Section A: Accelerators, Spectrometers, Detectors and Associated Equipment* **953** (2020) 163152.

[118] V. Ammosov, A. Ivanilov, V. Koreshev, Y. Sviridov, V. Zaets and A. Semak, *Study of cross-talks for multi-strip RPC read-out*, *Nuclear Instruments and Methods in Physics Research Section A: Accelerators, Spectrometers, Detectors and Associated Equipment* **456** (2000) 55.

[119] W. Riegler and D. Burgarth, *Signal propagation, termination, crosstalk and losses in resistive plate chambers*, *Nuclear Instruments and Methods in Physics Research Section A: Accelerators, Spectrometers, Detectors and Associated Equipment* **481** (2002) 130.

[120] "NRITSU MS2713E spectrum analyzer." https://www.anritsu.com/en-us/test-measurement/products/ms2713e.

[121] "Make more mile on VHF." https://mmmonvhf.de/bcn.php?detail=136.

[122] "TPG 110 10Mhz pulse generator."
https://www.aimtti.com/product-category/pulse-generators/aim-tgp110.

[123] "Fug 35-20000 high voltage power supply."
https://smt.at/wp-content/uploads/smt-datenblatt-fug-hce-deutsch-22-03.pdf.

[124] Gamage R.M.I.D, Basnet Samip, Cortina Gil Eduardo, Giammanco Andrea, Demin Pavel, Moussawi Marwa et al., *Portable resistive plate chambers for muography in confined environments*, *E3S Web Conf.* **357** (2022) 01001.